



A MegaCam Survey of Outer Halo Satellites. III. Photometric and Structural Parameters^{*†}

Ricardo R. Muñoz^{1,2}, Patrick Côté³, Felipe A. Santana¹, Marla Geha², Joshua D. Simon⁴, Grecco A. Oyarzún¹, Peter B. Stetson³, and S. G. Djorgovski⁵

¹ Departamento de Astronomía, Universidad de Chile, Camino del Observatorio 1515, Las Condes, Santiago, Chile; rmunoz@das.uchile.cl

² Astronomy Department, Yale University, New Haven, CT 06520, USA

³ National Research Council of Canada, Herzberg Astronomy & Astrophysics Program, 5071 W. Saanich Road, Victoria, BC, V9E 2E7, Canada

⁴ Observatories of the Carnegie Institution of Washington, 813 Santa Barbara St., Pasadena, CA 91101, USA

⁵ Astronomy Department, California Institute of Technology, Pasadena, CA 91125, USA

Received 2017 August 10; revised 2018 April 28; accepted 2018 April 30; published 2018 June 12

Abstract

We present structural parameters from a wide-field homogeneous imaging survey of Milky Way satellites carried out with the MegaCam imagers on the 3.6 m Canada–France–Hawaii Telescope and 6.5 m Magellan-Clay telescope. Our survey targets an unbiased sample of “outer halo” satellites (i.e., substructures having galactocentric distances greater than 25 kpc) and includes classical dSph galaxies, ultra-faint dwarfs, and remote globular clusters. We combine deep, panoramic *gr* imaging for 44 satellites and archival *gr* imaging for 14 additional objects (primarily obtained with the DECam instrument as part of the Dark Energy Survey) to measure photometric and structural parameters for 58 outer halo satellites. This is the largest and most uniform analysis of Milky Way satellites undertaken to date and represents roughly three-quarters (58/81 \simeq 72%) of all known outer halo satellites. We use a maximum-likelihood method to fit four density laws to each object in our survey: exponential, Plummer, King, and Sérsic models. We systematically examine the isodensity contour maps and color–magnitude diagrams for each of our program objects, present a comparison with previous results, and tabulate our best-fit photometric and structural parameters, including ellipticities, position angles, effective radii, Sérsic indices, absolute magnitudes, and surface brightness measurements. We investigate the distribution of outer halo satellites in the size–magnitude diagram and show that the current sample of outer halo substructures spans a wide range in effective radius, luminosity, and surface brightness, with little evidence for a clean separation into star cluster and galaxy populations at the faintest luminosities and surface brightnesses.

Key words: galaxies: dwarf – galaxies: photometry – galaxies: structure – globular clusters: general – Local Group – surveys

1. Introduction

The halo of the Milky Way contains substructures that hold important clues to the formation and evolution of the halo itself. Historically, these substructures (i.e., satellites) were divided into two distinct populations—i.e., globular clusters and dwarf galaxies—presumed to have fundamentally different formation channels. At the same time, history has also shown that the census of satellites at any time depends sensitively on observational selection effects, with surface brightness being a critical factor in our ability to identify and characterize halo substructures.

Over the past two decades, a number of wide-field optical surveys (having point-source detection limits that allow extremely faint surface brightness thresholds to be reached) have revolutionized our view of the halo and its embedded substructures. In addition to revealing numerous stellar streams and large-scale density fluctuations, these surveys (most notably the Sloan Digital Sky Survey (SDSS), Pan-STARRS, and the Dark Energy Survey (DES); York et al. 2000; Diehl et al. 2014; Chambers et al. 2016) have led to the discovery of

more than 50 satellites since 2000, i.e., roughly two-thirds of all outer halo substructures known at this time.

In a number of cases, the newly discovered satellites cannot easily be identified as globular clusters or dwarf galaxies, the two-category scheme historically used to classify halo substructures. In these instances, spectroscopic data are essential for measuring dynamical mass-to-light ratios and/or element abundances of individual stars. Still, it is worth bearing in mind that classifying as a star cluster or dwarf galaxy on the basis of photometric and structural parameters can itself be problematic. First, published catalogs for satellites tend to focus on either globular clusters or dwarf galaxies, rather than taking a holistic approach to halo substructures in general. Second, existing compilations often rely on shallow and heterogeneous data, some of them dating back to the 1960s (see, e.g., Djorgovski 1993; Pryor & Meylan 1993; Irwin & Hatzidimitriou 1995; Trager et al. 1995; Harris 1996; Mateo 1998; McLaughlin & van der Marel 2005; McConnachie 2012 and references therein). Finally, photometric and structural parameters are usually derived by fitting parametric models to the observed one- or two-dimensional density profiles, with different choices of the density law commonly made for globular clusters and dwarf galaxies.

Between 2009 and 2011, we carried out an extensive imaging survey that aimed to address these issues by using the 3.6 m Canada–France–Hawaii Telescope (CFHT) and the 6.5 m Magellan-Clay telescope to acquire panoramic *gr* images

^{*} Based on observations obtained at the Canada–France–Hawaii Telescope (CFHT), which is operated by the National Research Council of Canada, the Institut National des Sciences de l’Univers of the Centre National de la Recherche Scientifique of France, and the University of Hawaii.

[†] This paper includes data gathered with the 6.5 m Magellan Telescopes located at Las Campanas Observatory, Chile.

for a nearly complete sample of substructures in the outer halo of the Milky Way (i.e., at galactocentric radii of $r_{GC} = 25$ kpc or more). In this paper, we use the point-source photometric catalogs from this program to derive homogeneous photometric and structural parameters for each of our program objects.

This paper is the latest in a series that explores the properties of outer halo substructures based on these CFHT and Magellan data. Muñoz et al. (2018, hereafter Paper I) have presented an overview of the survey, including observational material, target selection, reduction procedures, and data products. In an upcoming paper, we will use the structural and photometric parameters from this paper to explore the scaling relations of outer halo satellites. Bradford et al. (2011) used imaging from this survey to carry out a dynamical analysis of the globular cluster Palomar 13, while Muñoz et al. (2012a) reported the discovery of an ultra-faint star cluster (Muñoz 1) in the direction of the Ursa Minor dwarf galaxy. Santana et al. (2013) presented a study of blue straggler stars across satellites of all types, while Carballo-Bello et al. (2015) reported the detection of possible foreground populations associated with Monoceros substructure in the direction of NGC 2419 and Kposov 2. Recently, Santana et al. (2016) used imaging for the Carina dwarf galaxy to investigate its spatially resolved star formation history, and finally, Carballo-Bello et al. (2017) studied the leading and trailing arms of the Sagittarius tidal stream around the globular cluster Whiting 1.

This paper is structured as follows. In Section 2, we briefly review our observations and sample selection. Our maximum-likelihood method for measuring structural parameters and density profiles is described in Section 3. Section 4 presents a comparison to previous results, including a case-by-case discussion of our survey targets. A discussion of our results is presented in Section 5, and we conclude in Section 6.

2. Observations and Target Selection

The scientific justification for our survey, including target selection, observing strategy, data reduction methods, and photometric calibration, is described in detail in a companion paper (Paper I). Briefly, our sample consists of 44 primary targets and 14 secondary targets located in the outer halo of the Milky Way. Here we consider the “outer halo” to begin at a galactocentric distance of $R_{GC} = 25$ kpc. Data acquisition for targets belonging to our primary sample was completed in 2010, and, after including our 14 secondary targets, the combined sample of satellites analyzed in this paper represented—at the time of writing—58 of the 81 known Galactic satellites beyond $R_{GC} = 25$ kpc (for an overall completeness level of $\approx 72\%$). Two massive satellites—the Large and Small Magellanic Clouds—were omitted from our study due to their large sizes, which render them impractical for a program of this scope. Although the same can be said of the Sagittarius dwarf spheroidal galaxy, this system lies at a galactocentric distance of 18 kpc and thus does not strictly satisfy our criterion for membership in the outer halo.

2.1. Primary Sample

Our 44 primary targets were observed in g - and r -band filters with the wide-field imagers on the CFHT and Magellan-Clay telescopes. This sample thus includes objects in both the

northern and southern hemispheres. In all, images for 30 and 14 satellites were collected using CFHT and Clay, respectively. Three satellites—the faint globular clusters Palomar 3 and NGC 7492 and the ultra-faint dwarf Segue 1—were observed with both facilities, with the intention of using them as cross-checks on our photometry and astrometry. Of the northern satellites, 22 were covered by a single pointing, as this provided full spatial coverage. The remaining eight objects were observed using either a 2×2 or 2×1 grid to ensure adequate coverage.

The MegaCam imagers are not identical instruments. The CFHT-MegaCam is a wide-field imager composed of 36 CCD chips that cover roughly 1×1 deg² on the sky (Boulade et al. 2003). The Clay-MegaCam also consists of 36 chips but covers a smaller field of 0.4×0.4 deg² (McLeod et al. 2015). In both cases, the images delivered by the observatory were pre-processed to correct for instrumental signatures across the mosaic. Image processing was then carried out using the DAOPHOT, ALLSTAR, and ALLFRAME packages (Stetson 1994), and astrometric solutions were refined using the SCAMP package.⁶ The typical 5σ point-source limits are $g_{lim} \simeq 25.6$ and $r_{lim} \simeq 25.3$ AB magnitudes, with typical seeing of $0''.7$ – $0''.9$ for CFHT and $0''.7$ – $1''.1$ for Clay.

2.2. Secondary Sample

As discussed in Paper I, data collection for our primary sample was completed in mid-2010. Since that time, an impressive number of new Galactic satellites have been discovered, most by the DES team (the DES Collaboration et al. 2015) and independently by Kposov et al. (2015a). In 2015, we therefore retrieved the publicly available DECam images for a number of these satellites and performed photometry in a manner similar to that used for our CFHT and Clay data. Photometry for a few other systems whose images were not publicly available was kindly provided by their respective discovery teams.

Table 1 lists the 44 objects belonging to our primary sample, along with their center equatorial coordinates (from this work). This table also includes estimates for their heliocentric distances, metallicities, metallicity dispersions, heliocentric systemic velocities, radial velocity dispersions, and mass-to-light ratios, when available, from the literature. At the bottom of Table 1, we present the same information for our secondary sample of 14 satellites.

2.3. Satellites Not Included in Our Survey: Tertiary Sample

The discovery of Galactic satellites has proceeded apace, and many new faint stellar systems have been reported during the past 2 yr. In all, 21 newly discovered outer halo satellites are absent from our sample defined in 2015.

1. Fourteen objects discovered in DES imaging. Kim 2 (Kim & Jerjen 2015a), Peg III (Kim et al. 2015a), Tuc II (Kposov et al. 2015a; the DES Collaboration et al. 2015), Tuc IV, Cet II, Ret III, Col I, Ind II, Gru II, Tuc V and Tuc III (Drlica-Wagner et al. 2015), DESJ0034–4902 (Luque et al. 2016), and DESJ0111–1341 and DESJ0225+0304 (Luque et al. 2017).

⁶ <http://astromatic.net/software/scamp>

Table 1
Adopted and Derived Parameters for Outer Halo Satellites

No.	Object	α_0 (J2000) (deg)	σ_α (s)	δ_0 (J2000) (deg)	σ_δ (arcsec)	R_\odot (kpc)	R_{GC} (kpc)	[Fe/H] (dex)	$\sigma_{[Fe/H]}$ (dex)	\bar{v}_r (km s $^{-1}$)	σ_{v_r} (km s $^{-1}$)	M/L_V ($M_\odot/L_{V,\odot}$)	Sources
Primary Sample													
1	Sculptor	15.0183	0.30	-33.7186	2.6	86.0	86.1	-1.68	0.46	111.4	9.20 \pm 1.40	12	1, 2
2	Whiting 1	30.7372	0.18	-3.2519	3.0	30.1	34.9	-0.70	...	-130.6	3
3	Segue 2	34.8226	0.95	+20.1624	16.5	35.0	41.2	-2.22	0.43	-40.2	<2.6	<500	4
4	Fornax	39.9583	0.26	-34.4997	3.5	147.0	149.1	-1.04	0.33	55.2	11.7 \pm 0.9	5.7	1, 2
5	AM 1	58.7608	0.14	-49.6152	1.5	123.3	124.7	-1.70	...	116.0	0.68	...	5
6	Eridanus	66.1853	0.10	-21.1876	1.5	90.1	95.4	-1.43	...	-23.6	0.9	...	5
7	Palomar 2	71.5248	0.00	+31.3817	0.0	27.2	35.5	-1.42	...	-133.0	8.39	...	5
8	Carina	100.4065	0.58	-50.9593	4.4	105.0	106.7	-1.72	0.33	222.9	6.6 \pm 1.2	34	2, 6
9	NGC 2419	114.5354	0.07	+38.8819	0.9	82.6	90.4	-2.10	0.032	-20.2	4.4 \pm 0.5	2.05	7, 8
10	Koposov 2	119.5715	0.26	+26.2574	5.5	34.7	42.3	
11	UMa II	132.8726	3.66	+63.1335	9.2	32.0	38.5	-2.18	0.66	-116.5	6.7 \pm 1.4	1910	1, 9
12	Pyxis	136.9869	0.15	-37.2266	2.1	39.4	41.5	35.9	2.5	...10	
13	Leo T	143.7292	0.52	+17.0482	5.6	417.0	422.1	-1.74	0.54	35	7.5 \pm 1.6	...	1, 9
14	Palomar 3	151.3823	0.09	+0.0718	1.4	92.5	96.0	-1.63	...	83.4	1.17	...	5
15	Segue 1	151.7504	2.84	+16.0756	27.4	23.0	28.1	-2.74	0.75	208.5	3.9 \pm 0.8	1530	11
16	Leo I	152.1146	0.12	+12.3059	1.2	254.0	256.0	-1.45	0.32	282.5	9.2 \pm 1.4	4.4	1
17	Sextans	153.2628	0.61	-1.6133	8.1	86.0	89.2	-1.94	0.47	224.3	7.9 \pm 1.3	110	1, 2
18	UMa I	158.7706	2.98	+51.9479	15.3	97.0	101.9	-2.10	0.65	-55.3	7.6 \pm 1.0	1620	1, 9
19	Willman 1	162.3436	1.04	+51.0501	4.8	38.0	43.0	-2.11	0.557	-12.3	4.3 $^{+2.3}_{-1.3}$	520	12
20	Leo II	168.3627	0.15	+22.1529	2.0	233.0	235.7	-1.63	0.40	79.1	6.6 \pm 0.7	13	1, 13
21	Palomar 4	172.3179	0.08	+28.9732	1.2	108.7	111.5	-1.41	...	74.5	1.06	...	5
22	Leo V	172.7857	1.07	+2.2194	8.6	178.0	178.8	-2.00	...	173.3	3.7 $^{+2.3}_{-1.4}$	215	14
23	Leo IV	173.2405	0.98	-0.5453	17.0	154.0	154.6	-2.45	0.65	132.3	3.3 \pm 1.7	145	1, 9
24	Koposov 1	179.8253	0.34	+12.2615	11.1	48.3	49.5	
25	ComBer	186.7454	1.02	+23.9069	12.7	44.0	45.2	-2.25	0.43	98.1	4.6 \pm 0.8	500	1, 9
26	CVn II	194.2927	0.73	+34.3226	13.3	160.0	160.7	-2.12	0.59	-128.9	4.6 \pm 1.0	230	1, 9
27	CVn I	202.0091	1.03	+33.5521	6.6	218.0	217.8	-1.91	0.44	30.9	7.6 \pm 0.4	160	1, 9
28	AM 4	209.0883	0.31	-27.1635	4.9	33.2	28.5	-1.30	0.30	...	5
29	Boötes II	209.5141	1.86	+12.8553	21.3	42.0	39.8	-2.72	0.30	-117.0	10.5 \pm 7.4	6400	15, 16
30	Boötes I	210.0200	0.83	+14.5135	15.8	66.0	63.5	-2.59	0.43	99.0	2.4 $^{+0.9}_{-0.5}$	60	17, 18
31	NGC 5694	219.9019	0.11	-26.5390	1.3	35.0	29.1	-1.98	...	-140.3	5.8 \pm 0.8	1.5	19
32	Muñoz 1	225.4490	1.00	+66.9682	9.3	45.0	47.3	-1.46	...	-137.0	0.25 \pm 0.05	...	20
33	NGC 5824	225.9943	0.00	-33.0685	0.0	32.1	25.6	-1.91	...	-27.5	11.6 \pm 0.5	...	19
34	UMi	227.2420	1.07	+67.2221	5.7	76.0	78.0	-2.13	0.34	-246.9	9.5 \pm 1.2	70	1, 21
35	Palomar 14	242.7544	0.14	+14.9584	2.2	76.5	71.3	-1.62	...	72.3	0.66	...	5
36	Hercules	247.7722	1.54	+12.7852	8.7	132.0	126.2	-2.39	0.51	45.2	3.7 \pm 0.9	140	1, 22
37	NGC 6229	251.7454	0.00	+47.5276	0.0	30.5	29.9	-1.47	...	-154.2	6.07	...	5
38	Palomar 15	254.9626	0.11	-0.5390	1.6	45.1	38.0	-2.07	...	68.9	0.79	...	5
39	Draco	260.0684	0.62	+57.9185	3.2	76.0	76.0	-1.98	0.42	-291.0	9.1 \pm 1.2	80	1, 23
40	NGC 7006	315.3721	0.00	+16.1871	0.0	41.2	38.4	-1.52	...	-384.1	4.37	...	5
41	Segue 3	320.3795	0.37	+19.1178	4.4	27.0	25.5	-1.30	...	-167	1.2 $^{+2.6}_{-1.2}$...	24
42	Pisces II	344.6345	0.61	+5.9526	5.7	182.0	181.1	-1.9	
43	Palomar 13	346.6858	0.12	+12.7712	2.5	26.0	27.1	-1.60	...	25.2	0.4 $^{+0.4}_{-0.3}$...	25
44	NGC 7492	347.1102	0.08	-15.6108	1.0	26.3	25.4	-1.78	...	-177.5	1.2 \pm 1.0	...	19
Secondary Sample													

Table 1
(Continued)

No.	Object	α_0 (J2000) (deg)	σ_α (s)	δ_0 (J2000) (deg)	σ_δ (arcsec)	R_\odot (kpc)	R_{GC} (kpc)	[Fe/H] (dex)	$\sigma_{[Fe/H]}$ (dex)	\bar{v}_r (km s ⁻¹)	σ_{v_r} (km s ⁻¹)	M/L_V ($M_\odot/L_{V,\odot}$)	Sources
1	Triangulum II	33.3252	0.97	+36.1702	19.0	30.0	36.5	-2.24	0.53	-381.7	<4.2	...	26
2	Eridanus III	35.6952	1.47	-52.2838	7.1	87.0	87.0
3	Horologium I	43.8813	1.71	-54.1160	20.2	79.0	79.3	-2.76	0.17	112.8	4.9	...	27
4	Horologium II	49.1077	14.15	-50.0486	40.4	78.0	79.1	-2.10	28
5	Reticulum II	53.9203	1.63	-54.0513	7.9	30.0	31.5	-2.46	~0.3	64.7	3.22	...	27
6	Eridanus II	56.0925	0.84	-43.5329	5.7	380.0	381.9	-2.38	0.47	75.6	6.9 ^{+1.2} _{-0.9}	...	29
7	Pictoris I	70.9490	1.92	-50.2854	8.6	114.0	115.7
8	Laevens 1	174.0668	0.28	-10.8772	2.9	145.0	144.8	-1.65	...	148.2	2.04	...	30
9	Hydra II	185.4251	0.91	-31.9860	13.7	134.0	131.1	-2.02	...	303.1	3.6	...	30
10	Kim 2	317.2020	1.21	-51.1671	38.3	100.0	94.0
11	Balbinot 1	332.6791	0.25	+14.9403	4.6	31.9	31.2	-1.58	31
	Kim 1 ^a	+332.9214	0.90	7.0271	12.9	19.8	19.2	-1.70	32
12	Grus I	344.1797	3.58	-50.1800	55.2	120.0	116.1
13	Phoenix II	354.9960	0.90	-54.4115	21.0	83.0	79.9

Note. Sources for primary sample: (1) Kirby et al. (2013b), (2) Walker et al. (2009b), (3) Carraro et al. (2007), (4) Kirby et al. 2013a; 95% confidence limit for kinematic data), (5) Webbink (1985), (6) Koch et al. (2006), (7) Willman & Strader (2012), (8) Baumgardt et al. (2009), (9) Simon & Geha (2007), (10) Palma et al. (2000), (11) Simon et al. (2011), (12) Willman et al. (2011), (13) Koch et al. (2007), (14) Walker et al. (2009a), (15) Belokurov et al. (2008), (16) Koch & Rich (2014), (17) Koposov et al. (2011), (18) Lai et al. (2011), (19) Harris (1996), (20) Muñoz et al. (2012a), (21) Wilkinson et al. (2004), (22) Adén et al. (2009), (23) Walker et al. (2007), (24) Fadely et al. (2011), (25) Bradford et al. (2011). Sources for secondary sample: (26) Kirby et al. (2017; 95% confidence limit for kinematic data), (27) Koposov et al. (2015b), (28) Kim & Jerjen (2015a), (29) Li et al. (2017), (30) Kirby et al. (2015), (31) Balbinot et al. (2013), (32) Kim & Jerjen (2015b).

^a Inner halo member.

Table 2
Satellites Not Included in This Survey: Tertiary Sample

No.	Name	α_0 (J2000) (deg)	δ_0 (J2000) (deg)	R_\odot (kpc)	R_{GC} (kpc)	M_V (mag)	r_e (pc)	ϵ	\bar{v}_r (km s ⁻¹)	Sources
Inner Halo ($R_{GC} < 25$ kpc)										
1	<i>Gaia</i> 2	28.12	+53.04	5.5	12.8	-2.0	3	$0.18^{+0.20}_{-0.12}$...	1
2	<i>Gaia</i> 1	101.47	-16.75	4.6	12.1	-5.1	9	...	57.6	1, 2
3	Draco II	238.20	+64.57	20 ± 3	22 ± 3	-2.9 ± 0.80	19^{+8}_{-6}	0.24 ± 0.25	$+347.6 \pm 1.8$	3, 4
4	Sagittarius	283.83	-30.55	26 ± 2	18 ± 2	-13.5 ± 0.3	2587 ± 219	0.64 ± 0.02	$+140.0 \pm 2.0$	5
5	Tucana III	359.15	-59.60	25 ± 2	23 ± 2	-2.4 ± 0.42	44 ± 6	...	-102.3 ± 0.4	6, 7
Outer Halo ($R_{GC} \geq 25$ kpc)										
1	Tucana IV	0.73	-60.85	48 ± 4	46 ± 4	-3.5 ± 0.28	127 ± 24	0.40 ± 0.10	...	6
2	DESJ0034-4902	8.45	-40.04	87	85	$-3.00^{+0.66}_{-0.41}$	9.88 ± 7.09	0.69 ± 0.24	...	8
3	SMC	13.19	-72.83	64 ± 4	61 ± 4	-16.8 ± 0.1	1106 ± 77	0.41 ± 0.05	$+145.6 \pm 0.6$	5
4	DESJ0111-1341	17.79	-13.68	26.5 ± 1.3	29.4 ± 1.3	$+0.3^{+0.9}_{-0.6}$	$4.55^{+1.33}_{-0.95}$	$0.27^{+0.20}_{-0.17}$...	9
5	Cetus II	19.47	-17.42	30 ± 3	32 ± 3	0.0 ± 0.68	17 ± 7	≤ 0.4	...	6
6	DESJ0225+0304	36.43	+3.07	$23.8^{+0.7}_{-0.5}$	$29.6^{+0.7}_{-0.5}$	$-1.1^{+0.5}_{-0.3}$	$18.6^{+9.2}_{-4.9}$	$0.61^{+0.14}_{-0.23}$...	9
7	Reticulum III	56.36	-60.45	92 ± 13	92 ± 13	-3.3 ± 0.29	64 ± 24	≤ 0.4	...	6
8	LMC	80.89	-69.76	51 ± 2	50 ± 2	-18.1 ± 0.1	2697 ± 115	0.15 ± 0.08	$+262.2 \pm 3.4$	5
9	Columba I	82.86	-28.03	182 ± 18	186 ± 18	-4.5 ± 0.17	103 ± 25	≤ 0.2	...	6
10	Crater II	177.31	-18.41	117 ± 2	116 ± 2	-7.8 ± 0.10	1066 ± 86	≤ 0.1	...	10
11	Virgo I	180.04	-0.68	87^{+13}_{-8}	87^{+13}_{-8}	-0.8 ± 0.9	38^{+12}_{-11}	$0.44^{+0.14}_{-0.17}$...	11
12	Sagittarius II	298.17	-22.07	67 ± 5	60 ± 5	-5.2 ± 0.40	38^{+8}_{-7}	0.23 ± 0.20	...	3
13	Indus II	309.72	-46.16	214 ± 16	208 ± 16	-4.3 ± 0.19	181 ± 67	≤ 0.4	...	6
14	Laevens 3	316.73	+14.98	67 ± 3	64 ± 3	-4.4 ± 0.30	7 ± 2	0.21 ± 0.21	-140.5 ± 2.0	3
15	Grus II	331.02	-46.44	53 ± 5	49 ± 5	-3.9 ± 0.22	93 ± 14	≤ 0.21	...	6
16	Pegasus III	336.10	+05.41	205 ± 20	203 ± 20	-4.1 ± 0.50	78^{+30}_{-24}	0.46 ± 0.23	...	12, 13
17	Aquarius II	338.48	-9.33	108 ± 3	105 ± 3	4.36 ± 0.14	159 ± 24	0.39 ± 0.09	71.1 ± 2.5	14
18	Tucana II	342.98	-58.57	57 ± 5	53 ± 5	-3.8 ± 0.10	165^{+28}_{-19}	0.39 ± 0.15	-129.1 ± 3.5	15, 16, 17
19	Tucana V	354.35	-63.27	55 ± 9	52 ± 9	-1.6 ± 0.49	17 ± 6	0.70 ± 0.15	...	6

Note. Sources for tertiary sample: (1) Koposov et al. (2017), (2) Mucciarelli et al. (2017), (3) Laevens et al. (2015a), (4) Martin et al. (2016), (5) McConnachie (2012), (6) Drlica-Wagner et al. (2015), (7) Simon et al. (2017), (8) Luque et al. (2016), (9) Luque et al. (2017), (10) Torrealba et al. (2016a), (11) Homma et al. (2016), (12) Kim et al. (2015a), (13) Kim et al. (2016), (14) Torrealba et al. (2016b), (15) Koposov et al. (2015a), (16) the DES Collaboration et al. (2015), (17) Walker et al. (2016).

2. Two objects discovered in Pan-STARRS imaging. Sgr II (Laevens et al. 2015a) and Laevens 3 (Laevens et al. 2015a).
3. Two objects discovered in VST/ATLAS imaging. Cr II (Torrealba et al. 2016a) and Aqu II (Torrealba et al. 2016b).
4. Two objects discovered in Subaru/HSC imaging. Vir I (Homma et al. 2016) and Cetus III (Homma et al. 2018).
5. Two new objects have been discovered in the constellation of Carina during the revision phase of this article: Carina II and III (Torrealba et al. 2018).

To summarize, 81 cataloged stellar systems meet our definition of outer halo members, i.e., our 58 primary and secondary targets, the two Magellanic Clouds, and the 21 recently discovered stellar systems listed above (see Table 2). Thus, the sample analyzed here represents 72% of all known outer halo satellites. If one restricts the sample to systems fainter than $M_V = -13.45$ (the absolute magnitude of the Fornax dSph galaxy, the brightest object in our sample), then the overall completeness is $58/77 \simeq 75\%$.

We note in passing that three other newly discovered satellites—Dra II (Laevens et al. 2015a) and *Gaia* 1 and 2 (Koposov et al. 2017)—are located at $R_{GCC} < 25$ kpc and so do not satisfy our criterion for membership in the outer halo.

3. Structural Parameters and Density Profiles

3.1. Two-dimensional Analysis: Parameter Estimation with a Maximum-likelihood Approach

The extreme sparseness of stellar systems at the faint end of the galaxy luminosity function (LF) challenges our ability to derive reliable photometric and structural parameters (e.g., Martin et al. 2008b; Sand et al. 2009; Muñoz et al. 2012b). Such parameters—including integrated luminosities, effective radii, and central and mean effective surface brightness, to name a few—are key ingredients in the measurement of dynamical masses and, ultimately, in using faint stellar systems in near-field cosmological studies of galaxy formation.

Martin et al. (2008b) presented a comprehensive analysis of SDSS photometric data available for the ultra-faint galaxies and derived structural parameters for them using a technique that (1) relies on all stars observed in a given field and (2) does not require binning of the photometric data. Sand et al. (2009) and Muñoz et al. (2010) showed that the structural parameters derived via this method often suffer from significant associated uncertainties—in some cases as large as 80%. This is largely a consequence of the relatively shallow depth of the SDSS, which has 5σ point-source limiting magnitudes in the g and r bands of ~ 23.3 and ~ 23.1 , respectively (York et al. 2000), although Martin et al. (2008b) only used stars with $g < 22.5$

and $r < 22$ for most objects. Indeed, Muñoz et al. (2012b) quantified the impact of stellar sample size on the measurement of structural parameters, showing that photometry significantly deeper than SDSS would typically be needed to measure parameters to a precision of $\sim 20\%$ or better.

Our survey has been specifically designed to produce improved estimates for the photometric and structural parameters of stellar systems in the outer halo. As shown in Figure 15 of Paper I, our imaging reaches typical 5σ point-source depths of $g \simeq 25.6$ and $r \simeq 25.3$, or about 2.2 mag deeper than SDSS. On average, our photometry reaches ~ 2 mag below the main-sequence turnoff (MSTO) in our program objects (with some variation between objects, depending mainly on their distance; i.e., in the case of our most distant target, Leo T, we fall ~ 2 mag short of the expected location of the MSTO). In addition, our analysis benefits from improved star–galaxy separation compared to SDSS, thanks to the superior image quality of CFHT and Clay. The median FWHMs for these two data sets are $0''.8$ and $0''.9$, respectively, which are significant improvements to what is available from SDSS ($1''.4$).

We employ the methodology described in Martin et al. (2008b) and adopted by several other authors. In essence, the technique determines six structural parameters simultaneously. These parameters are the equatorial coordinates, α_0 and δ_0 , of the center of the satellite; the radius, r_h , containing half the luminosity; the ellipticity, ϵ , of the projected two-dimensional isophotes; the position angle, θ , measured north through east, of the major axis; and the background density of stellar sources, Σ_b , not belonging to the satellite. This last parameter reflects the unavoidable presence of Galactic stars and unresolved galaxies in any field.

Muñoz et al. (2012b) showed that the reliability of the measured structural parameters depends not just on the total number of satellite stars but also on the stellar density contrast between the satellite and the background density. Thus, it is critically important to maximize the ratio Σ_0/Σ_b , where Σ_0 is the central surface density of the satellite. For each program object, we therefore select point sources having DAOPHOT morphological classification indices— χ and sharp—that are consistent with stellar detections (Stetson 1994). In our specific case, we adopt $-0.4 < \text{sharp} < +0.4$ and $\chi < 3$. Additionally, we select candidate stars only in regions of the color–magnitude diagram (CMD) that are close to the primary sequences of each satellite, i.e., the main sequence, MSTO, red giant branch (RGB), horizontal branch (HB), or red clump, when present.

As in our previous studies (Muñoz et al. 2010, 2012b), we initially fitted three density models that have been commonly used to fit the surface density or surface brightness profiles of Local Group galaxies: (1) an exponential profile, (2) a Plummer profile (Plummer 1911), and (3) a King profile (King 1962). The first two models are known to provide adequate descriptions for dwarf galaxies, while the third model, although most commonly used to fit the profiles of globular clusters, has been used successfully to fit the density profiles of dwarf galaxies as well (e.g., Irwin & Hatzidimitriou 1995). We note that, as has been argued in the past, King model parameters do not have obvious physical interpretations for dark matter–dominated systems (e.g., Koch et al. 2006; Gilmore et al. 2007).

The three profiles investigated here have the following functional forms:

$$\Sigma_{\text{exp}}(r) = \Sigma_{0,E} \exp\left(-\frac{r}{r_E}\right), \quad (1)$$

$$\Sigma_{\text{Plummer}}(r) = \Sigma_{0,P} \left(1 + \frac{r^2}{r_P^2}\right)^{-2}, \quad (2)$$

$$\Sigma_{\text{King}}(r) = \Sigma_{0,K} \left[\left(1 + \frac{r^2}{r_c^2}\right)^{-\frac{1}{2}} - \left(1 + \frac{r_t^2}{r_c^2}\right)^{-\frac{1}{2}} \right]^2. \quad (3)$$

Here r_E and r_P are the exponential and Plummer scale lengths, respectively, while r_c and r_t are the King core and tidal radii. Note that the exponential scale length is related to the half-light radius by the relation $r_h = 1.68 \times r_E$. In the case of the Plummer profile, r_P is equivalent to r_h .

We also include a fourth parameterization in our analysis. Although originally used to fit the luminosity profiles of early-type galaxies, we also fitted a Sérsic model to each of our program objects (Sérsic 1968). This model takes the form

$$\Sigma_{\text{Sérsic}}(r) = \Sigma_{0,S} \exp\left[-\left(\frac{r}{r_e}\right)^{1/n}\right], \quad (4)$$

where n is the Sérsic index, a measure of concentration. The effective radius, r_e , which contains half the total luminosity, is defined as $r_e = b_n^n \alpha$, where $b_n = 1.999n - 0.327$ (Caon et al. 1990). This parameterization is known to provide a good representation of the brightness profiles of early-type galaxies in local clusters, including low-mass dSph-like galaxies similar to those in the outer halo (see, e.g., Jerjen & Binggeli 1997; Graham & Guzmán 2003; Graham et al. 2003; Ferrarese et al. 2006; Côté et al. 2007).

The maximum-likelihood technique that we use for our analysis is predicated on the assumption that we know the shape of the satellite’s light distribution beforehand (i.e., one of the four models described above). The position of stars in our photometric catalog should then follow this distribution, which is well represented by a set of parameters p_1, p_2, \dots, p_j . Thus, we maximize a function of the form

$$L(p_1, p_2, \dots, p_j) = \prod_i l_i(p_1, p_2, \dots, p_j), \quad (5)$$

where $l_i(p_1, p_2, \dots, p_j)$ is the probability of finding the datum i given the set of parameters p_1, p_2, \dots, p_j . For example, in the case of a Plummer profile, this function takes the form

$$l_i(p_1, p_2, \dots, p_j) = S_0 \left(1 + \frac{r_i^2}{r_P^2}\right)^{-2} + \Sigma_b, \quad (6)$$

where S_0 , r_i , and r_P are expressed in terms of the structural parameters we want to determine.

In practice, to identify the best-fit parameters, we look for a global maximum $\log(L(\hat{p}_1, \hat{p}_2, \dots, \hat{p}_j))$ by searching the j -dimensional parameter space. In the case of an exponential and Plummer profile, the parameter space is six-dimensional, with free parameters α_0 , δ_0 , ϵ , θ , r_h , and Σ_b . For a King profile, the approach is slightly different. In this case, there are seven parameters to be determined because the tidal truncation introduced by this density law results in two characteristic

radii: the core radius, r_c , and tidal radius, r_t . Finding a set of parameters that maximize L has the extra complication that r_t is degenerate with Σ_b . We therefore fix the background density to the value found for the Plummer profile. The case of the Sérsic model is similar because there are again seven parameters to fit, including the background density. In this instance, the Sérsic index is degenerate with the background density, so we follow the same strategy adopted for the King profile: i.e., we fix the value of the background density to that found for the Plummer model and solve for the remaining six parameters.

We find a solution by searching the parameter space using the amoeba simplex algorithm (Press et al. 1988). This method is somewhat sensitive to the specified region of parameter space to be searched (i.e., the initial guess and allowed range for the parameters), but it runs considerably faster than an iteratively refined grid. To ensure convergence, we restarted the amoeba three times using the previously derived values. To derive uncertainties for the structural parameters, we carry out 10,000 bootstrap realizations of our data (i.e., a resampling with replacement). In most cases, the distribution of a given parameter is well described by a Gaussian distribution, except for the King tidal radius, which tends to deviate slightly from this functional form. We have therefore fitted Gaussian functions and report their mean and standard deviation as the mean and 1σ uncertainty for a given parameter.

Table 3 presents the best-fit structural parameters and their errors for the exponential and Plummer profiles. In all cases, we tabulate the position angles (θ), overall ellipticities (ϵ), and half-light radii (in both angular and physical units). In Tables 4 and 5, we list the best-fit King and Sérsic parameters.

3.2. Absolute Magnitude and Central Surface Brightness

In the past, total luminosities for resolved stellar systems have usually been estimated by adding the fluxes of individual stars down to a certain limiting magnitude and then correcting for the “missing” light contributed by stars below this threshold. Given the small number of stars in most ultra-faint dwarfs and some of the outer halo globular clusters, it has been argued (e.g., Martin et al. 2008b; Walsh et al. 2008; Sand et al. 2009; Muñoz et al. 2010, 2012b) that this methodology is prone to error due to shot noise; i.e., the inclusion or exclusion of even a single RGB star can significantly change the measured total luminosity for some systems. Therefore, an alternative method is often used to calculate the integrated luminosity or absolute magnitude in a given bandpass. In this study, we apply this alternative technique to all objects regardless of the number of stars, with the exception of the brighter classical dSphs, which can present complex star formation histories.

The method relies on the number of stars, N_* , that belong to the satellite down to the adopted magnitude threshold. The value of N_* is related to the background density Σ_b obtained from the maximum-likelihood method by

$$N_* = N_{\text{total}} - A\Sigma_b, \quad (7)$$

where N_{total} is the total number of stars (both satellite stars and background objects) used to determine the best-fit structural parameters, and A is the total area of the field.

We then assume that the satellites in our survey are well described by old, single stellar populations. This assumption is certainly reasonable for the globular clusters and appropriate for most of the dwarf galaxies as well. Indeed, the faintest

dwarfs in our sample seem to consist exclusively of old, metal-poor populations (Brown et al. 2012). This is also true of at least some of the brighter dSph systems like Draco, Ursa Minor, and Sextans (Santana et al. 2013).

We then model the respective stellar populations using theoretical LFs. In particular, we use LFs from Dotter et al. (2008a) generated for each object using the adopted metallicity and distance information and assuming a Salpeter initial mass function (Salpeter 1955). The theoretical LF then gives us the relative number of stars in different magnitude bins, from which we can derive the integrated flux down to an arbitrary threshold. Comparing this flux with what one obtains by integrating the entire LF then yields the amount of light that is contributed by stars below the adopted magnitude limit. Here N_* is used to normalize the values obtained from the theoretical LF to the values corresponding to our actual program objects.

In the case of brighter satellites, which can have more complex star formation histories (e.g., Carina, Fornax, Sculptor, and Leo I), we follow the traditional methodology. In these cases, rather than modeling the population using a theoretical LF, we sum the fluxes for all stars above the appropriate magnitude limit. Typically, this is chosen so that the completeness is higher than 90% (after removing the estimated background). We then use the theoretical LFs to correct for the missing flux below this limit.

The mean absolute magnitudes and associated uncertainties are derived using a bootstrap analysis. The procedure is as follows. We treat the theoretical LF used to calculate the luminosities as a cumulative probability function (down to our chosen magnitude threshold) for the number of stars expected as a function of magnitude. We then randomly draw a number N_* of stars from the LF and add their fluxes. We repeat this process 10,000 times and use the distribution of magnitudes to estimate 1σ errors. Table 6 records our best-fit absolute magnitudes and luminosities for all objects in the g and r bandpasses.

With structural parameters and total luminosities in hand, we can calculate μ_0 , the central surface brightness, for each object in the survey. For this calculation, we rely on the fitted Sérsic model, which, as we discuss below, provides a very good representation of the density and brightness distributions for most of our program objects, regardless of prior classification as a star cluster or dwarf galaxy. In physical units ($L_\odot \text{pc}^{-2}$), the central surface brightness is given by

$$I_0 = L/[2\pi\alpha^2 n\Gamma(2n)(1 - \epsilon)]. \quad (8)$$

From this, we can calculate the central surface brightness, in units of mag arcsec^{-2} , as

$$\mu_0 = M_\odot + 21.572 - 2.5 \log I_0. \quad (9)$$

We also report the value of μ_e , the effective surface brightness. For the Sérsic profile, this variable is related to the central surface brightness by

$$\mu_e = \mu_0 + 1.086b_n, \quad (10)$$

with the value of b_n given in Section 3.1. Our measurements for absolute magnitude, integrated luminosity, and central and effective surface brightness are given in Table 6. We quote absolute magnitudes in the g , r , and V bandpasses, while luminosities and surface brightness estimates are specified in the V bandpass. To obtain the V -band values, we used the transformation $V = g - 0.569 \times (g - r) - 0.021$ derived by

Table 3
Measured Structural Parameters: Exponential and Plummer Models

No.	Object	θ_{exp} (deg)	ϵ_{exp}	$r_{\text{h,exp}}$ (arcmin)	$r_{\text{h,exp}}$ (pc)	θ_{p} (deg)	ϵ_{p}	$r_{\text{h,p}}$ (arcmin)	$r_{\text{h,p}}$ (pc)
Primary Sample									
1	Sculptor	92 ± 1	0.36 ± 0.01	12.43 ± 0.18	311 ± 5	92 ± 1	0.33 ± 0.01	11.17 ± 0.05	280 ± 1
2	Whiting 1	53 ± 17	0.22 ± 0.08	0.70 ± 0.08	6.1 ± 0.7	48 ± 16	0.23 ± 0.07	0.64 ± 0.08	5.6 ± 0.7
3	Segue 2	166 ± 16	0.21 ± 0.07	3.64 ± 0.29	37.1 ± 2.9	164 ± 14	0.22 ± 0.07	3.76 ± 0.28	38.3 ± 2.8
4	Fornax	45 ± 1	0.28 ± 0.01	18.5 ± 0.2 ^a	791 ± 9	45 ± 1	0.29 ± 0.01	19.6 ± 0.08 ^a	838 ± 3
5	AM 1	41 ± 15	0.17 ± 0.06	0.48 ± 0.03	17.2 ± 1.1	42 ± 23	0.07 ± 0.05	0.45 ± 0.03	16.1 ± 1.1
6	Eridanus	35 ± 29	0.09 ± 0.04	0.65 ± 0.03	17.0 ± 0.8	32 ± 24	0.09 ± 0.04	0.64 ± 0.04	16.8 ± 1.0
7	Palomar 2	72 ± 13	0.06 ± 0.02	72 ± 14	0.05 ± 0.02	1.12 ± 0.08	8.9 ± 0.2
8	Carina	60 ± 1	0.37 ± 0.01	10.2 ± 0.1	311 ± 3	60 ± 1	0.36 ± 0.01	10.1 ± 0.10	308 ± 3
9	NGC 2419	103 ± 6	0.04 ± 0.01	103 ± 6	0.05 ± 0.01	0.85 ± 0.01	20.4 ± 0.2
10	Koposov 2	-36 ± 20	0.45 ± 0.15	0.42 ± 0.08	4.2 ± 0.8	-35 ± 18	0.43 ± 0.14	0.44 ± 0.07	4.4 ± 0.7
11	UMa II	-76 ± 2	0.55 ± 0.03	13.9 ± 0.4	129 ± 4	-76 ± 2	0.56 ± 0.03	13.8 ± 0.50	128 ± 5
12	Pyxis	-8 ± 28	0.04 ± 0.02	1.59 ± 0.03	18.2 ± 0.3	-12 ± 31	0.04 ± 0.01	1.62 ± 0.03	18.6 ± 0.3
13	Leo T	-104 ± 20	0.24 ± 0.09	1.27 ± 0.13	154 ± 16	-104 ± 18	0.23 ± 0.09	1.26 ± 0.13	153 ± 16
14	Palomar 3	11 ± 30	0.06 ± 0.03	0.71 ± 0.02	19.1 ± 0.5	1 ± 28	0.03 ± 0.02	0.71 ± 0.02	19.1 ± 0.5
15	Segue 1	75 ± 18	0.32 ± 0.13	3.93 ± 0.42	26.3 ± 2.8	77 ± 15	0.33 ± 0.10	3.62 ± 0.42	24.2 ± 2.8
16	Leo I	78 ± 1	0.31 ± 0.01	3.53 ± 0.03	261 ± 2	78 ± 1	0.30 ± 0.01	3.65 ± 0.03	270 ± 2
17	Sextans	57 ± 1	0.29 ± 0.01	16.9 ± 0.1	423 ± 3	57 ± 1	0.30 ± 0.01	16.5 ± 0.10	413 ± 3
18	UMa I	67 ± 2	0.59 ± 0.03	8.13 ± 0.31	229 ± 9	67 ± 2	0.59 ± 0.03	8.31 ± 0.35	234 ± 10
19	Willman 1	74 ± 4	0.47 ± 0.06	2.52 ± 0.21	27.9 ± 2.3	73 ± 4	0.47 ± 0.06	2.51 ± 0.22	27.7 ± 2.4
20	Leo II	40 ± 9	0.07 ± 0.02	2.46 ± 0.03	167 ± 2	38 ± 8	0.07 ± 0.01	2.52 ± 0.03	171 ± 2
21	Palomar 4	94 ± 31	0.02 ± 0.01	0.64 ± 0.02	20.2 ± 0.6	87 ± 25	0.03 ± 0.01	0.64 ± 0.02	20.2 ± 0.6
22	Leo V	-64 ± 33	0.45 ± 0.18	1.05 ± 0.39	54.4 ± 20.2	-71 ± 26	0.43 ± 0.22	1.00 ± 0.32	51.8 ± 16.6
23	Leo IV	-28 ± 30	0.19 ± 0.09	2.61 ± 0.32	117 ± 14	-28 ± 38	0.17 ± 0.09	2.54 ± 0.27	114 ± 12
24	Koposov 1	2 ± 19	0.54 ± 0.16	0.68 ± 0.18	9.6 ± 2.5	7 ± 21	0.45 ± 0.15	0.62 ± 0.18	8.7 ± 2.5
25	ComBer	-58 ± 4	0.37 ± 0.05	5.67 ± 0.32	72.6 ± 4.0	-57 ± 4	0.37 ± 0.05	5.64 ± 0.30	72.1 ± 3.8
26	CVn II	9 ± 13	0.41 ± 0.13	1.43 ± 0.24	66.6 ± 11.1	9 ± 15	0.40 ± 0.13	1.52 ± 0.24	70.7 ± 11.2
27	CVn I	80 ± 2	0.45 ± 0.02	7.48 ± 0.20	474 ± 13	80 ± 2	0.44 ± 0.03	7.12 ± 0.21	452 ± 13
28	AM 4	33 ± 23	0.27 ± 0.15	0.74 ± 0.18	7.1 ± 1.7	32 ± 24	0.08 ± 0.16	0.68 ± 0.15	6.6 ± 1.4
29	Boötes II	-71 ± 33	0.23 ± 0.11	3.07 ± 0.44	37.5 ± 5.4	-68 ± 27	0.25 ± 0.11	3.17 ± 0.42	38.7 ± 5.1
30	Boötes I	6 ± 3	0.26 ± 0.02	10.5 ± 0.2	202 ± 4	6 ± 3	0.30 ± 0.03	9.97 ± 0.27	191 ± 5
31	NGC 5694	65 ± 13	0.06 ± 0.02	68 ± 11	0.06 ± 0.02
32	Muñoz 1	136 ± 50	0.35 ± 0.17	0.49 ± 0.19	6.4 ± 2.5	139 ± 46	0.34 ± 0.17	0.49 ± 0.15	6.4 ± 2.0
33	NGC 5824	40 ± 6	0.04 ± 0.01	40 ± 7	0.03 ± 0.01
34	UMi	50 ± 1	0.55 ± 0.01	18.2 ± 0.1	404 ± 2	50 ± 1	0.55 ± 0.01	18.3 ± 0.11	407 ± 2
35	Palomar 14	81 ± 18	0.10 ± 0.06	1.42 ± 0.08	31.6 ± 1.8	86 ± 17	0.09 ± 0.05	1.36 ± 0.06	30.3 ± 1.3
36	Hercules	-74 ± 2	0.70 ± 0.03	5.83 ± 0.65	224 ± 25	-73 ± 2	0.69 ± 0.03	5.63 ± 0.46	216 ± 17
37	NGC 6229	-53 ± 23	0.03 ± 0.01	102 ± 76	0.03 ± 0.01	0.41 ± 0.01	3.63 ± 0.09
38	Palomar 15	93 ± 18	0.04 ± 0.02	1.45 ± 0.04	19.0 ± 0.5	91 ± 18	0.04 ± 0.02	1.49 ± 0.03	19.5 ± 0.4
39	Draco	87 ± 1	0.30 ± 0.01	9.61 ± 0.10	212 ± 2	87 ± 1	0.29 ± 0.01	9.67 ± 0.09	214 ± 2
40	NGC 7006	111 ± 6	0.06 ± 0.02	108 ± 6	0.05 ± 0.01
41	Segue 3	55 ± 29	0.25 ± 0.13	0.54 ± 0.11	4.2 ± 0.9	51 ± 38	0.23 ± 0.11	0.49 ± 0.08	3.8 ± 0.6
42	Pisces II	98 ± 13	0.39 ± 0.10	1.18 ± 0.20	62.5 ± 10.6	78 ± 20	0.34 ± 0.10	1.12 ± 0.16	59.3 ± 8.5
43	Palomar 13	6 ± 37	0.04 ± 0.04	1.26 ± 0.10	9.5 ± 0.8	11 ± 32	0.05 ± 0.05	1.14 ± 0.10	8.6 ± 0.8
44	NGC 7492	125 ± 21	0.03 ± 0.01	-51 ± 33	0.03 ± 0.02	1.28 ± 0.02	9.79 ± 0.16
Secondary Sample									
1	Triangulum II	28 ± 19	0.48 ± 0.17	2.34 ± 0.58	20.4 ± 5.1	44 ± 18	0.46 ± 0.16	1.99 ± 0.49	17.4 ± 4.3
2	Eridanus III	73 ± 28	0.57 ± 0.20	0.34 ± 0.23	8.6 ± 5.8	60 ± 28	0.58 ± 0.25	0.30 ± 0.24	7.6 ± 6.1
3	Horologium I	53 ± 27	0.32 ± 0.13	1.71 ± 0.37	39.3 ± 8.5	57 ± 25	0.27 ± 0.13	1.59 ± 0.31	36.5 ± 7.1
4	Horologium II	137 ± 12	0.71 ± 0.17	2.17 ± 0.59	49.2 ± 13.3	140 ± 12	0.72 ± 0.16	1.94 ± 0.61	44.0 ± 13.8
5	Reticulum II	69 ± 2	0.56 ± 0.03	5.41 ± 0.18	47.2 ± 1.6	70 ± 2	0.58 ± 0.02	5.52 ± 0.19	48.2 ± 1.7
6	Eridanus II	82 ± 8	0.38 ± 0.07	1.80 ± 0.16	199 ± 17	82 ± 8	0.35 ± 0.06	1.77 ± 0.17	196 ± 18.8
7	Pictoris I	69 ± 21	0.57 ± 0.19	0.89 ± 0.36	29.5 ± 11.9	72 ± 21	0.63 ± 0.21	0.88 ± 0.38	29.2 ± 12.6
8	Laevens 1	102 ± 20	0.20 ± 0.11	0.50 ± 0.06	21.1 ± 2.5	111 ± 16	0.17 ± 0.12	0.51 ± 0.16	21.5 ± 6.7
9	Hydra II	13 ± 28	0.25 ± 0.16	1.65 ± 0.39	64.3 ± 15.2	16 ± 25	0.24 ± 0.16	1.52 ± 0.28	59.2 ± 10.9
10	Kim 2	3 ± 26	0.72 ± 0.30	0.70 ± 0.46	20.4 ± 13.3	8 ± 20	0.32 ± 0.28	0.48 ± 0.41	14.0 ± 11.9
11	Balbinot 1	156 ± 13	0.33 ± 0.12	0.86 ± 0.20	8.0 ± 1.8	154 ± 10	0.37 ± 0.15	0.87 ± 0.20	8.1 ± 1.9
	Kim 1	120 ± 26	0.64 ± 0.19	0.93 ± 0.25	5.4 ± 1.4	120 ± 20	0.59 ± 0.22	1.09 ± 0.25	6.3 ± 1.4
12	Grus I	6 ± 33	0.55 ± 0.25	1.50 ± 0.68	52.4 ± 23.8	23 ± 18	0.45 ± 0.30	0.81 ± 0.66	28.3 ± 23.0
13	Phoenix II	-19 ± 15	0.62 ± 0.19	1.60 ± 0.33	38.6 ± 8.0	-20 ± 18	0.67 ± 0.22	1.49 ± 0.53	36.0 ± 12.8

Note.

^a Battaglia et al. (2006).

Table 4
Measured Structural Parameters: King Models

No.	Object	θ_k (deg)	ϵ_k	$r_{c,k}$ (arcmin)	$r_{t,k}$ (arcmin)
Primary Sample					
1	Sculptor	91 ± 1	0.37 ± 0.02	7.03 ± 0.05	74.1 ± 0.4
2	Whiting 1	46 ± 19	0.18 ± 0.07	0.20 ± 0.03	8.41 ± 1.69
3	Segue 2	167 ± 17	0.22 ± 0.07	2.93 ± 0.82	16.8 ± 3.8
4	Fornax	46 ± 1	0.28 ± 0.01	17.6 ± 0.2	69.1 ± 0.4 ^a
5	AM 1	42 ± 15	0.16 ± 0.06	0.28 ± 0.04	2.63 ± 0.36
6	Eridanus	37 ± 29	0.10 ± 0.05	0.36 ± 0.05	4.05 ± 0.65
7	Palomar 2	68 ± 21	0.04 ± 0.02	0.33 ± 0.01	8.91 ± 0.26
8	Carina	60 ± 1	0.38 ± 0.01	7.97 ± 0.16	58.4 ± 0.98
9	NGC 2419	106 ± 7	0.04 ± 0.01	0.27 ± 0.01	10.97 ± 0.07
10	Koposov 2	-36 ± 16	0.41 ± 0.15	0.23 ± 0.14	2.93 ± 1.89
11	UMa II	-77 ± 2	0.56 ± 0.03	11.7 ± 1.2	59.8 ± 3.1
12	Pyxis	-11 ± 21	0.04 ± 0.02	1.10 ± 0.06	8.17 ± 0.49
13	Leo T	-110 ± 14	0.24 ± 0.10	0.86 ± 0.57	6.25 ± 1.10
14	Palomar 3	7 ± 21	0.05 ± 0.02	0.54 ± 0.03	3.38 ± 0.16
15	Segue 1	74 ± 16	0.34 ± 0.10	3.24 ± 1.56	16.4 ± 2.6
16	Leo I	78 ± 1	0.31 ± 0.01	3.60 ± 0.10	13.5 ± 0.3
17	Sextans	58 ± 1	0.30 ± 0.01	20.1 ± 0.5	60.5 ± 0.6
18	UMa I	67 ± 3	0.57 ± 0.03	13.3 ± 2.9	24.0 ± 1.9
19	Willman 1	74 ± 4	0.47 ± 0.06	1.29 ± 0.26	16.5 ± 3.5
20	Leo II	43 ± 8	0.07 ± 0.02	2.25 ± 0.10	9.82 ± 0.41
21	Palomar 4	84 ± 43	0.03 ± 0.01	0.38 ± 0.03	3.61 ± 0.36
22	Leo V	-66 ± 21	0.46 ± 0.21	0.44 ± 0.19	9.27 ± 5.85
23	Leo IV	-30 ± 26	0.20 ± 0.09	2.14 ± 0.82	11.9 ± 3.1
24	Koposov 1	7 ± 13	0.46 ± 0.19	0.29 ± 0.12	4.3 ± 2.1
25	ComBer	-58 ± 4	0.38 ± 0.05	4.25 ± 0.73	26.1 ± 3.9
26	CVn II	10 ± 19	0.38 ± 0.15	0.89 ± 0.65	5.37 ± 4.00
27	CVn I	80 ± 2	0.47 ± 0.02	6.70 ± 0.50	30.9 ± 1.0
28	AM 4	34 ± 10	0.30 ± 0.14	0.36 ± 0.11	5.99 ± 1.85
29	Boötes II	-73 ± 30	0.25 ± 0.12	2.50 ± 1.47	12.9 ± 8.1
30	Boötes I	6 ± 3	0.26 ± 0.02	11.9 ± 1.0	37.5 ± 0.9
31	NGC 5694	66 ± 10	0.06 ± 0.02	0.05 ± 0.01	8.64 ± 0.11
32	Muñoz 1	148 ± 39	0.34 ± 0.17	0.24 ± 0.23	4.43 ± 1.93
33	NGC 5824	45 ± 1	0.04 ± 0.01	0.05 ± 0.01	13.21 ± 0.21
34	UMi	50 ± 1	0.55 ± 0.01	13.53 ± 0.3	77.3 ± 0.7
35	Palomar 14	89 ± 15	0.09 ± 0.05	0.64 ± 0.04	11.0 ± 0.8
36	Hercules	-73 ± 2	0.69 ± 0.03	3.29 ± 0.54	39.9 ± 4.7
37	NGC 6229	-42 ± 20	0.04 ± 0.01	0.09 ± 0.01	5.25 ± 0.06
38	Palomar 15	93 ± 23	0.04 ± 0.02	0.91 ± 0.06	7.92 ± 0.76
39	Draco	87 ± 1	0.30 ± 0.01	6.62 ± 0.15	48.1 ± 1.3
40	NGC 7006	110 ± 6	0.07 ± 0.02	0.12 ± 0.01	6.35 ± 0.03
41	Segue 3	59 ± 16	0.21 ± 0.13	0.27 ± 0.12	3.46 ± 0.86
42	Pisces II	99 ± 11	0.37 ± 0.10	0.72 ± 0.58	7.65 ± 2.69
43	Palomar 13	5 ± 32	0.04 ± 0.04	0.31 ± 0.05	15.9 ± 1.5
44	NGC 7492	62 ± 49	0.03 ± 0.02	0.89 ± 0.02	6.36 ± 0.07
Secondary Sample					
1	Laevens 2	36 ± 16	0.41 ± 0.16	1.39 ± 0.60	12.9 ± 3.81
2	Eridanus III	80 ± 19	0.63 ± 0.24	0.32 ± 0.21	1.45 ± 1.0
3	Horologium I	29 ± 27	0.28 ± 0.16	1.33 ± 1.13	6.61 ± 3.32
4	Horologium II	135 ± 10	0.70 ± 0.10	1.67 ± 1.23	8.07 ± 2.76
5	Reticulum II	69 ± 2	0.56 ± 0.03	6.35 ± 0.75	19.2 ± 0.9
6	Eridanus II	82 ± 6	0.37 ± 0.07	1.84 ± 0.9	6.72 ± 1.14
7	Pictoris I	72 ± 14	0.58 ± 0.20	0.64 ± 0.44	5.55 ± 2.22
9	Laevens 1	111 ± 15	0.14 ± 0.10	0.45 ± 0.14	2.01 ± 0.65
9	Hydra II	14 ± 20	0.23 ± 0.13	1.23 ± 0.57	8.22 ± 2.21
10	Indus I
11	Balbinot 1	154 ± 7	0.32 ± 0.13	0.38 ± 0.13	6.02 ± 1.00
	Kim 1	119 ± 11	0.60 ± 0.19	1.15 ± 0.25	3.07 ± 0.93
12	Grus I	9 ± 16	0.57 ± 0.23	1.26 ± 0.47	5.43 ± 3.73
13	Phoenix II	-19 ± 11	0.76 ± 0.14	0.91 ± 0.72	8.14 ± 4.46

Note.

^a Battaglia et al. (2006).

Table 5
Measured Structural Parameters: Sérsic Models

No.	Object	θ_s (deg)	ϵ_s	n_s	$r_{e,s}$ (arcmin)	$r_{e,s}$ (pc)
Primary Sample						
1	Sculptor	94 ± 1	0.37 ± 0.01	1.16 ± 0.01	12.33 ± 0.05	308 ± 1
2	Whiting 1	55 ± 13	0.24 ± 0.05	2.19 ± 0.26	0.73 ± 0.07	6.39 ± 0.61
3	Segue 2	166 ± 15	0.21 ± 0.07	0.82 ± 0.16	3.64 ± 0.29	37.1 ± 2.9
4	Fornax	46 ± 1	0.28 ± 0.01	0.71 ± 0.01	18.4 ± 0.2	787 ± 9
5	AM 1	43 ± 12	0.16 ± 0.06	1.08 ± 0.13	0.46 ± 0.03	16.5 ± 1.1
6	Eridanus	35 ± 25	0.09 ± 0.04	1.18 ± 0.14	0.64 ± 0.04	16.8 ± 1.1
7	Palomar 2	71 ± 12	0.05 ± 0.02	1.69 ± 0.04	0.99 ± 0.02	7.83 ± 0.16
8	Carina	60 ± 1	0.37 ± 0.01	0.94 ± 0.01	11.43 ± 0.12	349 ± 4
9	NGC 2419	104 ± 5	0.05 ± 0.01	1.71 ± 0.02	1.07 ± 0.01	25.7 ± 0.2
10	Koposov 2	-36 ± 25	0.48 ± 0.12	1.35 ± 0.70	0.43 ± 0.09	4.34 ± 0.91
11	UMa II	-77 ± 2	0.56 ± 0.03	0.89 ± 0.10	13.95 ± 0.46	130 ± 4
12	Pyxis	-10 ± 14	0.04 ± 0.02	0.99 ± 0.05	1.62 ± 0.04	18.6 ± 0.5
13	Leo T	-107 ± 16	0.23 ± 0.09	1.03 ± 0.26	1.25 ± 0.14	152 ± 17
14	Palomar 3	23 ± 16	0.07 ± 0.03	0.87 ± 0.05	0.72 ± 0.02	19.4 ± 0.5
15	Segue 1	75 ± 16	0.34 ± 0.11	0.85 ± 0.28	3.95 ± 0.48	26.4 ± 3.2
16	Leo I	78 ± 1	0.30 ± 0.01	0.77 ± 0.02	3.30 ± 0.03	244 ± 2
17	Sextans	58 ± 1	0.30 ± 0.01	0.60 ± 0.01	17.67 ± 0.17	442 ± 4
18	UMa I	67 ± 2	0.57 ± 0.03	0.47 ± 0.08	8.34 ± 0.34	235 ± 10
19	Willman 1	74 ± 4	0.47 ± 0.06	1.34 ± 0.20	2.53 ± 0.22	28.0 ± 2.4
20	Leo II	43 ± 8	0.07 ± 0.02	0.71 ± 0.02	2.48 ± 0.03	168 ± 2
21	Palomar 4	80 ± 15	0.03 ± 0.02	1.12 ± 0.08	0.64 ± 0.02	20.2 ± 0.6
22	Leo V	-65 ± 21	0.35 ± 0.07	1.70 ± 0.36	1.00 ± 0.22	51.8 ± 11.4
23	Leo IV	-29 ± 27	0.19 ± 0.09	0.86 ± 0.26	2.61 ± 0.31	117 ± 14
24	Koposov 1	1 ± 17	0.55 ± 0.15	1.27 ± 0.56	0.72 ± 0.18	10.1 ± 2.5
25	ComBer	-58 ± 4	0.37 ± 0.05	0.93 ± 0.12	5.63 ± 0.30	72.1 ± 3.8
26	CVn II	10 ± 11	0.46 ± 0.11	0.59 ± 0.49	1.51 ± 0.23	70.3 ± 10.7
27	CVn I	80 ± 2	0.46 ± 0.02	0.78 ± 0.04	7.67 ± 0.23	486 ± 14
28	AM 4	34 ± 15	0.29 ± 0.14	1.44 ± 0.33	0.76 ± 0.14	7.34 ± 1.35
29	Boötes II	-70 ± 27	0.24 ± 0.12	0.71 ± 0.43	3.05 ± 0.45	37.3 ± 5.5
30	Boötes I	7 ± 3	0.25 ± 0.02	0.64 ± 0.03	11.26 ± 0.27	216 ± 5
31	NGC 5694	67 ± 9	0.06 ± 0.02	3.20 ± 0.08	0.42 ± 0.01	4.28 ± 0.10
32	Muñoz 1	188 ± 15	0.50 ± 0.05	1.89 ± 0.31	1.70 ± 0.32	22.2 ± 4.2
33	NGC 5824	47 ± 4	0.04 ± 0.01	3.82 ± 0.05	0.53 ± 0.01	4.95 ± 0.09
34	UMi	50 ± 1	0.55 ± 0.01	0.82 ± 0.01	17.32 ± 0.11	383 ± 2
35	Palomar 14	90 ± 10	0.11 ± 0.04	1.49 ± 0.08	1.44 ± 0.06	32.0 ± 1.3
36	Hercules	-73 ± 2	0.69 ± 0.04	1.19 ± 0.17	5.99 ± 0.58	230 ± 22
37	NGC 6229	-23 ± 12	0.02 ± 0.01	2.62 ± 0.08	0.36 ± 0.01	3.19 ± 0.09
38	Palomar 15	93 ± 11	0.05 ± 0.02	1.04 ± 0.06	1.45 ± 0.03	19.0 ± 0.4
39	Draco	87 ± 1	0.30 ± 0.01	0.96 ± 0.02	9.93 ± 0.09	219 ± 2
40	NGC 7006	110 ± 5	0.07 ± 0.01	2.55 ± 0.07	0.51 ± 0.01	6.11 ± 0.12
41	Segue 3	65 ± 26	0.22 ± 0.09	1.30 ± 0.30	0.52 ± 0.09	4.08 ± 0.71
42	Pisces II	99 ± 13	0.40 ± 0.10	1.12 ± 0.34	1.22 ± 0.20	64.6 ± 10.6
43	Palomar 13	3 ± 19	0.10 ± 0.06	2.22 ± 0.19	1.26 ± 0.09	9.53 ± 0.68
44	NGC 7492	-5 ± 18	0.02 ± 0.02	1.00 ± 0.02	1.25 ± 0.01	9.56 ± 0.01
Secondary Sample						
1	Laevens 2	36 ± 16	0.39 ± 0.11	1.45 ± 0.45	2.00 ± 0.40	17.4 ± 3.5
2	Eridanus III	62 ± 11	0.32 ± 0.13	1.64 ± 0.27	0.29 ± 0.23	7.34 ± 5.82
3	Horologium I	50 ± 26	0.31 ± 0.16	0.98 ± 0.47	1.54 ± 0.34	35.4 ± 7.8
4	Horologium II	130 ± 16	0.86 ± 0.19	1.09 ± 0.37	2.83 ± 1.31	64.2 ± 29.7
5	Reticulum II	69 ± 2	0.56 ± 0.03	0.60 ± 0.05	5.59 ± 0.21	48.8 ± 1.8
6	Eridanus II	82 ± 7	0.37 ± 0.06	0.77 ± 0.19	1.81 ± 0.17	200 ± 19
7	Pictoris I	72 ± 10	0.24 ± 0.19	1.51 ± 0.31	0.66 ± 0.32	21.9 ± 10.6
8	Laevens 1	109 ± 25	0.11 ± 0.10	0.77 ± 0.36	0.49 ± 0.07	20.7 ± 2.9
9	Hydra II	29 ± 25	0.17 ± 0.13	1.20 ± 0.46	1.50 ± 0.32	58.5 ± 12.5
10	Indus I	5 ± 20	0.72 ± 0.29	1.22 ± 0.44	0.87 ± 0.45	25.3 ± 13.0
11	Balbinot 1	157 ± 10	0.35 ± 0.10	1.48 ± 0.23	0.84 ± 0.11	7.79 ± 1.02
	Kim 1	127 ± 24	0.67 ± 0.22	1.24 ± 0.55	0.93 ± 0.22	5.36 ± 1.27
12	Grus I	11 ± 32	0.54 ± 0.26	1.33 ± 0.31	2.08 ± 0.87	72.6 ± 30.4
13	Phoenix II	-19 ± 14	0.61 ± 0.15	1.14 ± 0.27	1.61 ± 0.27	38.9 ± 6.5

Table 6
Derived Parameters: Magnitude, Luminosity, and Surface Brightness Measurements

No.	Object	M_g (mag)	M_r (mag)	M_V (mag)	$\log L_V/L_{V,\odot}$	$\mu_{V,0}$ (mag arcsec $^{-2}$)	$\mu_{V,e}$ (mag arcsec $^{-2}$)
Primary Sample							
1	Sculptor	-10.57 ± 0.10	-10.98 ± 0.10	-10.82 ± 0.14	6.262 ± 0.056	23.29 ± 0.15	25.46 ± 0.15
2	Whiting 1	-2.26 ± 0.23	-2.73 ± 0.38	-2.55 ± 0.44	2.951 ± 0.176	$21.43^{+0.64}_{-0.66}$	25.83 ± 0.65
3	Segue 2	-1.52 ± 0.41	-2.08 ± 0.78	-1.86 ± 0.88	2.676 ± 0.352	28.48 ± 1.06	29.91 ± 1.06
4	Fornax	-13.22 ± 0.10	-13.61 ± 0.10	-13.46 ± 0.14	7.317 ± 0.056	23.59 ± 0.16	24.77 ± 0.16
5	AM 1	-4.65 ± 0.16	-5.28 ± 0.20	-5.03 ± 0.26	3.944 ± 0.104	$23.18^{+0.40}_{-0.41}$	$25.17^{+0.40}_{-0.38}$
6	Eridanus	-4.59 ± 0.16	-5.15 ± 0.21	-4.93 ± 0.26	3.904 ± 0.104	23.23 ± 0.40	25.44 ± 0.40
7	Palomar 2	-8.76 ± 0.05	-9.26 ± 0.05	-9.07 ± 0.07	5.558 ± 0.028	16.55 ± 0.11	19.87 ± 0.11
8	Carina	-9.10 ± 0.04	-9.65 ± 0.03	-9.43 ± 0.05	5.706 ± 0.020	25.35 ± 0.07	27.02 ± 0.07
9	NGC 2419	-9.16 ± 0.02	-9.45 ± 0.02	-9.35 ± 0.03	5.670 ± 0.012	18.82 ± 0.05	22.17 ± 0.05
10	Koposov 2	-0.59 ± 0.52	-1.14 ± 0.62	-0.92 ± 0.81	2.302 ± 0.324	$23.39^{+1.32}_{-1.22}$	$25.96^{+1.32}_{-1.22}$
11	UMa II	-3.86 ± 0.16	-4.50 ± 0.20	-4.25 ± 0.26	3.630 ± 0.104	28.07 ± 0.33	29.64 ± 0.33
12	Pyxis	-5.43 ± 0.13	-5.88 ± 0.14	-5.71 ± 0.19	4.215 ± 0.076	23.06 ± 0.24	24.86 ± 0.24
13	Leo T	-7.40 ± 0.10	-7.72 ± 0.10	-7.60 ± 0.14	4.973 ± 0.056	$25.42^{+0.40}_{-0.37}$	$27.30^{+0.40}_{-0.37}$
14	Palomar 3	-5.08 ± 0.13	-5.76 ± 0.17	-5.49 ± 0.21	4.127 ± 0.084	23.54 ± 0.27	25.07 ± 0.27
15	Segue 1	-1.08 ± 0.46	-1.43 ± 0.57	-1.30 ± 0.73	2.452 ± 0.292	$28.56^{+1.01}_{-0.98}$	$29.55^{+1.01}_{-0.98}$
16	Leo I	-11.43 ± 0.20	-12.00 ± 0.20	-11.78 ± 0.28	6.642 ± 0.112	22.61 ± 0.30	23.92 ± 0.30
17	Sextans	-8.36 ± 0.04	-8.95 ± 0.04	-8.72 ± 0.06	5.419 ± 0.024	27.22 ± 0.08	28.17 ± 0.08
18	UMa I	-4.51 ± 0.16	-5.55 ± 0.35	-5.12 ± 0.38	3.981 ± 0.152	29.11 ± 0.47	29.77 ± 0.47
19	Willman 1	-2.20 ± 0.37	-2.74 ± 0.64	-2.53 ± 0.74	2.943 ± 0.296	25.87 ± 0.94	28.42 ± 0.92
20	Leo II	-9.32 ± 0.02	-10.02 ± 0.03	-9.74 ± 0.04	5.828 ± 0.016	24.24 ± 0.07	25.42 ± 0.07
21	Palomar 4	-5.58 ± 0.10	-6.31 ± 0.12	-6.02 ± 0.16	4.339 ± 0.064	22.73 ± 0.23	24.80 ± 0.23
22	Leo V	-4.06 ± 0.22	-4.62 ± 0.28	-4.40 ± 0.36	3.692 ± 0.144	$24.89^{+0.90}_{-0.79}$	$28.23^{+0.90}_{-0.79}$
23	Leo IV	-4.70 ± 0.16	-5.18 ± 0.21	-4.99 ± 0.26	3.930 ± 0.104	$27.80^{+0.53}_{-0.50}$	$29.31^{+0.53}_{-0.50}$
24	Koposov 1	-0.78 ± 0.42	-1.20 ± 0.55	-1.04 ± 0.69	2.348 ± 0.276	$25.10^{+1.31}_{-1.17}$	$27.50^{+1.31}_{-1.17}$
25	ComBer	-4.03 ± 0.16	-4.60 ± 0.19	-4.38 ± 0.25	3.682 ± 0.100	26.98 ± 0.37	28.65 ± 0.37
26	CVn II	-4.80 ± 0.25	-5.42 ± 0.20	-5.17 ± 0.32	4.002 ± 0.128	$26.50^{+0.68}_{-0.63}$	$27.43^{+0.68}_{-0.63}$
27	CVn I	-8.43 ± 0.05	-9.04 ± 0.04	-8.80 ± 0.06	5.451 ± 0.024	26.78 ± 0.13	28.12 ± 0.14
28	AM 4	-0.67 ± 0.51	-1.04 ± 0.63	-0.90 ± 0.81	2.293 ± 0.324	$24.72^{+1.25}_{-1.18}$	$27.50^{+1.25}_{-1.18}$
29	Boötes II	-2.55 ± 0.31	-3.19 ± 0.67	-2.94 ± 0.74	3.106 ± 0.296	$27.55^{+1.09}_{-1.04}$	$28.74^{+1.09}_{-1.04}$
30	Boötes I	-5.71 ± 0.11	-6.21 ± 0.23	-6.02 ± 0.25	4.338 ± 0.100	28.38 ± 0.30	29.42 ± 0.30
31	NGC 5694	-7.61 ± 0.07	-8.15 ± 0.06	-7.94 ± 0.09	5.107 ± 0.036	13.41 ± 0.14	20.00 ± 0.14
32	Muñoz 1	-0.20 ± 0.62	-0.67 ± 0.74	-0.49 ± 0.97	2.127 ± 0.388	$26.32^{+1.42}_{-1.34}$	$30.07^{+1.42}_{-1.34}$
33	NGC 5824	-9.07 ± 0.03	-9.42 ± 0.03	-9.29 ± 0.04	5.648 ± 0.016	11.14 ± 0.08	19.08 ± 0.08
34	UMi	-8.70 ± 0.03	-9.25 ± 0.04	-9.03 ± 0.05	5.546 ± 0.020	25.77 ± 0.08	27.19 ± 0.06
35	Palomar 14	-4.95 ± 0.16	-5.71 ± 0.18	-5.40 ± 0.24	4.093 ± 0.096	23.58 ± 0.33	26.46 ± 0.33
36	Hercules	-5.46 ± 0.11	-6.08 ± 0.13	-5.83 ± 0.17	4.266 ± 0.068	26.82 ± 0.39	29.05 ± 0.38
37	NGC 6229	-7.74 ± 0.11	-8.24 ± 0.12	-8.05 ± 0.16	5.150 ± 0.064	13.86 ± 0.22	19.19 ± 0.22
38	Palomar 15	-5.24 ± 0.13	-5.95 ± 0.14	-5.66 ± 0.19	4.198 ± 0.076	23.06 ± 0.23	24.96 ± 0.23
39	Draco	-8.35 ± 0.03	-8.95 ± 0.04	-8.71 ± 0.05	5.417 ± 0.020	25.12 ± 0.07	26.85 ± 0.07
40	NGC 7006	-7.10 ± 0.06	-7.63 ± 0.06	-7.42 ± 0.08	4.901 ± 0.032	15.98 ± 0.12	21.16 ± 0.12
41	Segue 3	-0.74 ± 0.37	-0.93 ± 0.56	-0.87 ± 0.67	2.280 ± 0.268	$23.84^{+1.09}_{-1.02}$	$26.31^{+1.09}_{-1.02}$
42	Pisces II	-3.87 ± 0.24	-4.45 ± 0.30	-4.22 ± 0.38	3.620 ± 0.152	$26.52^{+0.77}_{-0.71}$	$28.60^{+0.77}_{-0.71}$
43	Palomar 13	-2.49 ± 0.29	-3.06 ± 0.47	-2.84 ± 0.55	3.066 ± 0.220	22.14 ± 0.70	26.60 ± 0.70
44	NGC 7492	-5.75 ± 0.03	-6.34 ± 0.03	-6.11 ± 0.04	4.375 ± 0.016	21.22 ± 0.06	23.04 ± 0.06
Secondary Sample							
1	Laevens 2	-1.46 ± 0.42	-1.67 ± 0.63	-1.60 ± 0.76	2.572 ± 0.304	$25.72^{+1.24}_{-1.16}$	$28.52^{+1.24}_{-1.16}$
2	Eridanus III	-2.01 ± 0.60	-2.61 ± 0.61	-2.37 ± 0.86	2.881 ± 0.344	$22.84^{+4.28}_{-2.13}$	$26.04^{+4.28}_{-2.12}$
3	Horologium I	-3.31 ± 0.37	-3.69 ± 0.42	-3.55 ± 0.56	3.351 ± 0.224	$26.28^{+1.10}_{-0.99}$	$28.05^{+1.10}_{-0.99}$
4	Horologium II	-1.28 ± 0.69	-1.73 ± 0.75	-1.56 ± 1.02	2.555 ± 0.408	$27.64^{+2.37}_{-1.85}$	$29.65^{+2.37}_{-1.85}$
5	Reticulum II	-3.65 ± 0.24	-4.01 ± 0.29	-3.88 ± 0.38	3.482 ± 0.152	26.77 ± 0.46	27.72 ± 0.46
6	Eridanus II	-6.89 ± 0.06	-7.41 ± 0.07	-7.21 ± 0.09	4.815 ± 0.036	26.63 ± 0.30	27.95 ± 0.30
7	Pictoris I	-3.16 ± 0.41	-3.63 ± 0.44	-3.45 ± 0.60	3.311 ± 0.240	$24.50^{+2.04}_{-1.46}$	$27.42^{+2.04}_{-1.46}$
8	Laevens 1	-4.62 ± 0.22	-4.90 ± 0.25	-4.80 ± 0.33	3.852 ± 0.132	$24.48^{+0.66}_{-0.62}$	$25.80^{+0.66}_{-0.62}$
9	Hydra II	-4.32 ± 0.25	-4.77 ± 0.27	-4.60 ± 0.37	3.771 ± 0.148	$26.14^{+0.89}_{-0.79}$	$28.39^{+0.89}_{-0.79}$
10	Indus I	-3.01 ± 0.43	-3.52 ± 0.45	-3.32 ± 0.62	3.260 ± 0.248	$24.38^{+2.20}_{-1.53}$	$26.67^{+2.20}_{-1.53}$
11	Balbinot 1	-0.94 ± 0.60	-1.40 ± 0.66	-1.22 ± 0.89	2.421 ± 0.356	$24.36^{+1.19}_{-1.16}$	$27.22^{+1.19}_{-1.16}$
	Kim 1	$+0.98 \pm 0.71$	$+0.58 \pm 0.78$	$+0.73 \pm 1.05$	1.639 ± 0.420	$25.21^{+1.64}_{-1.51}$	$27.54^{+1.64}_{-1.51}$
12	Grus I	-3.27 ± 0.39	-3.59 ± 0.44	-3.47 ± 0.59	3.321 ± 0.236	$26.86^{+1.77}_{-1.35}$	$29.39^{+1.77}_{-1.35}$
13	Phoenix II	-3.09 ± 0.42	-3.42 ± 0.47	-3.30 ± 0.63	3.252 ± 0.252	$25.85^{+1.03}_{-0.97}$	$27.96^{+1.03}_{-0.97}$

Jordi et al. (2006), which is generally useful for metal-poor Population II stars.

3.3. One-dimensional Analysis: High Surface Brightness Objects

The maximum-likelihood procedure described above will yield reliable results as long as the stellar completeness function remains roughly constant across the field. While this is true for most objects in our sample, it is not the case for Palomar 2, NGC 2419, NGC 5694, NGC 5824, NGC 6229, NGC 7006, and, to a lesser extent, NGC 7492. These stellar systems—all relatively bright globular clusters—have central V -band surface brightnesses in the range 11.15–18.33 mag arcsec⁻² (with $\mu_{V,0} \simeq 21$ mag arcsec⁻² for NGC 7492) and are therefore limited by crowding.

For these seven objects, we must resort to a more standard approach for measuring photometric and structural parameters. In the inner regions of each cluster, where crowding reduces completeness in the star counts, we performed surface photometry in the manner described by Fischer et al. (1992). The central CCD images were divided into concentric annuli positioned on the centroid of the star-count distribution. The annuli were then divided into eight azimuthal sections, and the median pixel value for these sectors was adopted as the surface brightness for the annulus at the area-weighted radius. The standard error in the median of the eight sectors was adopted as the uncertainty in the surface brightness at that radius. In the outer regions of the cluster, we used star counts to derive surface density profiles (with assumed Poisson errors) that were then matched via least-squares to the surface photometry profiles at intermediate radii.

The resulting composite surface brightness profiles were then fitted with exponential, Plummer, King, and Sérsic surface brightness profiles using Levenberg–Marquardt minimization to determine the best-fit parameters and their errors. The derived parameters are recorded in Tables 3–5, and the composite brightness profile for one representative cluster in this class, NGC 2419, is shown in Figure 1 along with the various best-fit models.

The results for NGC 2419 are typical for this sample of high surface brightness objects. As expected, the King (1962) model is found to provide an excellent representation of the surface brightness profiles for these bright globular clusters. Though less widely appreciated, the Sérsic model is also able to provide reasonable fits to these cluster brightness profiles, although we show two Sérsic models in Figure 1—one that best fits the full profile and one that excludes the central few arcseconds (see also Baumgardt et al. 2009). At the same time, an exponential profile provides a poor parameterization for these seven systems (even over a restricted radial range), and we omit the best-fit parameters for this model from Table 3. This is largely the case for the Plummer model as well. However, for this model, we find marginally acceptable fits for Palomar 2, NGC 2419, NGC 6229, and NGC 7492 and thus record the best-fit Plummer parameters in Table 3. No acceptable Plummer model fit could be found for NGC 5694, NGC 5824, or NGC 7006.

4. Results

4.1. Critical Evaluation of Density Models

It is natural to ask which family of models fitted in this paper is best able to match the surface brightness and surface density distributions of our program objects. As discussed in

Section 3.1, the choice of parameterization for different types of halo substructure has often been a matter of historical precedent, with King models being the standard choice for globular clusters and exponential or Plummer models widely used for Local Group dwarf galaxies (of both classical and ultra-faint varieties). Meanwhile, outside of the Milky Way and M31 systems, Sérsic models are usually the parameterization of choice for the surface brightness profiles of early-type galaxies, including both high-mass (giants) and low-mass (dE-type) systems (see, e.g., Jerjen & Binggeli 1997; Graham & Guzmán 2003; Graham et al. 2003; Ferrarese et al. 2006; Côté et al. 2007).

As described in Section 4.3, we can use the structural parameters derived using our maximum-likelihood method to generate a one-dimensional surface density profile for each of our program objects. In Figure 2, we show surface density profiles computed in this way for six representative objects from our survey. In order of decreasing luminosity, these are Fornax, Carina, Leo T, Hercules, Palomar 3, and Pisces II. These six satellites span a factor of nearly 5000 in luminosity and include three classical dwarf galaxies, two ultra-faint dwarf galaxies, and one low-mass globular cluster. Note that this sample excludes the high surface brightness globular clusters that, as discussed in Section 3.3, are well fitted by King or Sérsic models (but not exponential or Plummer models).

In each panel of Figure 2, we show four different models (i.e., Sérsic, King, Plummer, and exponential) having best-fit parameters derived from our two-dimensional analysis. For each of the satellites fitted with this maximum-likelihood technique, we have computed χ^2 values for these four models using the observed density profiles and fitted models. We find median χ^2 values of 0.33 (Sérsic), 0.44 (King), 0.49 (Plummer), and 0.50 (exponential). Thus, the slightly preferred parameterization for these systems is the Sérsic model, consistent with our findings for the high-luminosity globular clusters examined in Section 3.3.

This finding should perhaps not come as a surprise, for two reasons. First, unlike the Plummer or exponential laws, which have two free parameters, the Sérsic model has three: a scale density or surface brightness, a scale radius, and a concentration parameter that serves to change the shape, or curvature, of the profile. As a result, this model has greater flexibility in reproducing the observed density profiles of satellites, from classical dSphs to ultra-faint systems and globular clusters. Although the King model has three free parameters as well, including a concentration index that governs the global shape of the profile, it features (by definition) a tidal truncation that limits its ability to fit the extended profiles exhibited by some of the satellites. In addition, it is now recognized that Sérsic models are also flexible enough to accurately match to the surface brightness profiles of early-type galaxies spanning a wide range in luminosity—from brightest cluster galaxies down to the level of dwarf galaxies with luminosities comparable to the brightest systems in our sample, like Fornax, Leo I, or Sculptor (see, e.g., Ferrarese et al. 2016).

For the remainder of this paper, we therefore adopt the Sérsic parameters as the default parameters for our program objects, though structural parameters are also provided for exponential, Plummer, and King fits so that the reader is free to choose from these four options. In practice, the precise choice of model has no impact on our conclusions for the satellite population as a whole or for individual systems. For instance, Figure 3 shows a

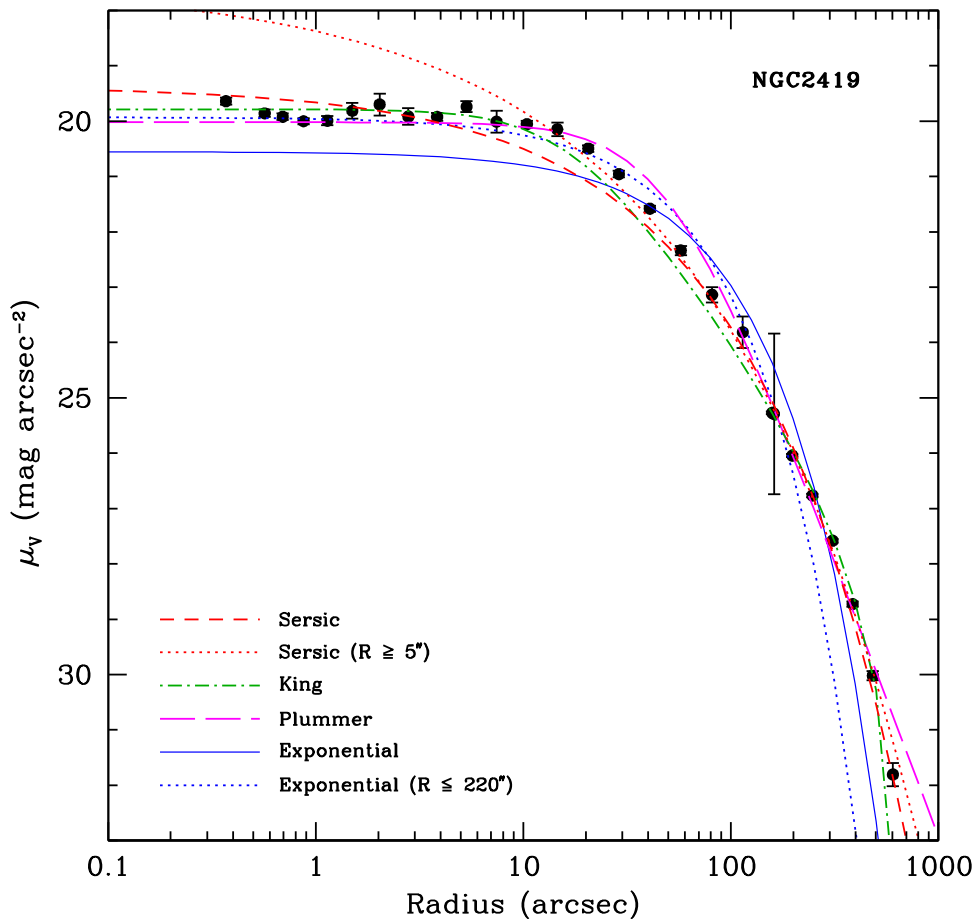


Figure 1. Surface brightness profile for NGC 2419, one of seven high surface brightness satellites in our sample for which our two-dimensional maximum-likelihood approach is not appropriate because of varying stellar completeness. This is a composite profile based on surface photometry in the core and star counts in the outer regions, matched via least-squares at intermediate radii. The smooth curves show the best-fit Sérsic, King, Plummer, and exponential models (red, green, magenta, and blue curves, respectively). For the Sérsic and exponential models, two models are shown: one that best fits the full profile (dashed and solid curves) and one that best fits the observed profiles over a restricted radial range, as indicated in the legend (dotted curves).

comparison between the best-fit Sérsic parameters (ellipticity, position angle, and effective or half-light radius) and those found using King, Plummer, or exponential models for the 37 objects fitted using our maximum-likelihood approach. There is generally good agreement between the different models.

4.2. Comparison with Previous Results

Although Section 4.4 presents a detailed comparison of our photometric and structural parameters to those in the literature for each object in our survey, it is useful to begin by comparing our measurements to those reported in the most widely used databases for dwarf galaxies and globular clusters.

4.2.1. McConnachie (2012)

The most extensive compilation of photometric and structural parameters for Local Group galaxies remains that of McConnachie (2012). This catalog includes basic information for about two dozen Galactic dwarf galaxies. Note that while the McConnachie catalog has been updated since publication, a number of the most recently discovered Galactic satellites—such as those uncovered in recent DES, Pan-STARRS, and Subaru imaging surveys—are not included in the current database.

In Figure 4, we compare our best-fit parameters to those tabulated in McConnachie (2012). Panels (a)–(d) show the results for four key parameters: absolute magnitude, M_V ; effective (or half-light) radius, R_e ; mean ellipticity, ϵ ; and central surface brightness, $\mu_{0,V}$. The dashed line in each panel shows the one-to-one relation. A total of 23 objects are shown in Figure 4, of which 15 and eight objects belong to our primary and secondary samples (blue and red symbols, respectively). Note that some caution must be exercised in these comparisons because the McConnachie (2012) measurements were standardized assuming exponential profiles, whereas our parameters come from the best-fit Sérsic models (cf. Section 4.1).

This caveat aside, the comparisons in Figure 4 show very good agreement apart from a few outliers. Most notably, our measured effective radii for Sextans and Ursa Minor differ significantly from those given in McConnachie (2012). For Sextans, we measure $R_e = 17'.67 \pm 0'.17$ —much smaller than the value of $27'.8 \pm 1'.2$ in McConnachie (2012). For Ursa Minor, we find $R_e = 17'.32 \pm 0'.11$, which is more than double the value of $8'.2 \pm 1'.2$ given in McConnachie (2012). In both cases, though, the McConnachie (2012) values were taken from the photographic survey of Irwin & Hatzidimitriou (1995).

Ursa Major I is a slight outlier in panel (c), where we measure an ellipticity of $\epsilon = 0.57 \pm 0.03$. This is significantly

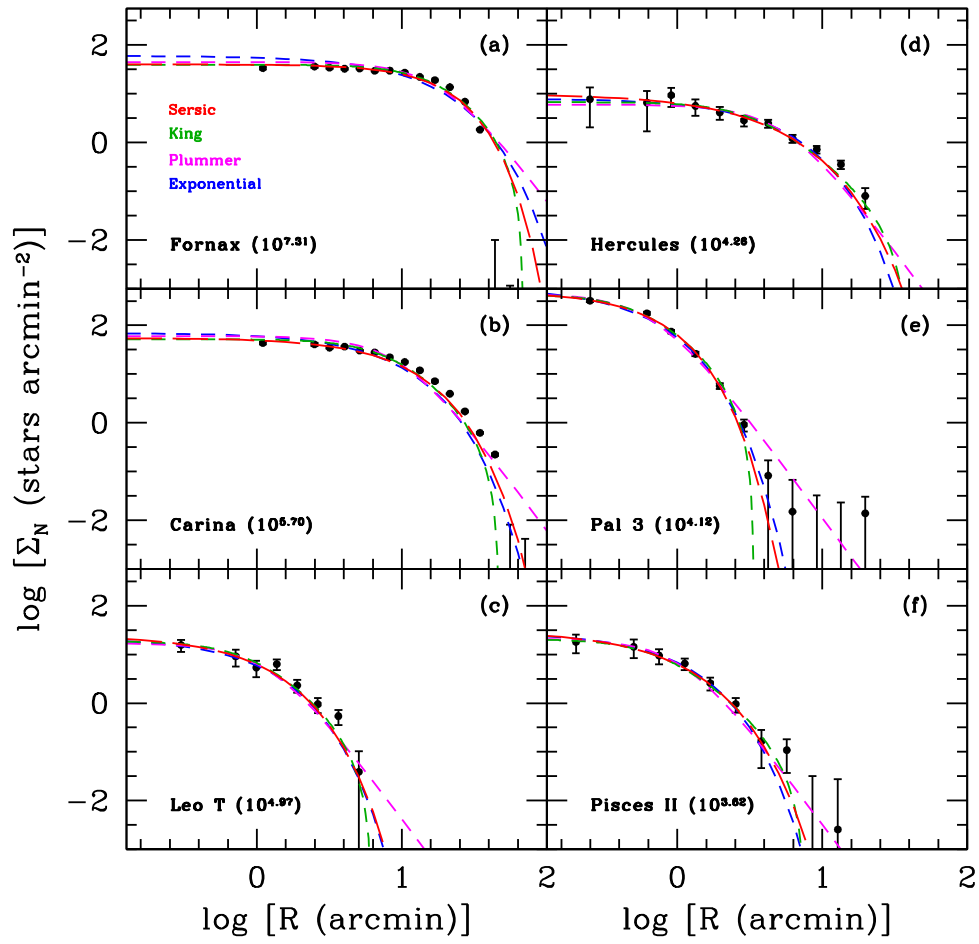


Figure 2. One-dimensional surface density profiles for six representative satellites from our survey. The subsample of objects shown here includes three classical dwarf galaxies (Fornax, Carina, and Leo T), a globular cluster (Palomar 3), and two ultra-faint dwarfs (Hercules and Pisces II). Total luminosities (given in parentheses) decrease monotonically from panels (a) to (f). In each panel, the best-fit (two-dimensional) Sérsic, King, Plummer, and exponential models are shown by the red, green, magenta, and blue profiles, respectively.

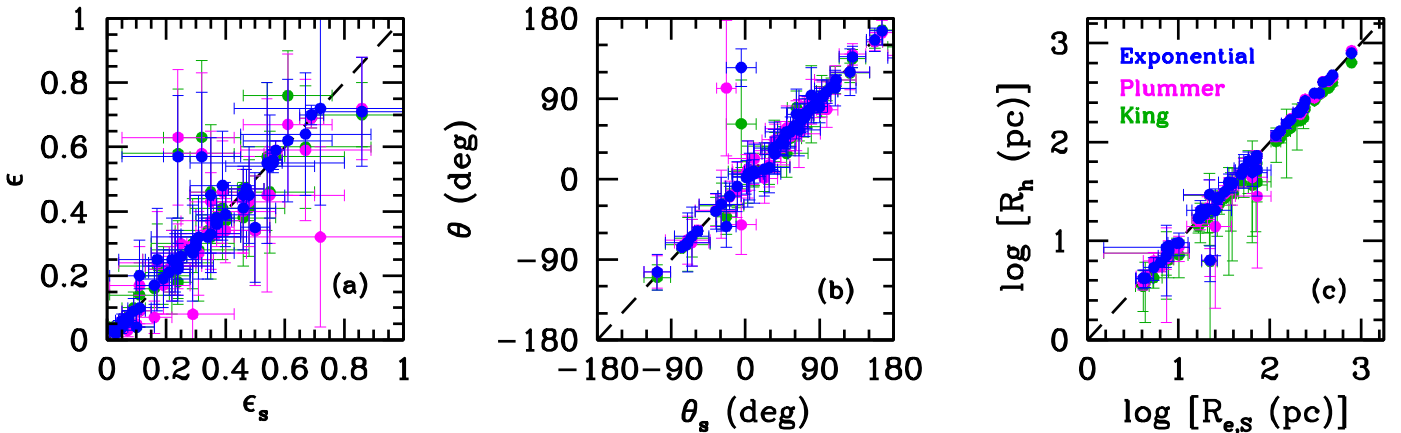


Figure 3. Comparison between the baseline Sérsic model parameters and those found assuming King, Plummer, and exponential models (green, magenta, and blue points, respectively). Panels (a)–(c) show results for ellipticity, position angle, and effective or half-light radius, respectively. The dashed line in each panel shows the one-to-one relation.

lower than the value of 0.80 ± 0.04 from McConnachie (2012), which is, in turn, based on relatively shallow SDSS star counts analyzed by Martin et al. (2008b). Using much deeper Suprime-Cam imaging, Okamoto et al. (2008b) found an ellipticity of 0.54, which is in excellent agreement with our value. Finally, in panel (d), we see a slight (1.2σ) discrepancy between our central surface brightness measurement for Leo V,

$\mu_{0,V} \simeq 24.9^{+0.90}_{-0.79}$ mag arcsec $^{-2}$, and that given in McConnachie (2012), $\mu_{0,V} \simeq 27.1 \pm 0.8$ mag arcsec $^{-2}$, which is based on the analysis of de Jong et al. (2010). The origin and significance of this disagreement are unclear, since the photometric catalogs used in our analysis and in de Jong et al. (2010) have comparable depth and areal coverage, although we note that Leo V is located at the field edge in the

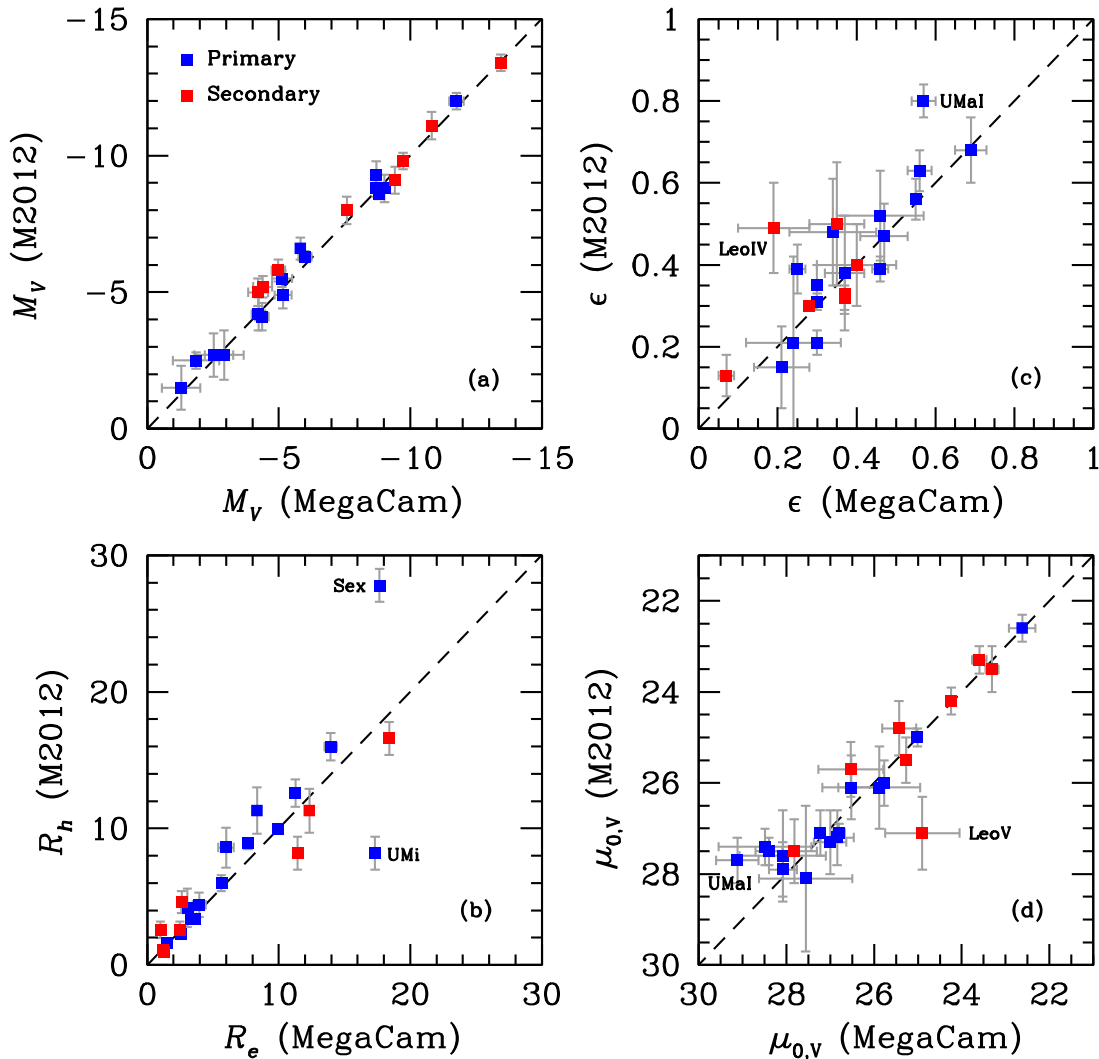


Figure 4. Comparison of the best-fit Sérsic photometric and structural parameters for “classic” and ultra-faint dwarf galaxies in our survey with parameters for Local Group dwarf galaxies taken from the compilation of McConnachie (2012). The four panels, beginning at the upper left, compare absolute V -band magnitude, ellipticity, half-light vs. effective radius, and central surface brightness. A total of 23 satellites are shown in this figure—15 and eight objects belonging to our primary and secondary samples, respectively.

latter study. We note that the analysis of Leo V by Sand et al. (2012) using deeper data yields a central surface brightness of $\mu_{0,V} \sim 26.3$.

4.2.2. Harris (1996, 2010)

The most widely used catalog of Galactic globular clusters is that of Harris (1996). Figure 5 compares our photometric and structural parameters for the 19 objects that appear in the 2010 version of this catalog. This comparison sample consists of 12 low surface brightness objects with parameters derived from our two-dimensional maximum-likelihood method (Section 3.1) and seven high surface brightness objects whose parameters were derived from a one-dimensional analysis as described in Section 3.3. Filled and open squares indicate the low and high surface brightness clusters, respectively.

As was the case in Figure 4, the four panels of this figure show absolute magnitude, M_V ; effective (or half-light) radius, R_e ; mean ellipticity, ϵ ; and central surface brightness, $\mu_{0,V}$. Note that most of the Harris magnitude, size, and surface brightness measurements are, in fact, taken from the study of McLaughlin & van der Marel (2005), who fitted King models

to the (rather heterogeneous) star count and surface brightness data of Trager et al. (1995). For the remote halo clusters that are the focus of this study, the Trager et al. (1995) profiles often come from a variety of photographic, photoelectric, and CCD sources, sometimes taken in different filters and having differing depths and resolution.

For the most part, we find reasonable agreement between our Sérsic measurements and those tabulated in the Harris (1996) catalog. In terms of absolute magnitude, there is quite good agreement, although our magnitude for Palomar 2 ($M_V \simeq -9$) is significantly brighter than the Harris (1996) value ($M_V \simeq -8$). However, integrated light measurements for this object are problematic given its low Galactic latitude ($b \simeq -9^\circ$) and large and variable reddening. The two sets of ellipticity measurements are also in good agreement, although Harris (1996) reported a rather high ellipticity, $\epsilon = 0.24$, for NGC 7492. We find a much smaller value, $\epsilon = 0.02 \pm 0.02$, as would be expected from the round isopleths derived in Section 4.3.1.

Care must be taken when comparing central surface brightness measurements. The values given in Harris (1996)

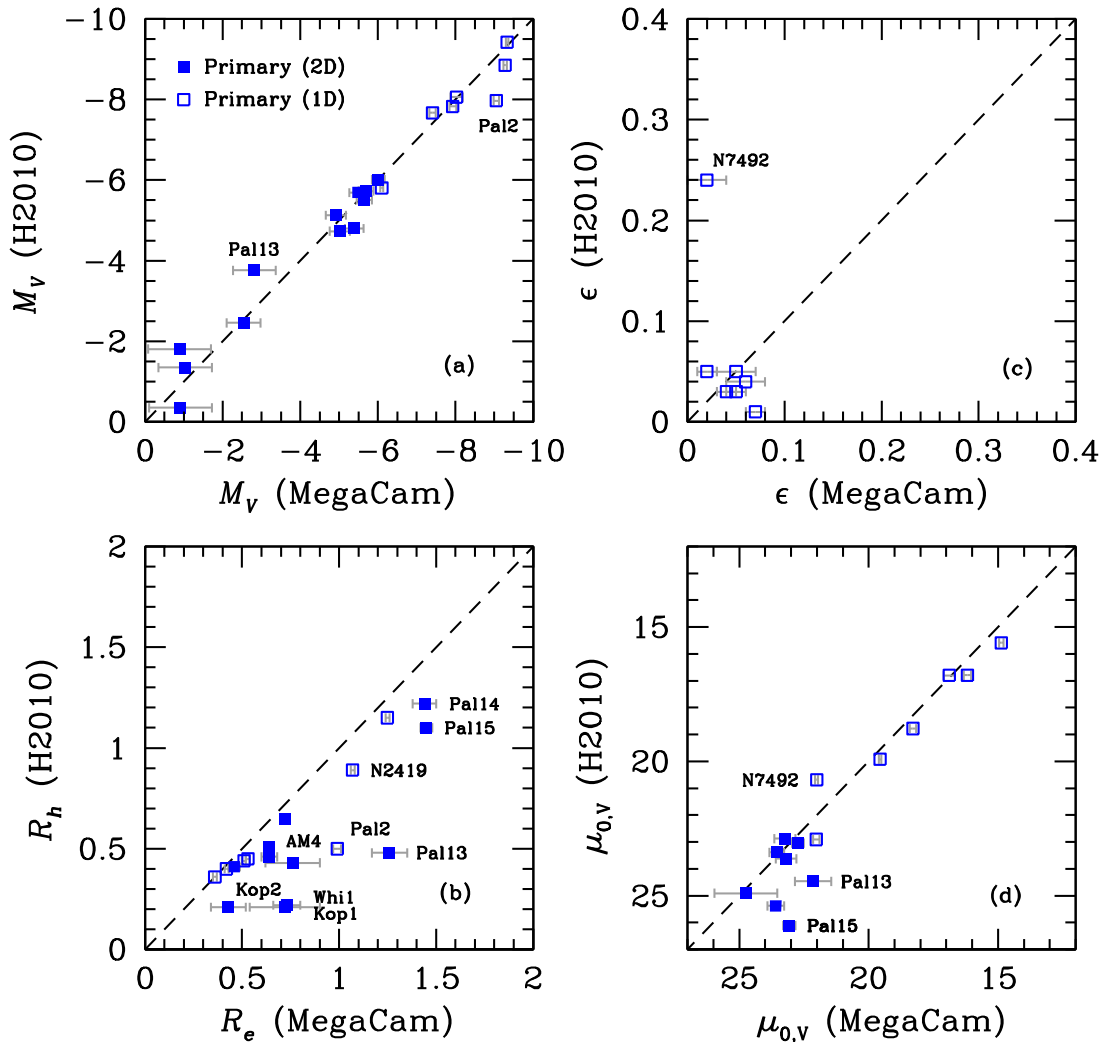


Figure 5. Comparison of the best-fit Sérsic photometric and structural parameters for halo clusters in our survey with those in the 2010 version of the Harris (1996) catalog of Galactic globular clusters. The four panels, beginning at the upper left, compare absolute V -band magnitudes, ellipticities, King half-light vs. Sérsic effective radius, and central surface brightness. A total of 19 globular clusters are shown in this figure.

are based on King model fits, which have isothermal cores, so these may not be directly comparable to the inward extrapolations of Sérsic models (i.e., the values reported in Table 6). For the seven high surface brightness clusters, we therefore rely on median (nonparametric) values within a radius of $5''$. All in all, there is reasonable agreement between the surface brightness measurements, although our values for Palomar 13, 14, and 15 are somewhat brighter than suggested by the earlier Trager et al. (1995) data. We note that, in the case of Palomar 13, our estimate of $\mu_{0,V} \simeq 22.15 \pm 0.70$ mag arcsec $^{-2}$ is in agreement with the value of $\mu_{0,V} = 22.54^{+0.20}_{-0.17}$ mag arcsec $^{-2}$ given in Côté et al. (2002).

Finally, Figure 5 shows that our effective radii are often larger than the half-light values reported in Harris (1996). The most discrepant objects are Whiting 1 ($0'.73$ versus $0'.22$), Koposov 1 ($0'.72$ versus $0'.21$), Palomar 13 ($1'.26$ versus $0'.48$), Palomar 2 ($0'.99$ versus $0'.5$), and AM 4 ($0'.76$ versus $0'.43$). We have carefully inspected our fits and found that the larger values are in fact much more consistent with the deeper Megacam data than the Harris ones. In the case of Whiting 1 and AM 4, the Harris value was taken from Carraro et al. (2007) and Carraro (2009), respectively. In both cases, the light distribution appeared to extend out to several arcminutes

following a shallow slope in the outer region and was thus fitted using a King-plus-power law profile to account for the extended light distribution. Our photometry is at least 2 mag deeper in both cases. We do not see an obvious break in the light distribution and, consequently, our best-fit Sérsic profiles yield larger half-light radii. In Palomar 2, the central stellar density is severely affected by a dust lane crossing the cluster, which significantly modifies the light distribution, especially that of the brighter stars. To derive its structural parameters, we excluded the brighter giants, which results in a larger half-light radius.

The case of Palomar 13 is interesting: our effective radius is roughly three times larger than the Harris value, though we note that the Harris half-light radius was not measured directly but instead estimated based on the cluster's core radius following the expression $\log(r_h/r_c) = 0.6c - 0.4$, where c is the concentration index. Our best-fit King core radius is $r_c \sim 0'.31$, which is similar to previous determinations (Siegel et al. 2001; Côté et al. 2002). We conclude that our larger effective radius is due to the fact that a King profile is not a good description of Palomar 13's unusual surface brightness profile distribution, which is better matched by a Sérsic profile with a larger effective radius.

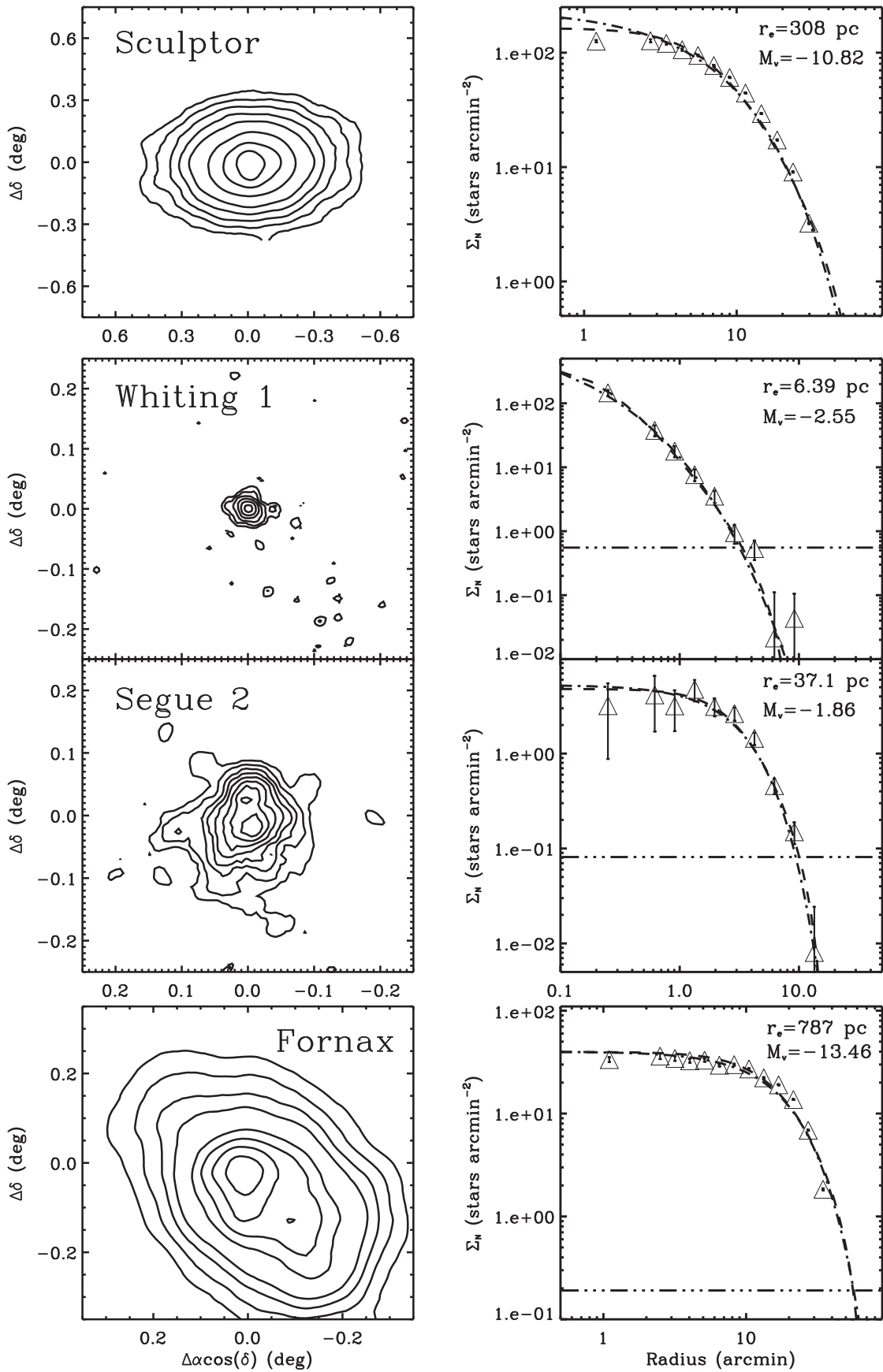


Figure 6. Isodensity contour maps (left panels) and radial number density profiles (right panels) for four of our program objects: Sculptor, Whiting 1, Segue 2, and Fornax. For the number density profiles, the dashed and dot-dashed curves show the best-fit King and Sérsic models, while the horizontal line in each panel shows the fitted background level. Note that these one-dimensional profiles were produced using the best-fit parameters from the maximum-likelihood analysis and do not represent the best-fit parameters for the binned number density profiles.

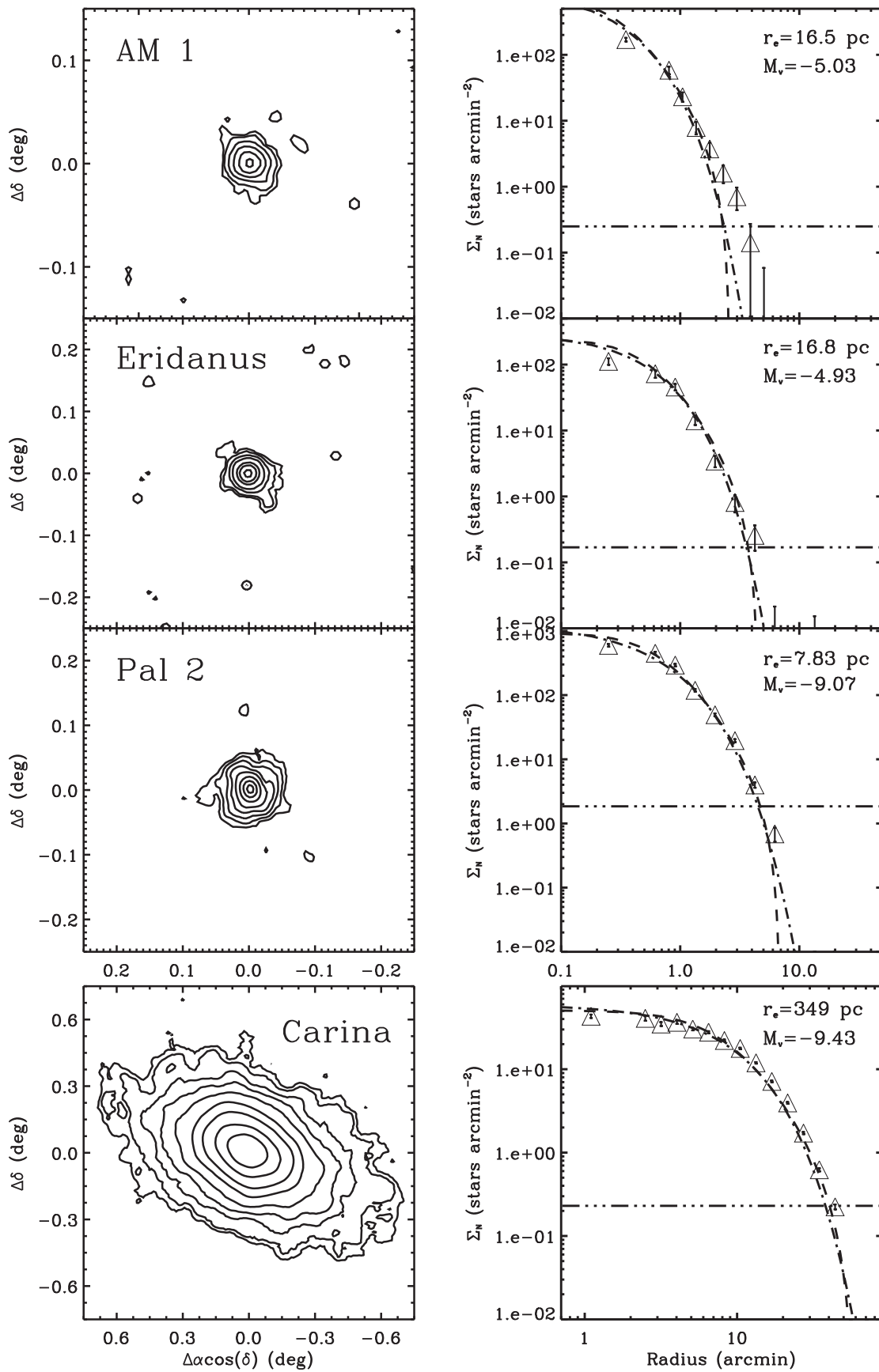


Figure 7. Same as Figure 6 but for AM 1, Eridanus, Palomar 2, and Carina.

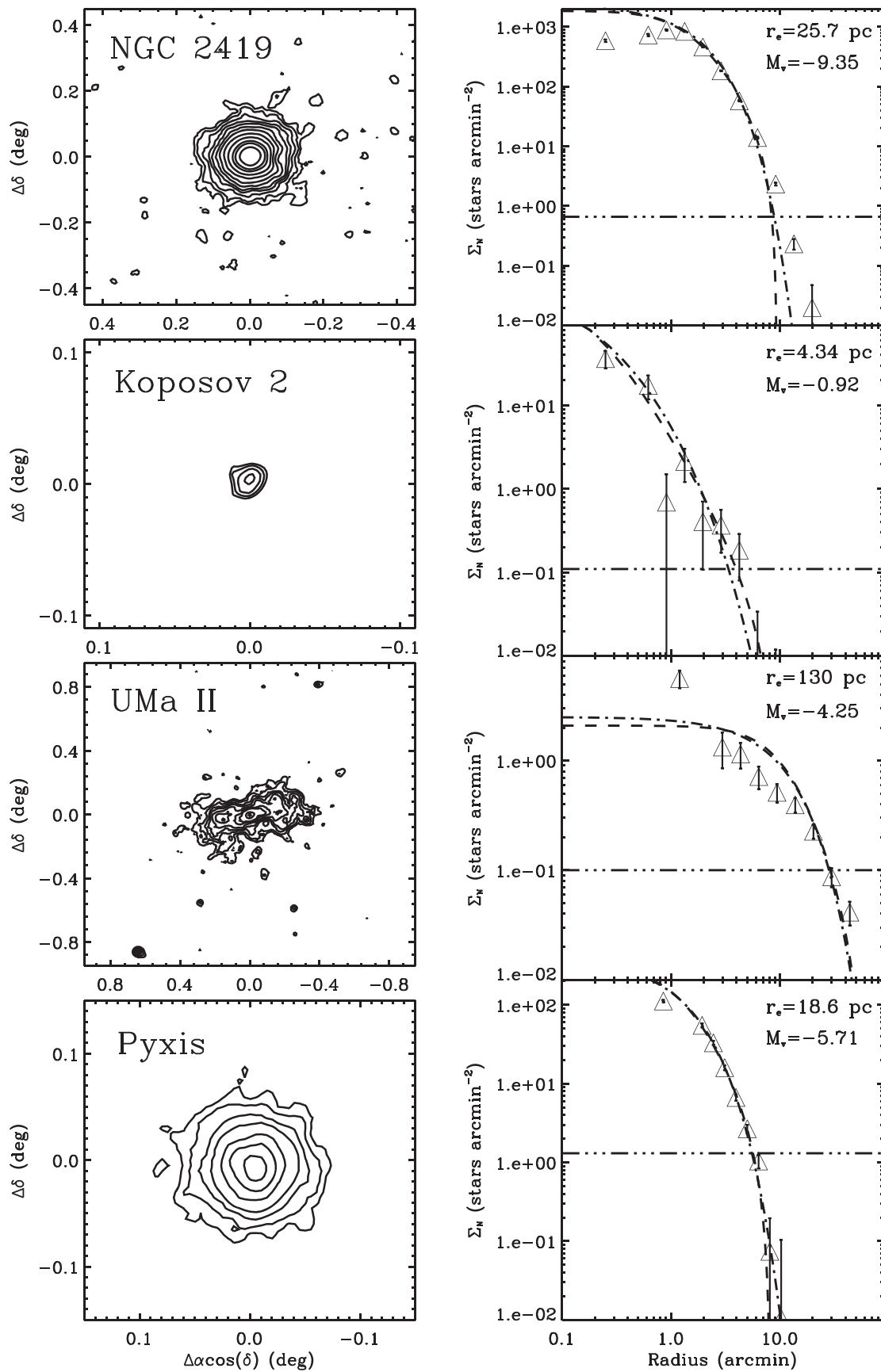


Figure 8. Same as Figure 6 but for NGC 2419, Koposov 2, Ursa Major II, and Pyxis.

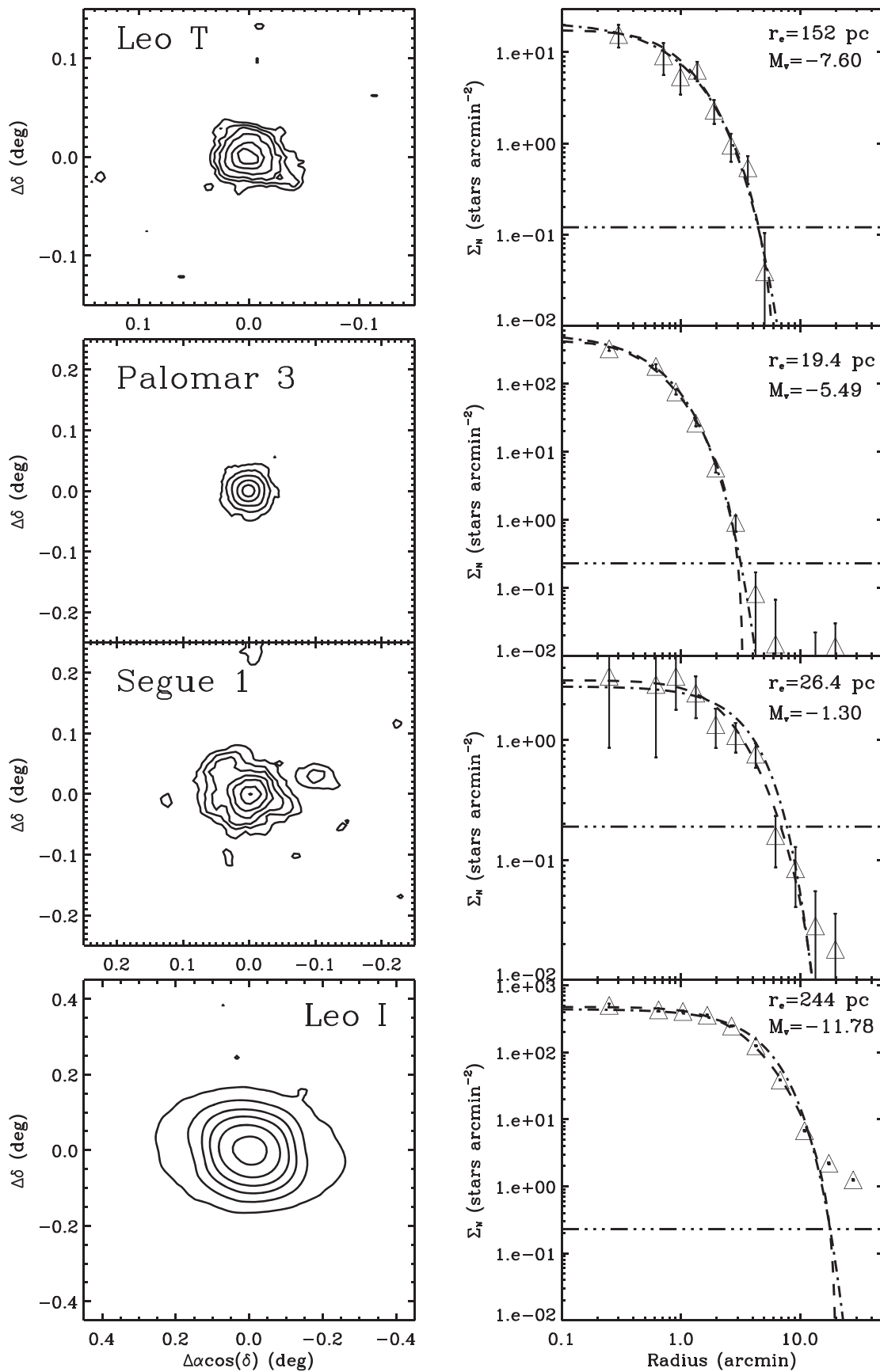


Figure 9. Same as Figure 6 but for Leo T, Palomar 3, Segue 1, and Leo I.

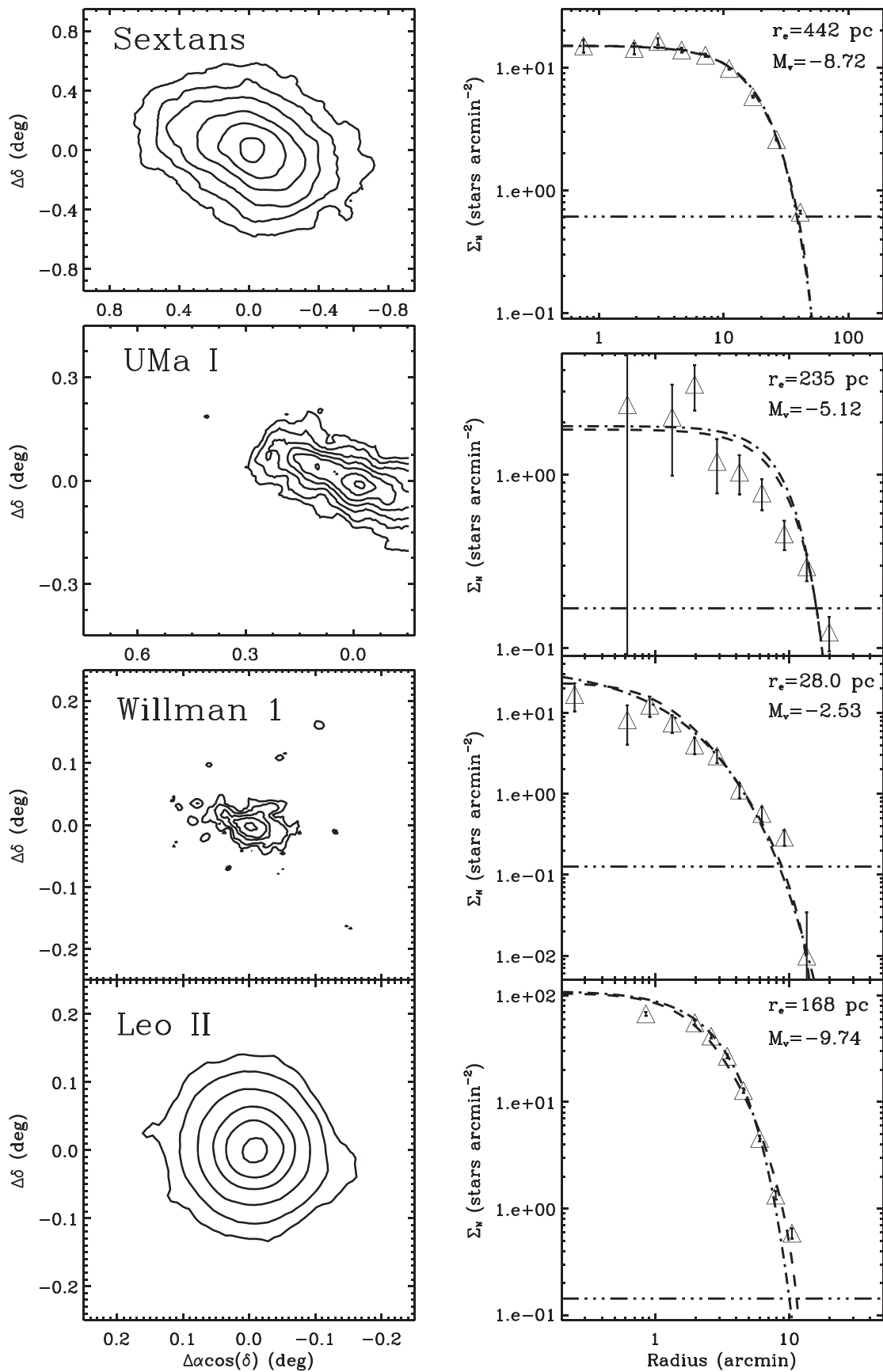


Figure 10. Same as Figure 6 but for Sextans, Ursa Major I, Willman 1, and Leo II.

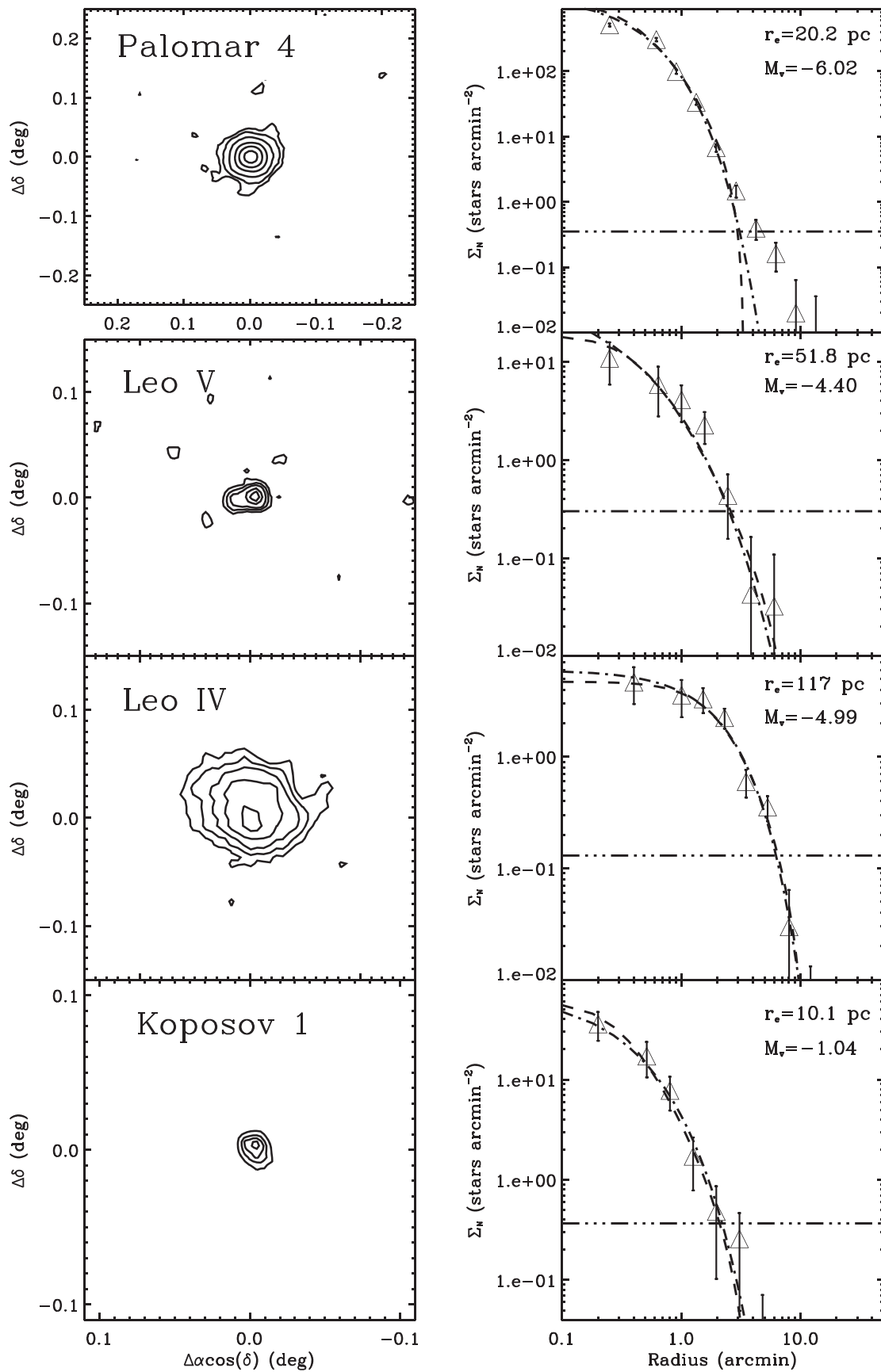


Figure 11. Same as Figure 6 but for Palomar 4, Leo V, Leo IV, and Kaposov 1.

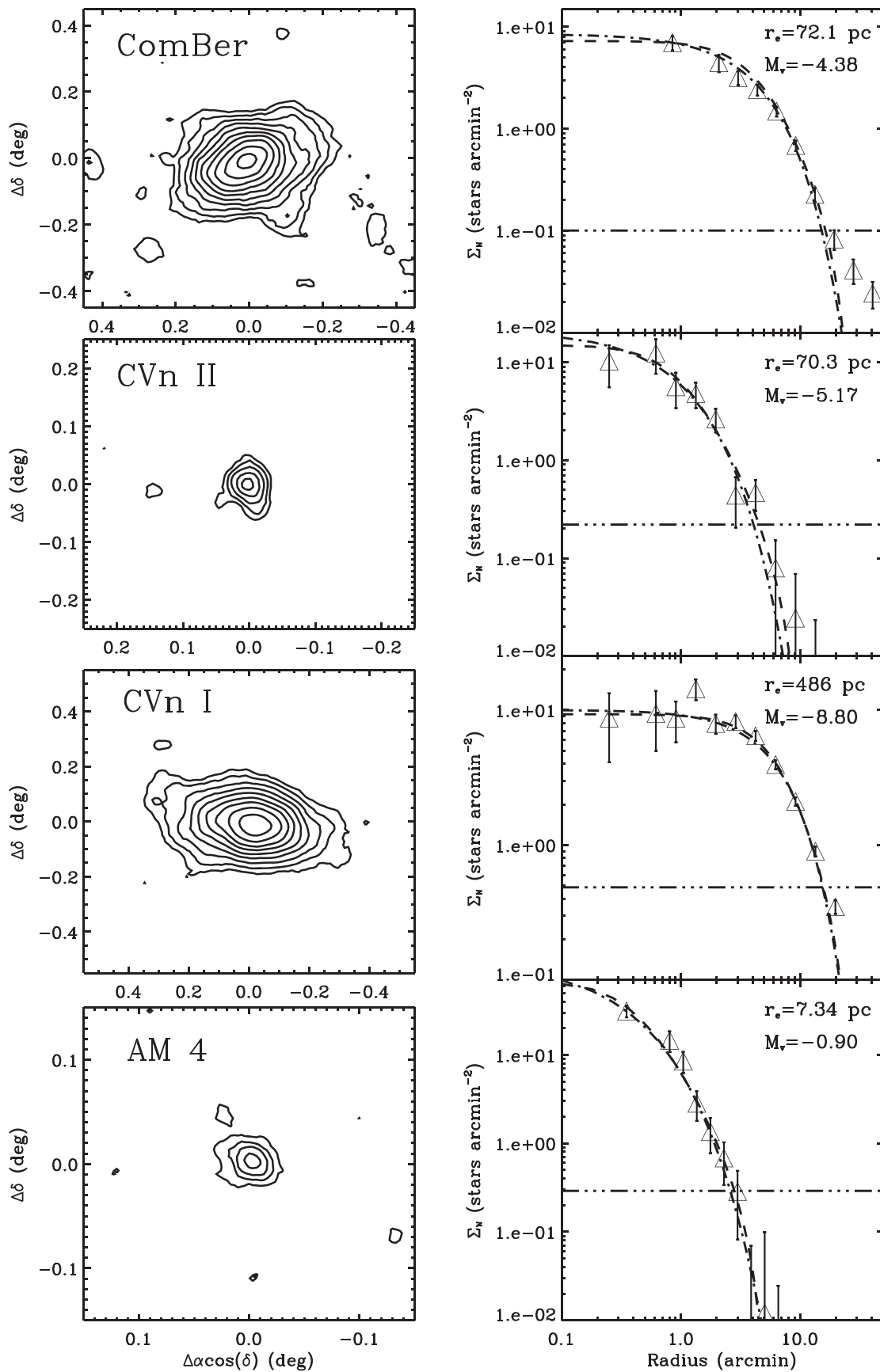


Figure 12. Same as Figure 6 but for Coma Berenices, Canes Venatici II, Canes Venatici I, and AM 4.

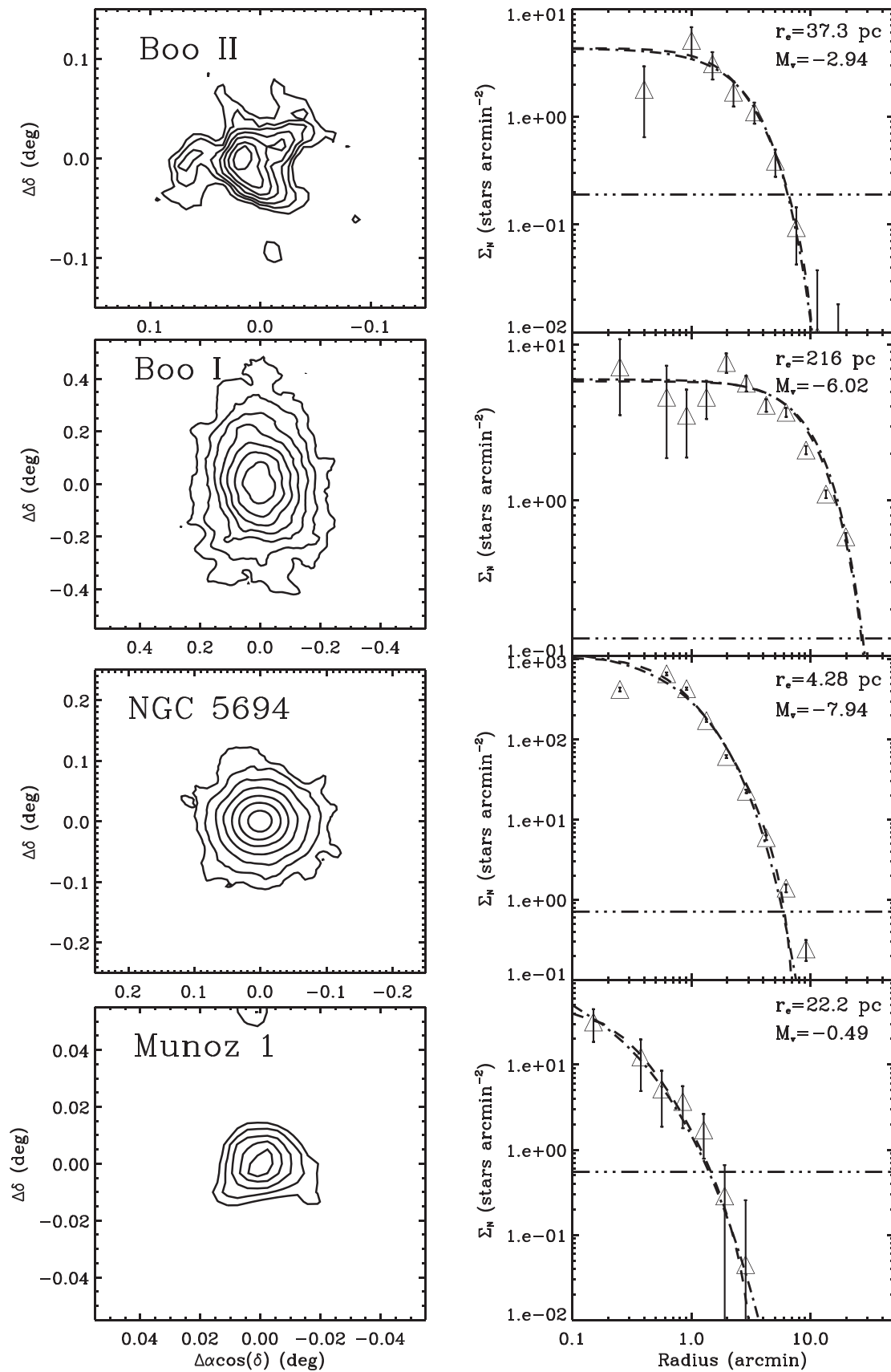


Figure 13. Same as Figure 6 but for Boötes II, Boötes I, NGC 5694, and Muñoz 1.

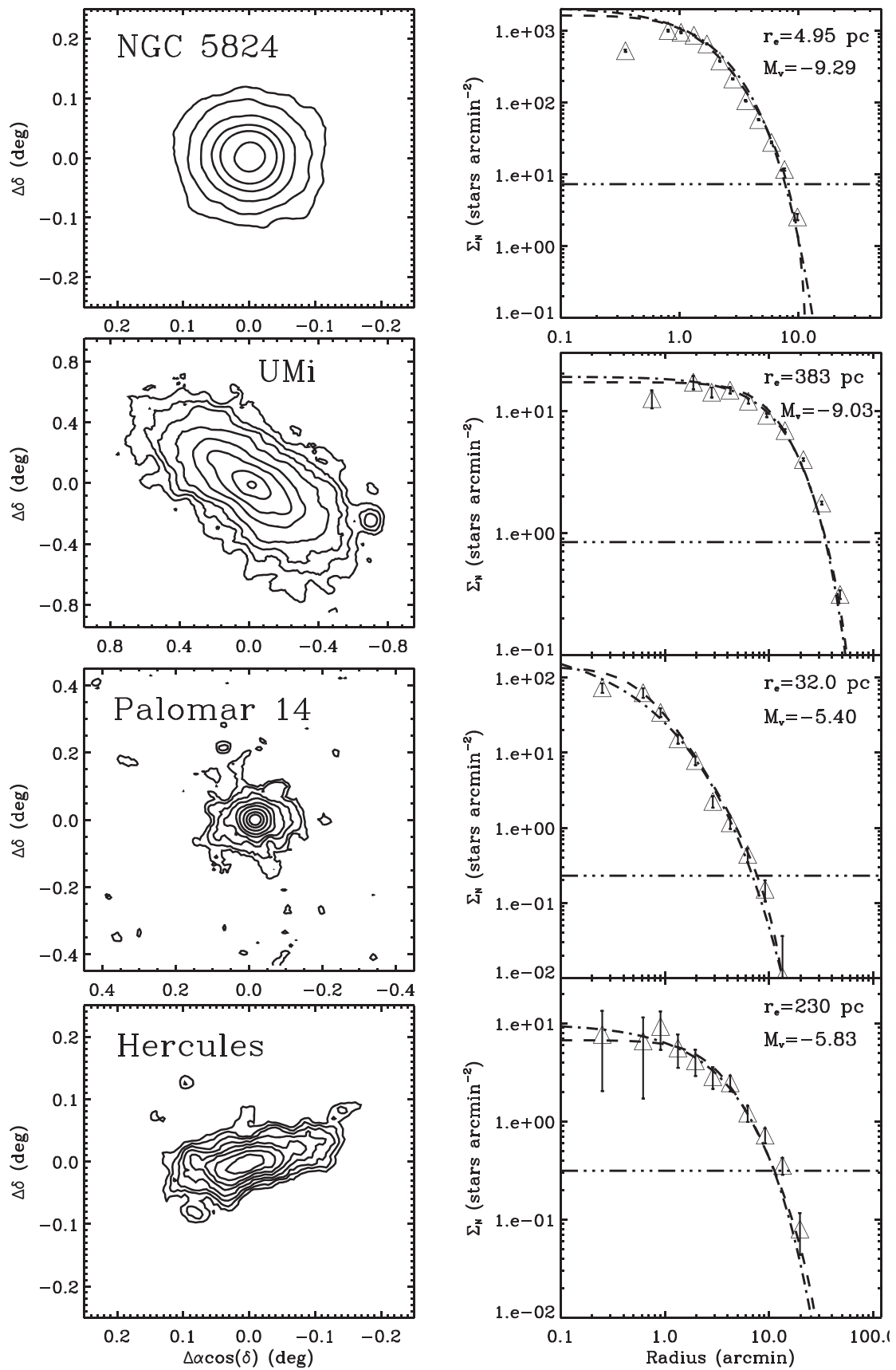


Figure 14. Same as Figure 6 but for NGC 5824, Ursa Minor, Palomar 14, and Hercules.

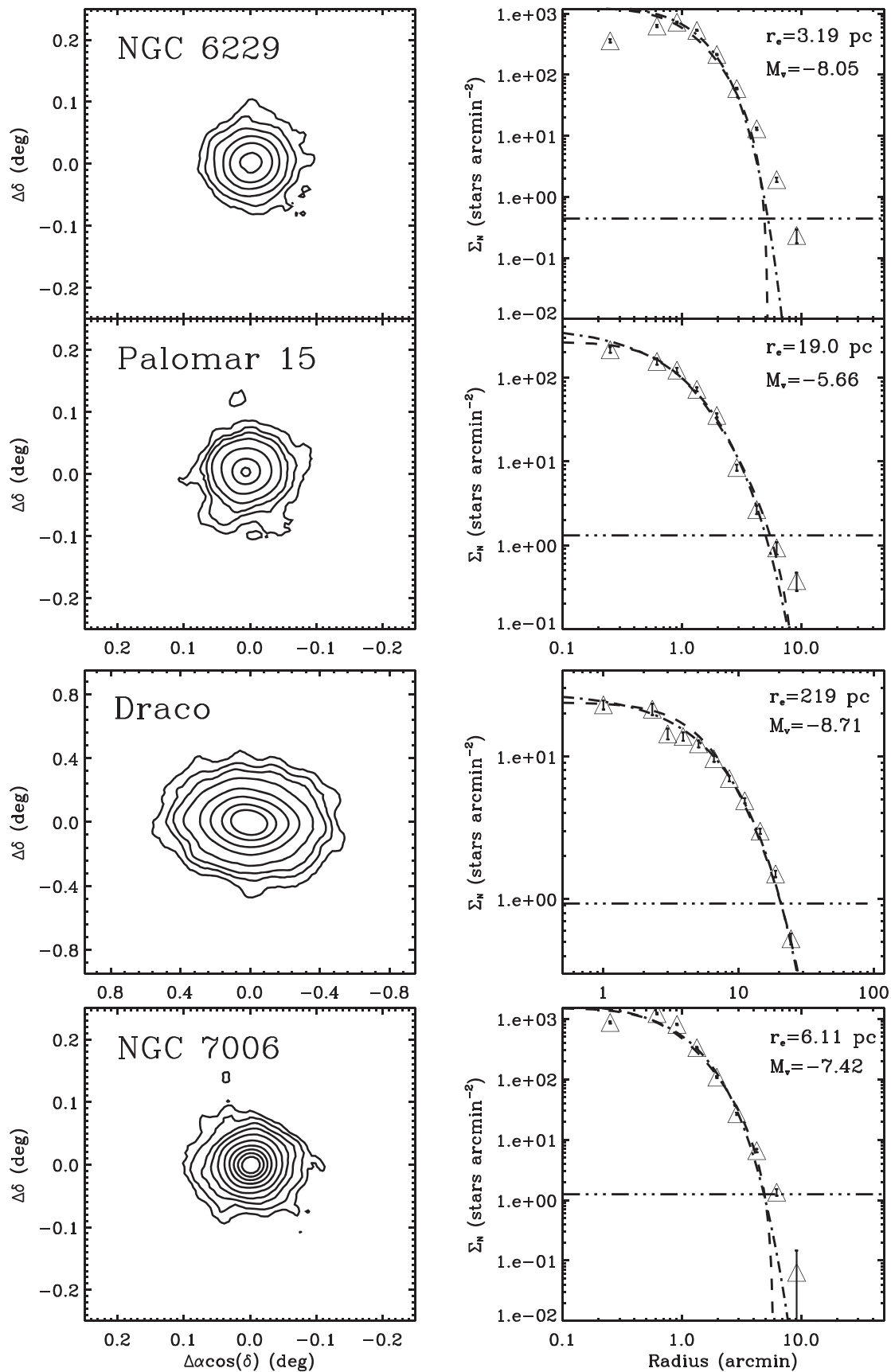


Figure 15. Same as Figure 6 but for NGC 6229, Palomar 15, Draco, and NGC 7006.

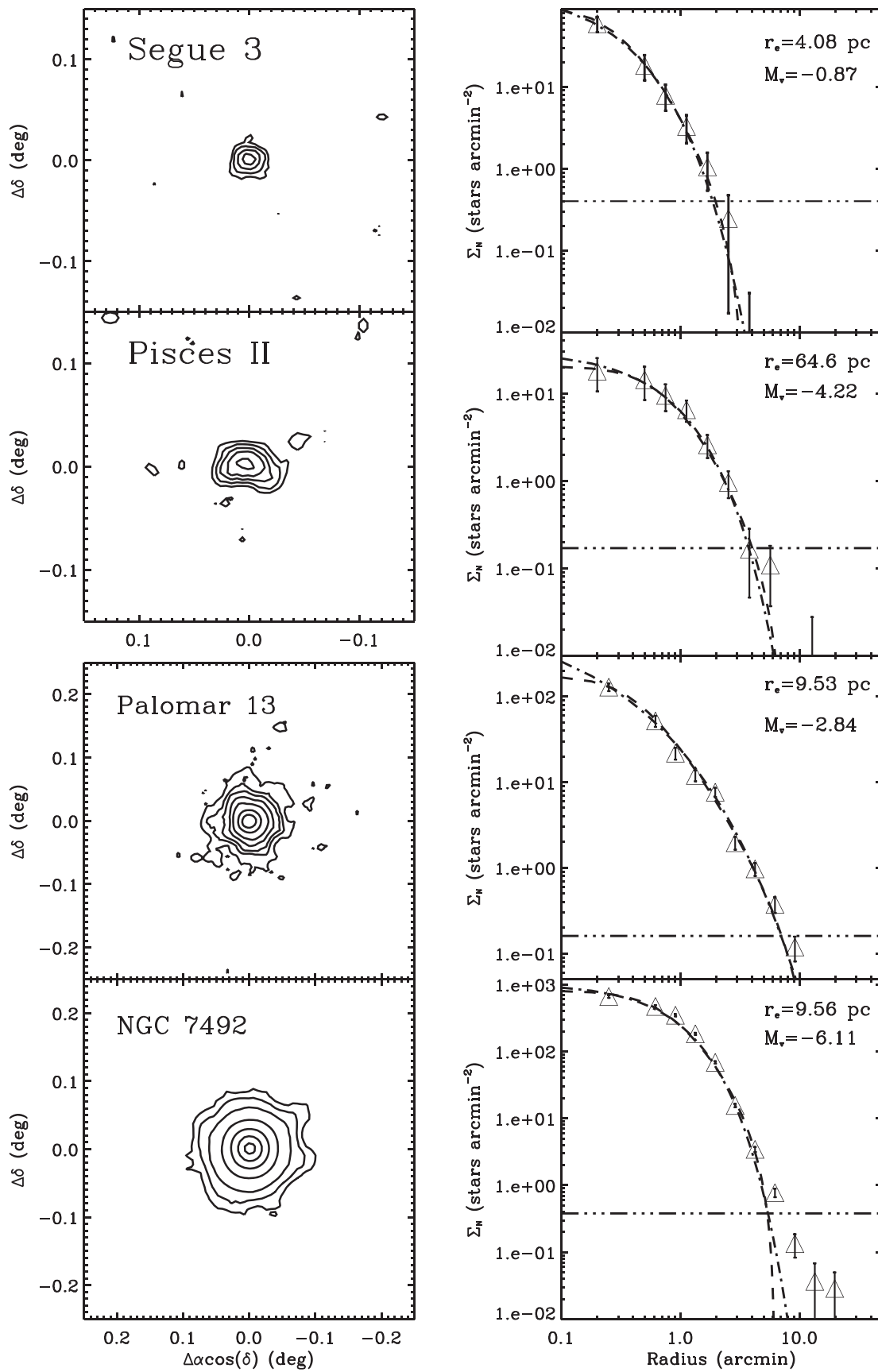


Figure 16. Same as Figure 6 but for Segue 3, Pisces II, Palomar 13, and NGC 7492.

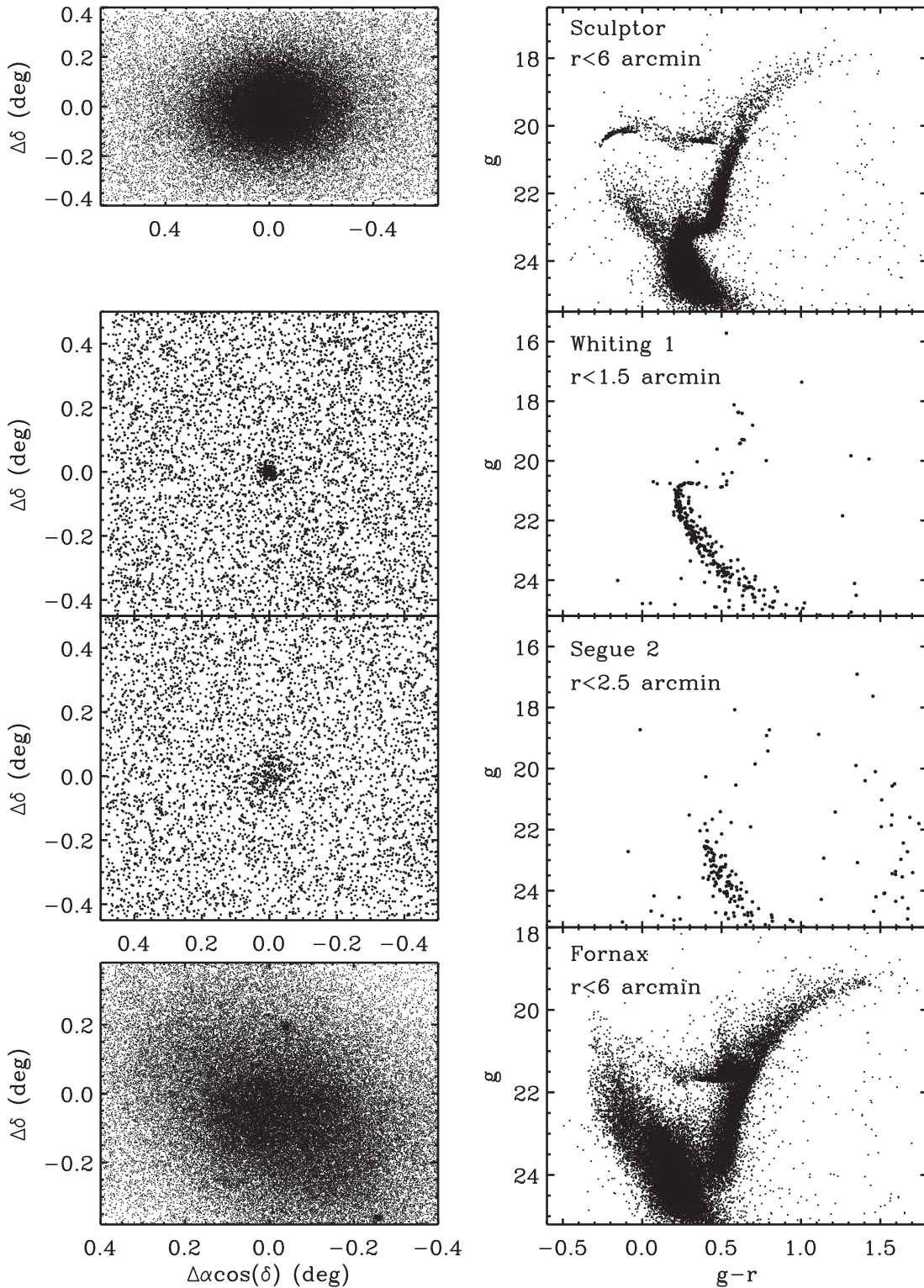


Figure 17. Star-count maps (left panels) and CMDs (right panels) for four of our program objects: Sculptor, Whiting 1, Segue 2, and Fornax.

4.3. Diagnostic Tools for Program Objects

The stellar catalogs generated from our wide-field gr images form the basis of our maximum-likelihood analysis and can be used not only to estimate photometric and structural parameters but also to help us understand the nature of each program object. Here we briefly describe the diagnostic tools used to analyze each satellite.

4.3.1. Isodensity Contour Maps and One-dimensional Density Profiles

To examine the two-dimensional morphologies of our program objects in a systematic way, we created smoothed isodensity contour maps using the same “cleaned” photometric catalogs that were used to derive structural parameters. These catalogs consist of star-like objects identified by applying DAOPHOT χ and sharp cuts and selected to fall in regions of the CMD delineated by the

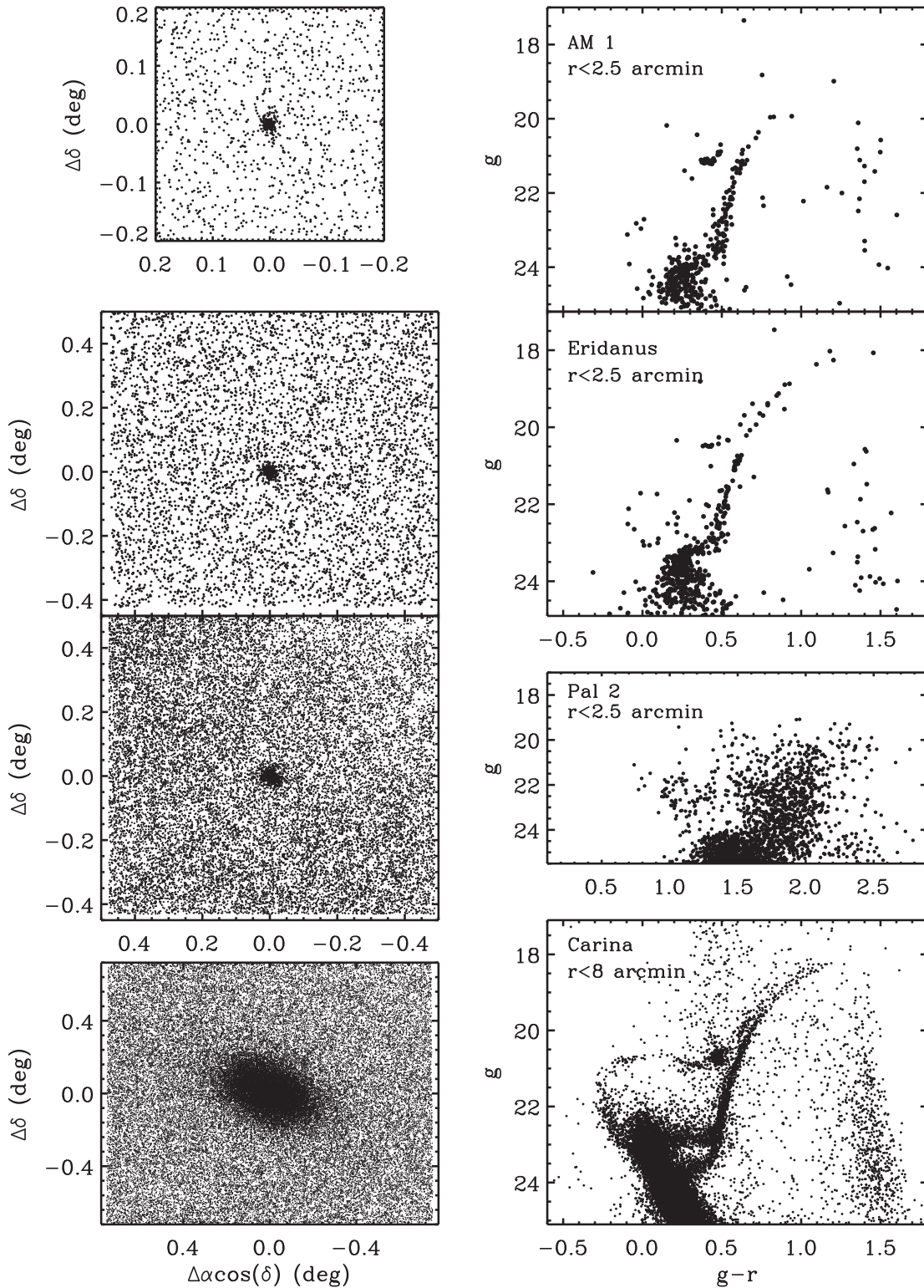


Figure 18. Same as Figure 17 but for AM 1, Eridanus, Palomar 2, and Carina.

adopted best-fit isochrone. For objects with more than one star formation episode, like some of the classical dwarf galaxies, we also included stars that fall in other regions of the CMD that were not covered by the best-fitting isochrone.

To construct density maps, we count stars in bins that are subsequently spatially smoothed with an exponential filter. The bin size and scale of the smoothing exponential vary depending on the

angular size of the object and range from $40'' \times 40''$ bins for the classical dwarfs to $10'' \times 10''$ bins for the most compact satellites. The resulting contour maps are shown in the left panels of Figures 6–16 and are discussed on a case-by-case basis in Section 4.4.

Using the photometric and structural parameters derived in Section 3, we can also generate radial stellar density profiles for all objects. The stellar densities were measured by counting stars

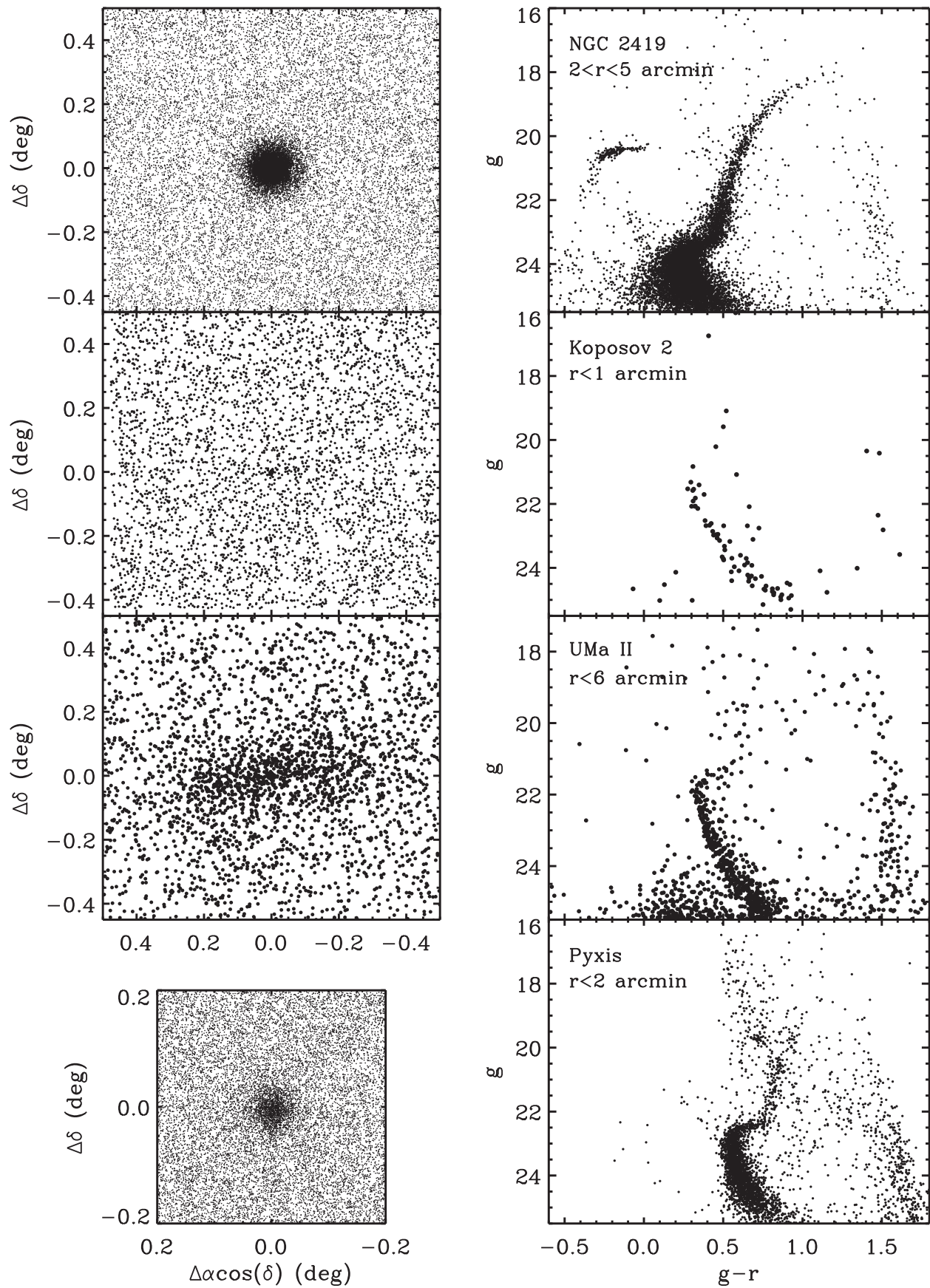


Figure 19. Same as Figure 17 but for NGC 2419, Koysov 2, Ursa Major 2, and Pyxis.

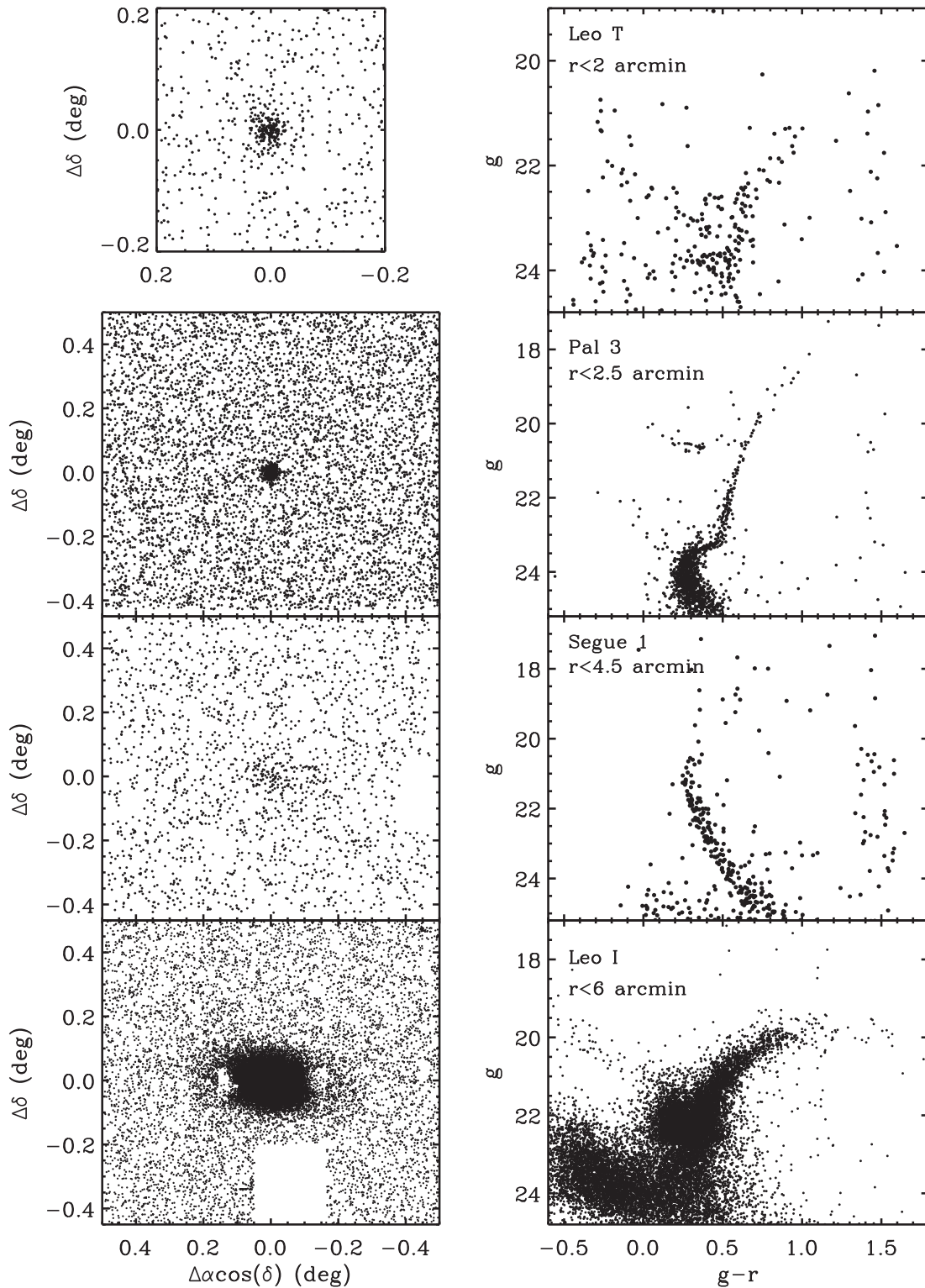


Figure 20. Same as Figure 17 but for Leo T, Palomar 3, Segue 1, and Leo I.

within concentric annuli of fixed ellipticity centered around α_0 and δ_0 and oriented according to the derived position angle θ . Uncertainties were calculated from Poisson statistics. The right panels of Figures 6–16 show background-subtracted, one-dimensional density profiles for all objects, as well as the respective best-fit King and Sérsic models. We remind the reader that these are not profiles fitted to the binned densities but generated with the parameters derived using all of the detected stars.

4.3.2. Star-count Maps and CMDs

For completeness, we show in the left panels of Figures 17–27 star-count maps for the individual satellites. Although the isodensity contour maps shown in Figures 6–16 are based on star-count maps, the latter have not been smoothed and so offer a different perspective on the two-dimensional structure of each satellite. In the right panels of Figures 17–27,

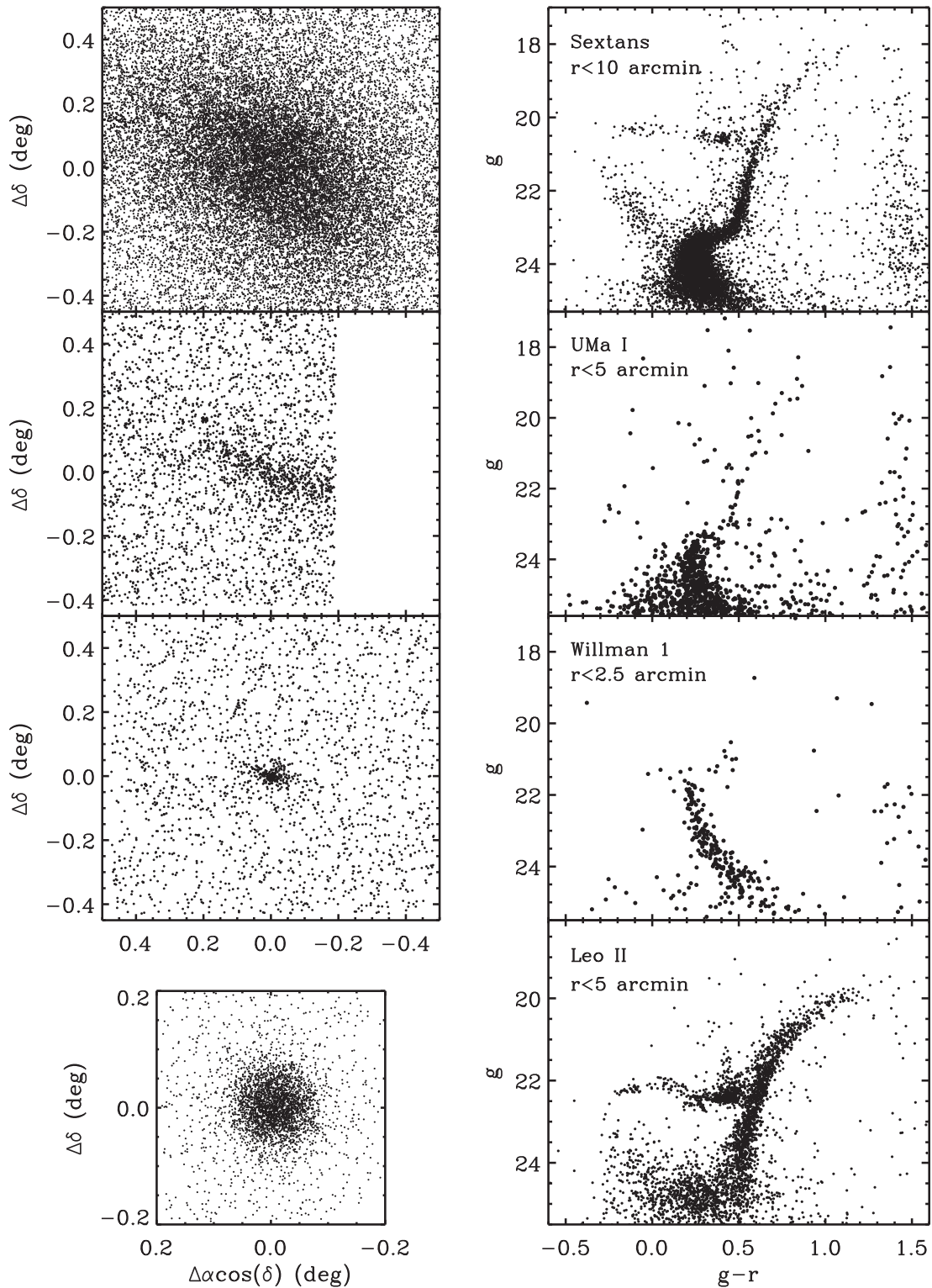


Figure 21. Same as Figure 17 but for Sextans, Ursa Major 1, Willman 1, and Leo II.

we show the CMDs for our program objects constructed from the catalog of star-like sources identified in each object.

4.4. Analysis of Individual Systems

In the following subsections, we briefly summarize the results shown in Figures 6–27 for each of the 44 objects in our primary sample, highlighting some relevant aspects of the

individual targets. The systems are ordered in terms of increasing R.A.

4.4.1. Sculptor

Sculptor was the first of the Milky Way’s dSph galaxies to be discovered (Shapley 1938a). Hodge (1961) carried out the first detailed star-count analysis of this satellite, finding a

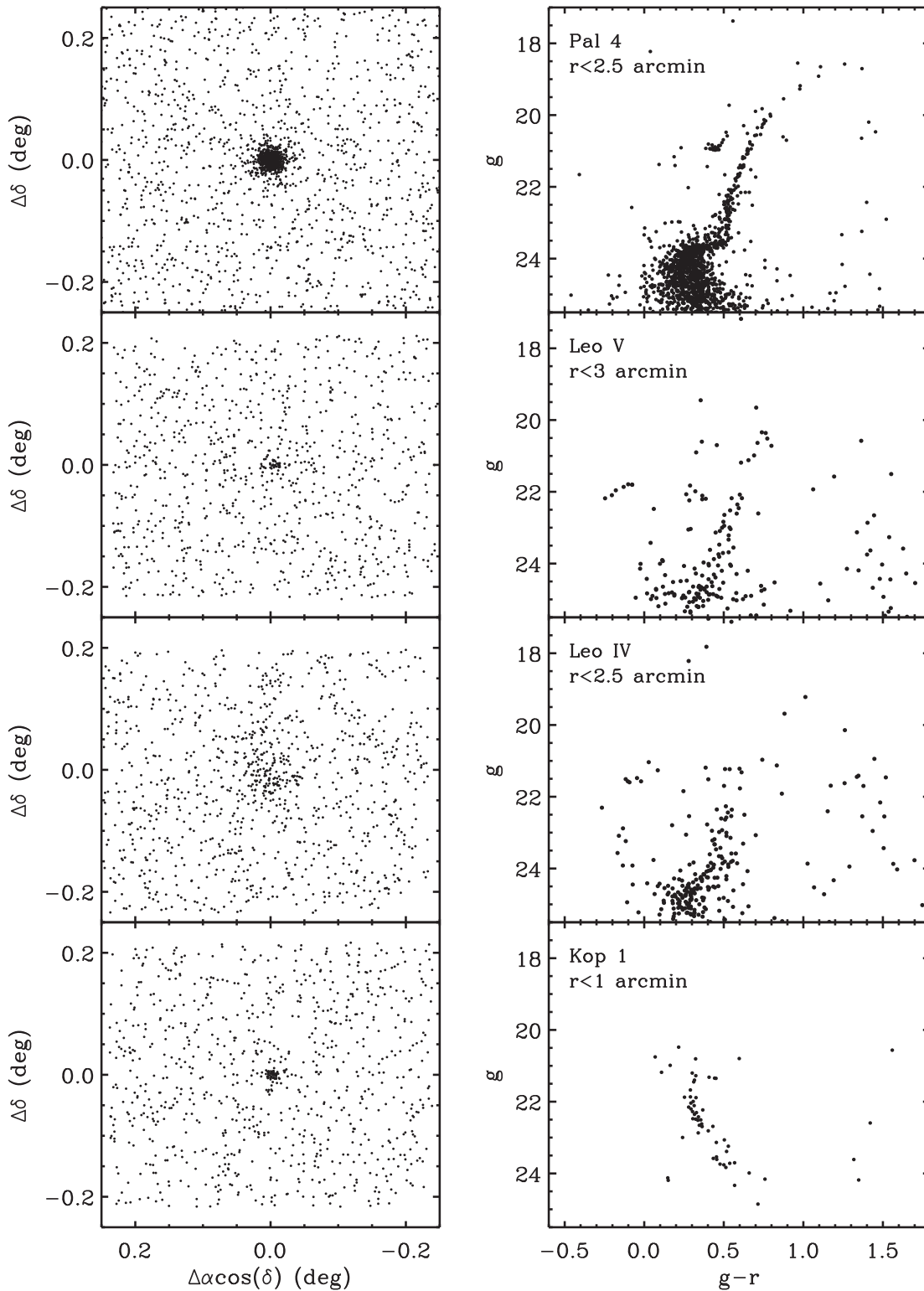


Figure 22. Same as Figure 17 but for Palomar 4, Leo V, Leo IV, and Kaposov 1.

smooth, slightly elongated distribution of stars that did not follow the models traditionally used to describe the luminosity profiles of elliptical galaxies.

More recently, Coleman et al. (2005) carried out a $3^{\circ}.1 \times 3^{\circ}.1$ wide-field survey centered on Sculptor and studied its outer structure, finding at most a mild level of tidal interaction with the Milky Way. In our survey, Sculptor was

imaged using the Clay-MegaCam in a 2×4 mosaic configuration yielding a total field of view of $0^{\circ}.8 \times 1^{\circ}.6$ (see Figure 17). This coverage barely reaches to the system’s King tidal radius, which, as shown by Muñoz et al. (2012b), limits our ability to derive reliable structural parameters using a maximum-likelihood method (since the background number density is one of the fitted parameters). Nevertheless, we

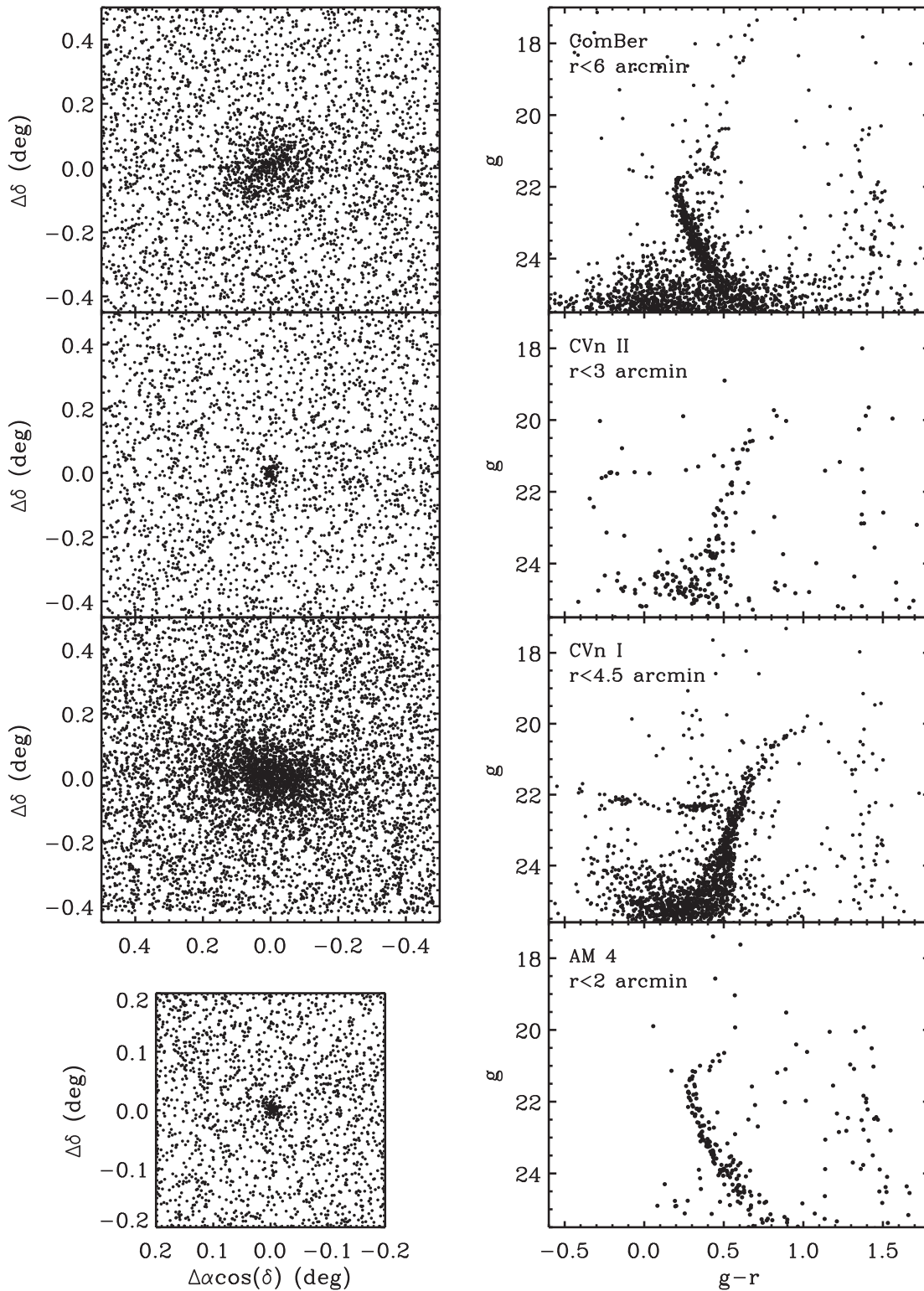


Figure 23. Same as Figure 17 but for Coma Berenices, Canes Venatici II, Canes Venatici I, and AM 4.

measure structural parameters consistent with the values previously published for this satellite (e.g., Irwin & Hatzidimitriou 1995). Figure 17 also shows the CMD of Sculptor’s inner $10'$, which reaches to $g \simeq 26$, or more than 2 mag below the MSTO. Combined with our spatial coverage, this represents the deepest and widest photometry currently available for this galaxy.

The upper right panel of Figure 6 shows the number density profile for Sculptor, while the upper left panel shows its isodensity contour map. Its one-dimensional profile is well described by a Sérsic profile of index $n_s = 0.74$. Our measured ellipticity of $\epsilon = 0.37$ (for a Sérsic model) is somewhat higher than the value of 0.32 from Irwin & Hatzidimitriou (1995). It is worth noting that, in

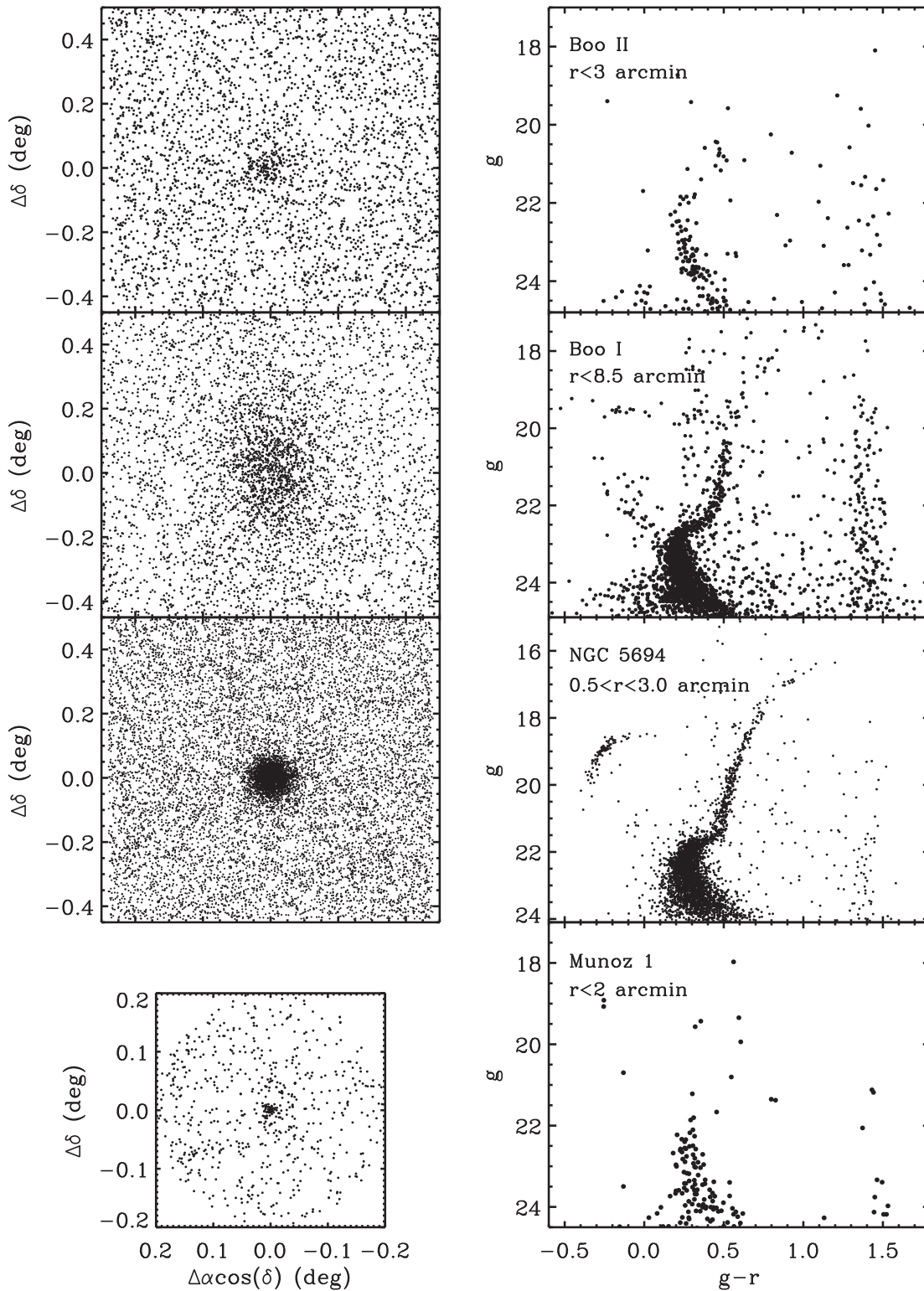


Figure 24. Same as Figure 17 but for Boötes II, Boötes I, NGC 5694, and Muñoz 1.

the structural study by Westfall et al. (2006), the ellipticity was found to range between 0.23 and 0.49, depending on the adopted stellar subsample, with deeper samples leading to lower ellipticities. In terms of its two-dimensional morphology, Sculptor shows an elongated but otherwise regular morphology, with no obvious signs of internal substructure or evidence of significant Galactic tidal disturbance. This finding is in line with previous studies.

4.4.2. Whiting 1

Discovered by Whiting et al. (2002), Whiting 1 is the youngest outer halo globular cluster thought to be associated with the Sgr dSph galaxy (Carraro 2005; Carraro et al. 2007; Law & Majewski 2010). Sparsely populated and originally classified as an open cluster (Dias et al. 2002), Whiting 1 is located at $R_{\odot} \sim 30$ kpc with an estimated age and metallicity

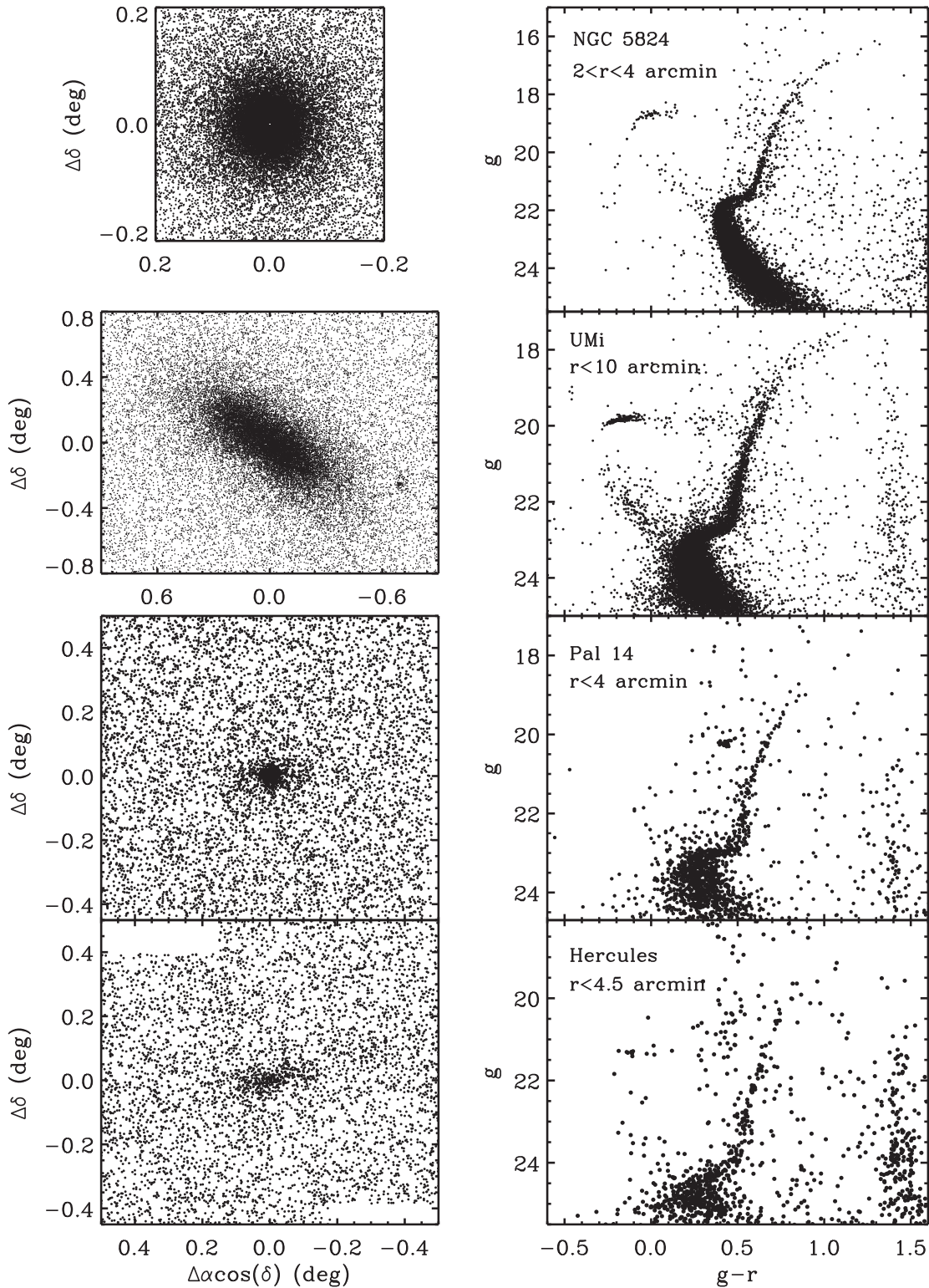


Figure 25. Same as Figure 17 but for NGC 5824, Ursa Minor, Palomar 14, and Hercules.

of ~ 6 Gyr and $[\text{Fe}/\text{H}] \sim -0.5$ dex, respectively (Carraro 2005; Valcheva et al. 2015).

In our photometry, the subgiant branch is clearly delineated, which allows us to confirm the system’s young age through isochrone fitting (i.e., ~ 6.5 Gyr; see Figure 17). This satellite is one of the faintest globular clusters known, with a total

luminosity of just $\sim 10^3 L_{\odot}$. Whiting 1 is surrounded by debris from the Sgr dSph, which complicates any analysis of its potential disturbed morphology (Paper I; Carballo-Bello et al. 2017). Our measurement of its effective radius, $r_{e,s} \simeq 6.4 \pm 0.6$ pc, makes it one of the smallest outer halo satellites.

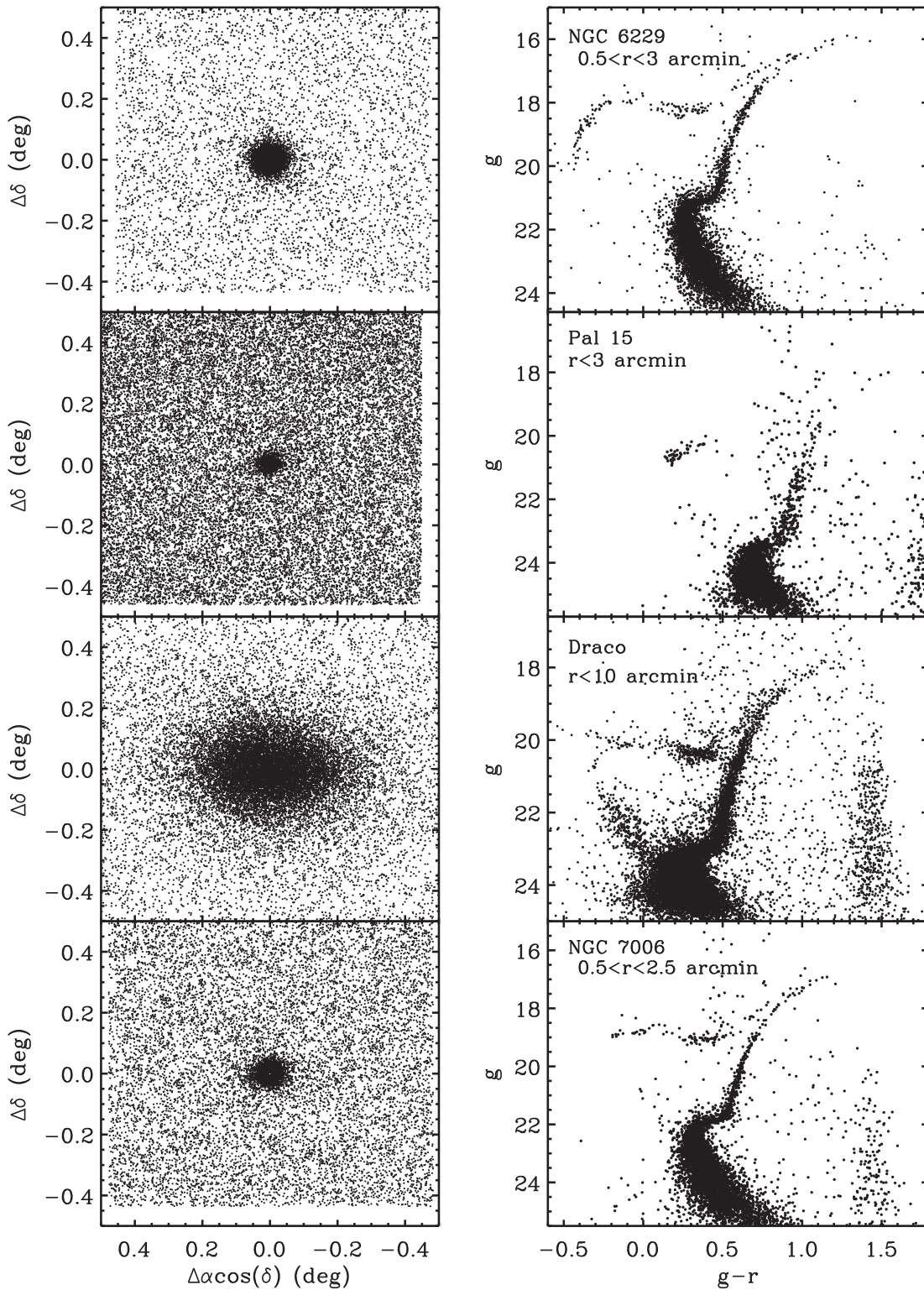


Figure 26. Same as Figure 17 but for NGC 6229, Palomar 15, Draco, and NGC 7006.

4.4.3. Segue 2

With a total luminosity of just $\sim 500 L_{\odot}$ and a central surface brightness of $\mu_{0,V} \sim 28.5$ mag arcsec $^{-2}$, Segue 2 is one of the faintest and most diffuse of the ultra-faint satellites discovered in the SDSS (Belokurov et al. 2009). It is usually considered to be a low-mass galaxy, primarily because of its large internal metallicity spread; i.e., spectroscopic measurements for member

stars range between $[\text{Fe}/\text{H}] \simeq -2.85$ and -1.33 dex (Kirby et al. 2013a).

Our data, reaching more than 3 mag below the MSTO, reveal a sparsely populated object with $r_{e,s} = 37 \pm 3$ pc and $M_V = -1.86 \pm 0.88$ (Figure 17). Because the subgiant branch is so poorly defined, it is difficult to measure the object’s age and distance accurately from isochrone fitting.

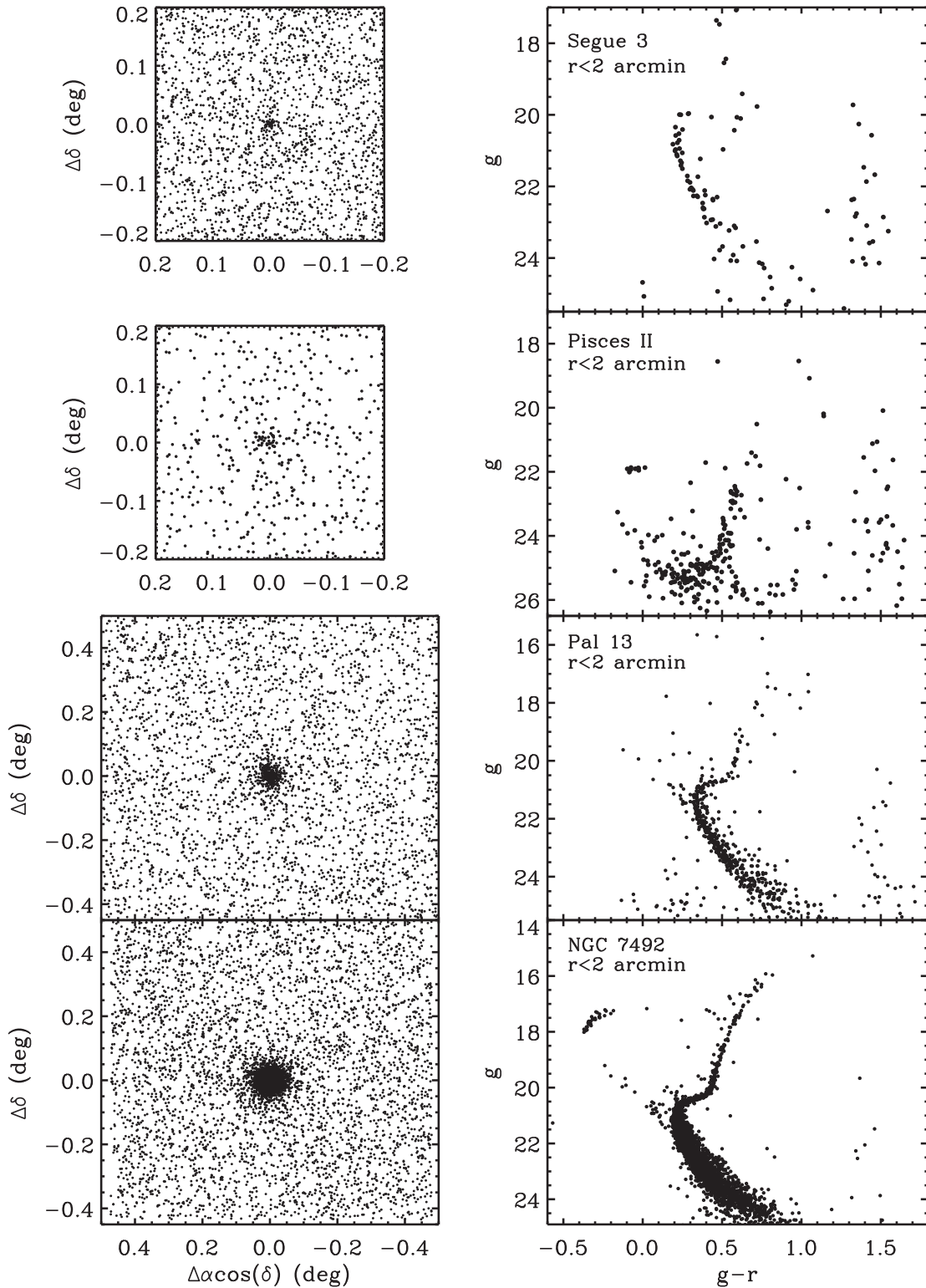


Figure 27. Same as Figure 17 but for Segue 3, Pisces II, Palomar 13, and NGC 7492.

Interestingly, Segue 2 does not appear to follow the familiar luminosity–metallicity relation obeyed by the Galaxy’s other dwarf satellites; i.e., its metallicity is on the high side for its (low) luminosity. This may indicate that Segue 2 was once a more luminous object, perhaps similar to Ursa Minor, that underwent significant tidal stripping (Kirby et al. 2013a). From our photometry, the isodensity contour

map (Figure 6) shows a highly irregular morphology suggestive of tidal stripping, although its number density profile does not show an excess of stars usually associated with the presence of tidal debris. We emphasize that the small number of member stars introduces significant shot noise, so conclusions on potential tidal interactions should be viewed with caution.

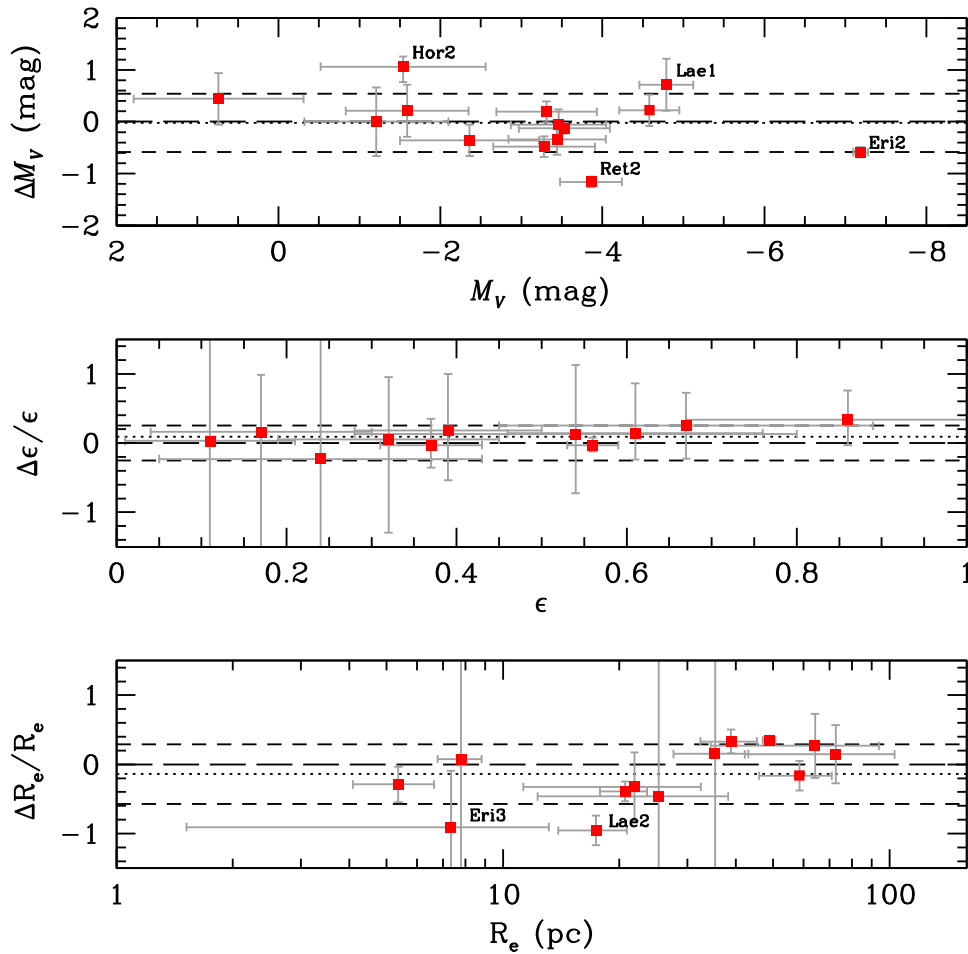


Figure 28. Comparison of photometric and structural parameters relative to the literature values for the 14 satellites in our secondary sample. From top to bottom, the panels show comparisons of absolute magnitude, ellipticity, and effective radius. In all cases, the plotted residuals are in the sense of our values minus those in the literature.

4.4.4. Fornax

The Fornax dSph galaxy was discovered by Shapley (1938b) using plates from the 24 inch telescope at Boyden Observatory. Baade & Hubble (1939) used plates from the 100 inch Mount Wilson telescope to establish many of its key photometric and morphological properties, reporting a major-axis diameter of $\sim 50'$, an ellipticity of $\epsilon \sim 0.3$, a distance of $R_h = 188$ kpc, and an absolute magnitude of $M = -11.9$.

Fornax has an apparent diameter that is among the largest of the outer halo satellites ($r_t \sim 1.2^\circ$; Battaglia et al. 2006). Our Clay imaging, which covers an area of $\sim 0.6 \text{ deg}^2$ in a 2×2 grid, does not reach the edge of the galaxy. For this reason, Fornax is the only object in our primary survey for which the maximum-likelihood method failed to converge. To estimate its structural parameters, we therefore resorted to the more traditional approach of fitting a density model to the binned number density profile. We find Fornax to be the largest and brightest object in our survey with $r_{e,s} = 787 \pm 9$ pc and $M_V = -13.46 \pm 0.14$. Its global ellipticity is measured to be $\epsilon = 0.28 \pm 0.01$.

Fornax contains multiple stellar populations (i.e., a dominant intermediate-age population, as well as both old and young stars; see, e.g., de Boer et al. 2012), and these different components are readily apparent in its complex CMD (Figure 17). It is also known that the spatial distributions of

these populations vary, with the younger population being more centrally concentrated and showing a clumpy morphology, while the older stars are more smoothly distributed. This complexity is evident in the isodensity map shown in Figure 6. Note that several of Fornax’s globular clusters are visible in the lower left panel of Figure 17.

4.4.5. AM 1

At a galactocentric distance of $R_{GC} \simeq 125$ kpc, AM 1 is one of the most remote Galactic globular clusters currently known. It was discovered by Lauberts (1976) while inspecting plates from the ESO Schmidt telescope in Chile. AM 1 is an intermediate-luminosity ($M_V = -5.2$) and metal-poor ($[\text{Fe}/\text{H}] = -1.7$ dex) cluster whose angular proximity to the Large Magellanic Cloud (LMC)—it is located just $\sim 15^\circ$ from the LMC center—prompted early speculation that it may be physically associated with the LMC. However, the latest distance estimates suggest an association is quite unlikely.

Figure 18 shows the CMD for the inner $2/5$ of AM 1. Like most outer halo clusters, AM 1 shows a clear second-parameter effect; i.e., it has a red HB despite its relatively low metallicity. This effect has been recognized since the 1970s, most notably by Harris (1976), Searle & Zinn (1978), and Zinn (1980a, 1980b), who pointed to an age spread among the outer halo clusters as a possible explanation for the unusual HB

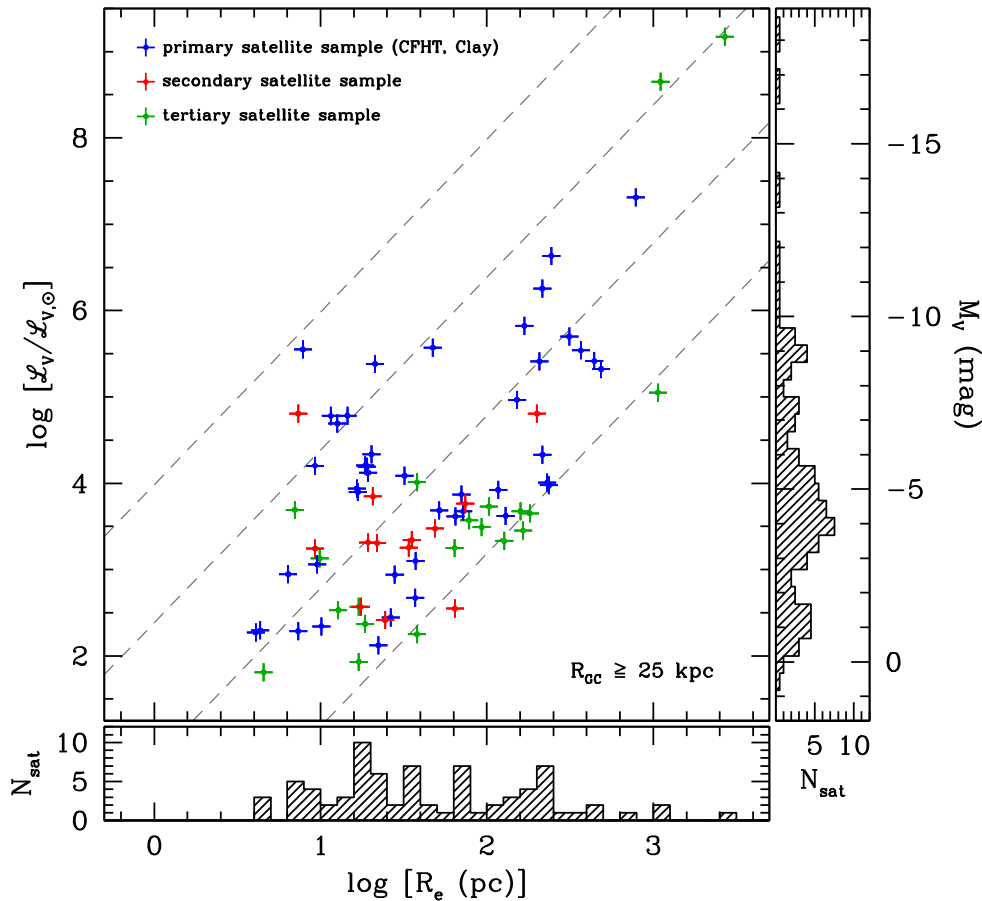


Figure 30. Same as Figure 29 but with labels and the four satellites with $R_{GC} \leq 25$ kpc removed. The histograms in the bottom and right panels show the distribution of these 77 outer halo satellites in terms of effective radius and absolute magnitude.

than the fainter, main-sequence stars. We see this effect as well, probably a consequence of a dust lane crossing the cluster in the N–S direction and causing differential reddening that affects the fainter stars more noticeably than the brighter giants.

Figure 18 shows the CMD based on our new CFHT imaging. Despite the heavy obscuration and differential reddening, the brighter evolutionary sequences are readily discernible, meaning that it is possible to identify candidate member stars and measure reliable structural parameters. Our effective radius, $r_{e,s} = 7.8 \pm 0.2$ pc, is larger than published values, while our absolute magnitude, $M_V = -9.07 \pm 0.07$,⁷ is significantly brighter than the value of Harris et al. (1997), indicating that Palomar 2 is one of the brightest outer halo clusters.

4.4.8. Carina

Carina was discovered by Cannon et al. (1977) while inspecting plates from the ESO/SRC Southern Sky Survey. Using CCD images taken with the CTIO 1 m telescope, Smecker-Hane et al. (1994) published wide-field photometry for Carina revealing a well-defined HB with two distinct components—direct evidence for two populations of differing age. From the color of the RGB, Smecker-Hane et al. (1994) obtained a mean metallicity of $[Fe/H] \sim -2.1$ dex. Deeper photometric studies, based on imaging from *HST*/WFPC2 and

the CTIO 4 m telescope, confirmed these findings (e.g., Mighell 1997; Hurley-Keller et al. 1998).

In our survey, Carina was observed in a 4×4 mosaic with the Clay telescope, covering a total area of $\simeq 2.2$ deg². This coverage extends well beyond the system’s nominal tidal radius (e.g., $R_t = 28.8$; Mateo 1998), and our CMD, which reaches to $g \sim 26$, reveals in detail the full complexity of Carina’s stellar populations (Figure 18). The combination of depth and field coverage makes our photometric catalog the most extensive currently available for this system. Indeed, Santana et al. (2016) recently used these data to derive a detailed star formation history for the galaxy. In our maximum-likelihood analysis, we measure an effective radius of $r_{e,s} = 313 \pm 3$ pc and an absolute magnitude of -9.43 ± 0.05 . Thus, Carina appears to be significantly larger than reported in some previous studies (although still consistent with early reports of likely member stars beyond the nominal tidal radius). Our number density profile does not show the previously reported “break” at $\sim 20'$ (Majewski et al. 2000, 2005; Muñoz et al. 2006b) and is well fitted over its full extent by a Sérsic profile with $n_s = 0.84 \pm 0.02$. The galaxy is moderately flattened, with $\epsilon = 0.37 \pm 0.01$, but its isodensity contour map shows no clear signs of tidal interaction (Figure 7).

4.4.9. NGC 2419

By far the brightest of the outer halo clusters, NGC 2419 is located in the direction of the Galactic anticenter. It was discovered by W. Herschel in 1788 and recognized as a globular cluster

⁷ The low uncertainty in our measurement does not include the effect of differential reddening, which is difficult to assess.

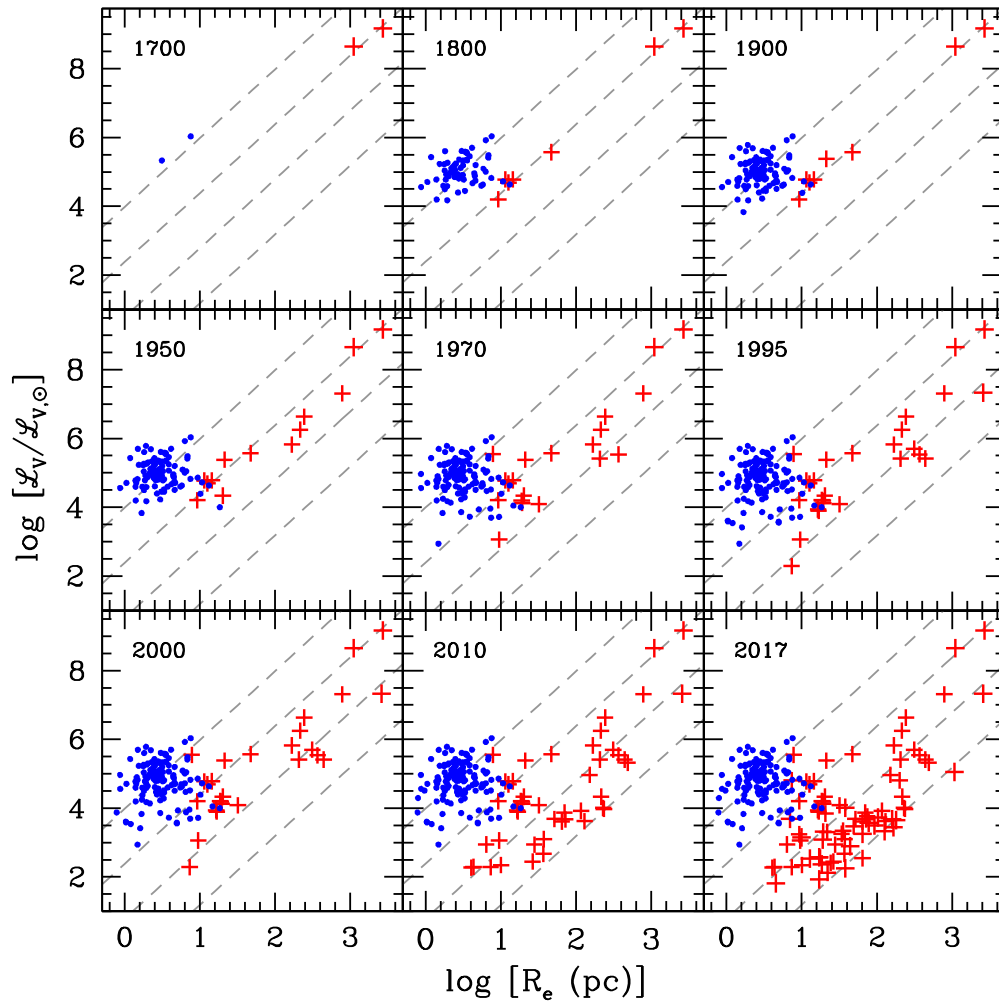


Figure 31. Discovery of Galactic satellites as a function of time, illustrating the importance of selection effects when identifying objects in the size–luminosity plane. The nine panels show the population of Galactic satellites known at the years labeled in each panel. A total of 139 globular clusters with $R_{GC} < 25$ kpc are shown as blue points. Red crosses show the 81 remaining satellites (i.e., globular clusters and galaxies) that are known at the present time, 77 of which reside in the outer halo, $R_{GC} \geq 25$ kpc.

almost a century and a half later by C. O. Lampland on plates from the Lowell Observatory (Baade 1935). Racine & Harris (1975) produced the first modern CMD for the cluster using *BI* plates taken with the Palomar 200 inch telescope. Their diagram reached $V \sim 22$, slightly more than 4 mag below the tip of the RGB, and revealed an extended and predominantly blue HB unlike most other remote halo clusters. From a comparison to M92, these authors concluded that NGC 2419 is equally metal-poor.

NGC 2419 is interesting because of its rather unusual nature: it is much brighter than the other remote halo cluster, and it does not show a second-parameter anomaly in its HB. It also appears to be unique in its chemical properties (Cohen et al. 2010; Cohen & Kirby 2012).

We imaged NGC 2419 with CFHT in a single pointing roughly centered on the cluster. Figure 19 shows our CMD for the cluster, which reaches 1 mag below the MSTO. A blue extended HB is clearly visible. We measure an absolute magnitude of $M_V = -9.35 \pm 0.03$. With an effective radius of $r_{e,s} \sim 25.7 \pm 0.2$ pc and King limiting radius of $r_{k,t} = 227$ pc, it is also the largest of the star clusters in our sample. Its isodensity map reveals a round and regular morphology, showing no obvious signs of tidal interaction with the Milky Way (Figure 8). We measure an ellipticity of $\epsilon_s = 0.05 \pm 0.01$.

4.4.10. Koposov 1 and 2

Koposov 1 and 2 were initially identified by Koposov et al. (2008) using SDSS data and subsequently confirmed as Galactic satellites by the same group using imaging from Calar Alto. Both systems were originally classified as globular clusters but later reported to be old open clusters by Paust et al. (2014). These authors found both satellites to be significantly younger than other outer halo clusters. They also proposed that both Koposov 1 and 2 were originally born as part of the Sagittarius dSph and later removed by the Galactic tidal field.

From our Clay imaging, we determined a very faint absolute magnitude of $M_V = -1.0 \pm 0.7$ for Koposov 1 (slightly brighter than the value of Paust et al. 2014) and an effective radius of $r_e = 10.1 \pm 2.5$ pc, similar to earlier measurements. As is the case with Koposov 2 and Muñoz 1, the measured ellipticity is high ($\epsilon = 0.55 \pm 0.15$) but poorly constrained due to the small number of member stars. Indeed, the CMD of Koposov 1 is sparsely populated, with no stars visible on the RGB and only a handful of potential subgiant stars (Figure 22). If these are bona fide Koposov 1 members, then isochrone fitting points to an age between 8 and 10 Gyr, consistent with the conclusions of Paust et al. (2014).

Koposov 2 has a nearly identical low luminosity as Koposov 1. We measure an absolute magnitude of $M_V = -0.9 \pm 0.8$ and an effective radius of $r_{e,s} = 4.3 \pm 0.9$ pc. Its CMD has no stars on the upper RGB, and the upper main sequence is scarcely populated as well (Figure 19). Despite the depth of our photometry, which reaches to $g = 25$, the number of detected stars remains low, translating into rather large uncertainties in the measured structural parameters, particularly in the case of the King core and tidal radii, where the uncertainties reach 65%. Its measured ellipticity is among the highest obtained for a globular cluster, at $\epsilon = 0.48 \pm 0.15$, but given the low number of stars, this may be an artifact of shot noise.

4.4.11. Ursa Major II

Ursa Major II was one of the first ultra-faint dwarfs discovered in the SDSS (Zucker et al. 2006b). Follow-up images from the Subaru telescope acquired by the same authors revealed a stellar system with a highly elongated morphology, a size of ~ 250 pc \times 125 pc, and an absolute magnitude of $M_V \sim -3.8$. Its unusual morphology prompted Fellhauer et al. (2007) to suggest that Ursa Major II may be the disrupted progenitor of the Orphan Stream (Belokurov et al. 2006b).

Using the same CFHT images described here, Muñoz et al. (2010) carried out a morphological analysis and argued that UMa II is probably a system that is undergoing severe tidal disruption. This view is supported by the observed number density profile and isodensity contour map (Figure 8). The former is poorly fitted by each of the density laws considered in this study, and the latter shows an unusually elongated structure. If this interpretation is correct, then previous reports of high mass-to-light ratios (which were obtained under the assumption of dynamical equilibrium) should be viewed with caution. Kinematic measurements covering the full extent of UMa II will be needed to conclusively determine its dynamical state.

Our CMD for Ursa Major II reaches 3 mag below the well-defined MSTO (Figure 19). The subgiant branch is clearly visible, although the RGB is only sparsely populated. Using our maximum-likelihood method, we revisit this system's structural parameters and measure an absolute magnitude of $M_V = -4.2 \pm 0.3$ and an effective radius of $r_{e,s} = 130 \pm 4$ pc. We find its mean ellipticity to be $\epsilon = 0.56 \pm 0.03$, although, as noted by Muñoz et al. (2010), this value increases inward.

4.4.12. Pyxis

Located at a galactocentric distance of $R_{GC} \simeq 41$ kpc, Pyxis was detected by Weinberger (1995) as a stellar overdensity and quickly confirmed as a globular cluster by da Costa (1995) and Irwin et al. (1995).

Pyxis is the cluster in our sample with the lowest Galactic latitude, ($l = 26^\circ, b = 7^\circ$), and its CMD (Figure 19) is significantly contaminated by foreground disk stars. Nevertheless, the cluster sequences are readily apparent and, unlike Palomar 2, are only somewhat broadened. In line with most outer halo clusters, Pyxis has a predominantly red HB and thus exhibits the well-known second-parameter effect. In this context, Dotter et al. (2011) used *HST*/ACS data to measure an age of 11.5 ± 1.0 Gyr, consistent with Pyxis being somewhat younger than the inner halo systems.

Our analysis suggests an effective radius of $r_{e,s} = 18.6 \pm 0.5$ pc, which is typical for outer halo clusters, and an

absolute magnitude of $M_V = -5.7 \pm 0.2$, also consistent with published values. Its number density profile is well fitted by either a King or Sérsic model, and its 2D morphology is round and regular, with a low ellipticity of $\epsilon = 0.04 \pm 0.02$.

4.4.13. Leo T

At a galactocentric distance of $R_{GC} = 420$ kpc, or roughly half the distance to M31, Leo T is easily the most distant satellite in our survey. It was discovered by Irwin et al. (2007) as a stellar overdensity in the SDSS DR5 data. Because of its large distance, the original SDSS CMD reached only a few mag below the tip of the RGB but was sufficient to reveal two key features: a well-defined RGB and a bluer sequence likely due to the presence of young stars ($\lesssim 1$ Gyr). Irwin et al. (2007) also detected H I associated with Leo T, classifying this object as a transition-type dwarf galaxy. Based on deep Large Binocular Telescope data, de Jong et al. (2008) found that Leo T has been forming stars at least as recently as a few hundred Myr ago, making Leo T the faintest star-forming galaxy known at this time.

In our Clay imaging, we detect stars in Leo T's CMD only down to the red clump level (Figure 20). We find an absolute magnitude of $M_V = -7.6 \pm 1.0$ and an effective radius of $r_{e,s} = 151 \pm 17$ pc, both similar to published values. In terms of morphology, Leo T is one of the roundest galaxies in our sample, with $\epsilon = 0.23 \pm 0.09$. Its number density profile is well fitted by either a King or Sérsic model, and its morphology appears undisturbed (Figure 9).

4.4.14. Palomar 3

Palomar 3 was discovered by Wilson (1955) and Abell (1955) using plates from the National Geographic Society–Palomar Observatory Sky Survey. At $R_{GC} \simeq 92.5$ kpc, it is, with AM 1, Eridanus, NGC 2419, Palomar 4, and Palomar 14, among the most remote Galactic globular clusters. The CMD based on our CFHT imaging (see Figure 20) reveals a definite second-parameter effect, with an HB that is composed almost exclusively of red stars despite its low metallicity of $[Fe/H] \simeq -1.6$ dex (Koch et al. 2009a).

Our analysis reveals Palomar 3 to be a relatively faint ($M_V = -5.5 \pm 0.2$) and extended ($r_{e,s} = 19.4 \pm 0.5$ pc) cluster, similar in size to the smallest of the ultra-faint dwarf galaxies, Willman 1 and Segue 1. However, unlike these objects, the cluster's two-dimensional morphology (see Figure 9) is unremarkable, with an ellipticity of $\epsilon = 0.07 \pm 0.03$, and shows the regular density contours typical of globular clusters.

4.4.15. Segue 1

Among the Galactic satellites discovered during the last decade, Segue 1 (Belokurov et al. 2007) is arguably one of the most fascinating objects. With an absolute magnitude of $M_V = -1.3 \pm 0.7$, it has been described as the faintest Milky Way satellite galaxy discovered to date (Geha et al. 2009; Simon et al. 2011), although it was originally classified as a diffuse globular cluster by Belokurov et al. (2007). The CMD based on our CFHT imaging (Figure 20) traces the main sequence roughly 4 mag below the MSTO, and yet only a handful of subgiant stars are visible, highlighting the very low luminosity of the object ($\simeq 280 L_\odot$).

Its low luminosity, modest ellipticity ($\epsilon = 0.31 \pm 0.13$), and compact size ($r_{e,s} = 26 \pm 4$ pc) have prompted some

researchers to suggest that Segue 1 may be a dark matter–free, disrupted cluster (Domínguez et al. 2016). Based on our imaging, we see no signs that Segue 1 is being affected by tides. Its density contour map (see Figure 9) shows a round central structure, and the system’s kinematic and chemical properties clearly favor a dwarf galaxy classification.

4.4.16. *Leo I*

At a galactocentric distance of $R_{GC} = 258$ kpc, Leo I is one of the most distant stellar systems that is likely bound to the Milky Way. It was discovered, together with Leo II, by Harrington & Wilson (1950) while inspecting plates from the Palomar Sky Survey. Hodge (1963) carried out a star-count analysis using a variety of plate material and found Leo I to be elliptical ($\epsilon \sim 0.3$) and almost perfectly symmetrical in structure. Assuming a distance similar to that of Leo II, Hodge (1963) estimated a linear cutoff radius along the major axis of 950 ± 70 pc. He also reported an absolute magnitude of $M_V \simeq -11.4$ for his adopted distance of 230 kpc.

Gallart et al. (1999a, 1999b) presented what is, to date, the deepest photometric analysis of Leo I. Their *HST*/WFPC2 *VI* imaging for a central field reached more than 2 mag deeper than the study of Lee et al. (1993), barely detecting the old MSTO. Gallart et al. (1999a) used these data to measure a detailed star formation history based on comparison with synthetic CMDs. They concluded that Leo I is dominated by an intermediate-age population, with the majority of the stars having formed between 7 and 1 Gyr ago, at which point star formation abruptly ceased.

Our CFHT photometry is visibly affected by the presence of Regulus, as can be seen in Figure 20. Our CMD reaches $g \sim 25$, albeit with strongly varying completeness across the field. Nevertheless, we are able to estimate useful structural parameters, finding $M_V = -11.8 \pm 0.3$, $r_{e,s} = 244 \pm 2$ pc, and $\epsilon = 0.30 \pm 0.01$. The morphology of Leo I appears to be fairly regular, with no sign of obvious tidal features (Figure 9).

4.4.17. *Sextans*

Sextans is one of the faintest and most diffuse of the Galaxy’s classical dSph galaxies. Due to its low surface brightness and the significant foreground contamination arising from its low Galactic latitude ($b \simeq 8^\circ$), it escaped detection until Irwin et al. (1990) discovered it in an analysis of plates taken with the 1.2 m UK Schmidt telescope. From the mean magnitude of the HB, the authors estimated a distance of 85 ± 5 kpc. Fitting a King (1962) model to the surface density profile yielded a King limiting radius of ~ 2 kpc and an absolute magnitude of $M_B \sim -8$.

Several deep CCD photometric surveys covering a large fraction of the galaxy have now been published. Lee et al. (2003) used the CFH12K camera at CFHT to produce a CMD that reaches $V \sim 24$, about 1 mag below the MSTO. The CMD was found to be consistent with a mean metallicity of $[\text{Fe}/\text{H}] = -2.1 \pm 0.1$ dex. Okamoto et al. (2008a) used Subaru imaging to produce a CMD that reached to $V \sim 25$, the deepest to date. Their analysis showed that the red HB stars seem to be more concentrated than the blue HB stars, consistent with the metallicity gradient reported by Battaglia et al. (2011).

In our survey, Sextans was imaged in four CFHT pointings arranged in a 2×2 grid that covers an area of nearly 4 deg^2 .

Our photometry reaches to a depth of $g \sim 25.5$, a little more than 2 mag below the MSTO. This makes our survey the most extensive to date in terms of depth and spatial coverage. Our CMD shows a narrow RGB, as well as an extended but predominantly red HB (Figure 21). A blue straggler sequence is also readily apparent. We measure an effective radius of $r_{e,s} \sim 442 \pm 4$ pc, making Sextans one of the largest satellites included in this catalog. We also find an absolute magnitude of $M_V = -8.7 \pm 0.06$, in good agreement with previous measurements (but see Section 4.2). The isodensity contour map in Figure 10 shows a fairly regular morphology with no obvious signs of tidal features.

4.4.18. *Ursa Major I*

Ursa Major I was one of the first ultra-faint dwarfs to be discovered in automated searches for substructures in the SDSS (Willman et al. 2005b). Located at a galactocentric distance of $R_{GC} \simeq 102$ kpc, early estimates of its photometric properties ($M_V \sim -6.75$, $r_h = 250$ pc; Willman et al. 2005b) were consistent with a dwarf galaxy classification, and its CMD appeared to be similar to that of Sextans, albeit with more sparsely populated evolutionary sequences.

Okamoto et al. (2008b) obtained deep Suprime-Cam imaging with the Subaru telescope, revising Ursa Major I’s distance and showing it to be dominated by an old, metal-poor population more closely resembling that of a globular cluster than a typical dSph. Brown et al. (2012, 2014) included Ursa Major I in their *HST*/ACS survey of ultra-faint dwarfs. From their *VI* photometry, which reached 4 mag below the MSTO, they concluded that Ursa Major I appears to be a “fossil” galaxy, in the sense that it hosts an ancient and metal-poor population with all star formation having ceased ~ 11.6 Gyr ago. In terms of its morphology, Okamoto et al. (2008b) found Ursa Major I to be both elongated and disturbed and suggested that it has suffered (or continues to suffer) significant tidal stripping.

Although we covered this satellite with two CFHT pointings, the SW field was unfortunately taken in conditions of poor seeing, resulting in a significantly shallower photometry. We therefore restricted our analysis to just the deeper NE field (see Figure 21). Like its neighbor Ursa Major II, we find Ursa Major I to be highly elongated, with an overall ellipticity of $\epsilon = 0.57 \pm 0.03$ and irregular isodensity contours resembling those of Ursa Major II (Figure 10). We measure an absolute magnitude of $M_V = -5.1 \pm 0.4$ and an effective radius of $r_{e,s} = 235 \pm 10$ pc.

4.4.19. *Willman 1*

The first of the ultra-faint stellar systems discovered in the SDSS (Willman et al. 2005a), Willman 1 is also, given its complex photometric and kinematical properties, one of the more intriguing Galactic satellites (e.g., Willman et al. 2011). It occupies a region in the luminosity–size diagram ($M_V = -2.5 \pm 0.7$, $r_{e,s} = 28 \pm 2$ pc) that includes Segue 1, Segue 2, and Boötes II, all of which have been classified as ultra-faint dwarf galaxies. Its size, however, is more comparable to that of a remote halo cluster. It should be noted that all clusters having a similar size are brighter than Willman 1 by an order of magnitude or more.

Our CFHT photometry, which reaches to $g \simeq 25$, reveals an irregular morphology that hints at tidal interactions. In

particular, the isodensity map seems to have an unusual three-tailed structure, as noted by Willman et al. (2006; see Figure 10). Unfortunately, the sparsely populated CMD renders this finding tentative.

4.4.20. Leo II

The Leo II satellite was discovered, along with Leo I, by Harrington & Wilson (1950) while examining plates taken with the 48 inch Palomar Schmidt telescope for the National Geographic Society–Palomar Observatory Sky Survey. Hodge (1962, 1971) carried out a star-count analysis of the galaxy using plates from multiple telescopes, finding a (low) ellipticity of $\epsilon = 0.01 \pm 0.10$ and a limiting radius of $r_r = 11'9$, corresponding to $\simeq 800$ pc at a distance of 230 kpc.

Mighell & Rich (1996) presented deep *HST*/WFPC2 photometry for Leo II reaching $V \sim 27.4$ and $I \sim 26.6$. Their CMD, reaching about 3 mag below the MSTO, suggested a mean metallicity of $[\text{Fe}/\text{H}] = -1.60 \pm 0.25$ dex and an age of 9 ± 1 Gyr. More recently, Coleman et al. (2007) used SDSS to explore the outer structure of the galaxy, concluding that the influence of the Galactic gravitational field on the structure of the galaxy has been relatively mild.

In our survey, we imaged Leo II in a 2×2 grid pattern with the Clay telescope, covering an area of ~ 0.6 deg². Our CMD reaches $g \sim 25.5$, covering about 3 mag below the HB (Figure 21). We measure an absolute magnitude of $M_V = -9.7 \pm 0.04$ and an effective radius of $r_{e,s} = 168 \pm 2$ pc, consistent with previous estimates. Leo II is the roundest of the dwarf satellites in our survey with an overall ellipticity of $\epsilon = 0.07 \pm 0.02$, similar to many of the globular clusters in our sample. Its morphology is found to be quite regular, with no signs of tidal features (Figure 10).

4.4.21. Palomar 4

The second most distant of the Galactic globular clusters ($R_{GC} = 110$ kpc), Palomar 4 was discovered by Abell (1955) on plates from the National Geographic Society–Palomar Observatory Sky Survey. Stetson et al. (1999) used *HST*/WFPC2 data to show that Palomar 4 is a second-parameter cluster, with an age 1.5–2 Gyr younger than M3 and M5.

Our CFHT imaging reaches ~ 1.5 mag below the MSTO, as shown in Figure 22. A red HB is clearly visible despite the cluster’s relatively low metallicity (e.g., $[\text{Fe}/\text{H}] \simeq -1.4$ dex; Koch & Côté 2010). From our data, we find an absolute magnitude of $M_V = -6.0 \pm 0.2$ and an effective radius of $r_{e,s} = 20 \pm 0.6$ pc, values that are in line with those of its outer halo counterparts, Palomar 3, AM 1, and Eridanus. Isochrone fitting suggests an age a few Gyr younger than inner halo clusters (Stetson et al. 1999). Its surface density profile shows a possible excess of stars at large radii with respect to the fitted King, or even Sérsic, model, although its two-dimensional morphology appears round and regular (Figure 11). We see no evidence for a tidal tail in the Galactic anticenter direction, as reported by Sohn et al. (2003).

4.4.22. Leo IV and V

This pair of low-luminosity satellites was discovered in SDSS DR5 and DR6, respectively, by Belokurov et al. (2007, 2008). The two systems are located at large and rather similar heliocentric distances: $R_\odot \simeq 160$ (Leo IV) and 180 kpc (Leo V). In the discovery papers, Leo IV was found to be the larger and brighter

of the two systems, with $r_h \sim 160$ pc and $M_V = -5.1 \pm 0.6$, compared to $r_h \sim 40$ pc and $M_V = -4.3 \pm 0.5$ for Leo V. The two systems are separated by just $\sim 3^\circ$ on the sky and are receding with similar heliocentric radial velocities: $v_r = 132$ and 173 km s⁻¹, respectively (Simon & Geha 2007; Belokurov et al. 2008). Taken together, these properties might suggest a physical connection.

De Jong et al. (2010) used imaging from the 3.5 m Calar Alto telescope to analyze the distribution of RGB and HB stars and found both galaxies to be larger than initially reported, with $r_h = 206 \pm 36$ and 133 ± 31 pc for Leo IV and Leo V, respectively. Both galaxies were found to be highly elongated ($\epsilon > 0.5$). Later imaging studies of Leo IV (Sand et al. 2010; Okamoto et al. 2012) reexamined its structural properties, reporting values more similar to the initial estimates than to those of de Jong et al. (2010). Brown et al. (2014) presented *HST*/ACS photometry for Leo IV and argued that the system is composed exclusively of old, metal-poor stars; i.e., the system formed more than 80% of its stars by $z = 6$. Leo IV is thus another example of a fossil galaxy in the Galactic halo.

In Figure 22, we show CMDs for these systems based on our Clay imaging. Our photometry reaches just slightly below the MSTO in each galaxy. Although this is similar in depth to the photometric study of de Jong et al. (2010), our measured structural parameters are significantly smaller for both objects. We find $r_{e,s} = 117 \pm 14$ and 52 ± 11 pc and $M_V = -5.0 \pm 0.3$ and -4.4 ± 0.4 , respectively, for Leo IV and V. We are unsure of the reason for this discrepancy but note that our results are similar to most previously published values using both shallower and deeper photometry (Belokurov et al. 2008; Martin et al. 2008b; Sand et al. 2009; Okamoto et al. 2012).

4.4.23. Coma Berenices

The discovery of Coma Berenices and four other faint Galactic satellites was reported by Belokurov et al. (2007). The discovery itself was based on SDSS DR5 imaging but included deeper follow-up observations from the Suprime-Cam on the Subaru telescope. These deeper data were used to examine Coma Berenices’s stellar content and derive structural parameters. On the basis of their estimated half-light radius, $r_h \sim 70$ pc, these authors classified the object as an ultra-faint dwarf galaxy.

Coma Berenices was previously studied, along with Ursa Major II, by Muñoz et al. (2010) using the same CFHT imaging included in this study. The CMD shown in Figure 23 reaches almost 4 mag below the MSTO and shows a well-defined subgiant branch, as well as a hint of an RGB. Muñoz et al. (2010) confirmed that Coma Berenices is a faint, compact dwarf galaxy of modest luminosity. We find an absolute magnitude of $M_V = -4.4 \pm 0.3$ and an effective radius of $r_{e,s} = 72 \pm 4$ pc. Its number density profile is well described by any of the density models explored in our analysis, including King and Sérsic laws (Figure 12). Unlike what was seen in the Subaru data, our isodensity map reveals a regular morphology with an overall elongation of $\epsilon = 0.37 \pm 0.05$, similar to most dSph galaxies, with no signs of tidal stripping.

4.4.24. Canes Venatici II

One of five ultra-faint satellites discovered by Belokurov et al. (2007) using SDSS DR5 data, Canes Venatici II is a faint,

compact system located $R_{GC} \sim 161$ kpc from the Galactic center.

To date, the deepest photometry published for Canes Venatici II is the Subaru VI data of Okamoto et al. (2012). In their CMD, a sparsely populated RGB was visible, as well as a few blue HB star candidates. Our gr CMD looks nearly identical to the earlier CMD from Okamoto (Figure 23). Although our photometry is slightly shallower, we cover an area that is four times larger. Based on our CFHT photometry, we measure an effective radius of $r_{e,s} = 70 \pm 11$ pc, slightly smaller than the Okamoto et al. (2012) value, and an absolute magnitude of $M_V = -4.9 \pm 0.4$. We find an overall ellipticity $\epsilon = 0.46 \pm 0.11$, significantly larger than the value of $\epsilon = 0.23$ reported by Okamoto et al. (2012). The two-dimensional morphology of Canes Venatici II shows no obvious irregularities or perturbations (Figure 12), although the number of stars at large radii is low.

4.4.25. Canes Venatici I

Canes Venatici I was discovered by Zucker et al. (2006a) using SDSS DR5 data. At a galactocentric distance of $R_{GC} \sim 220$ kpc, it is one of the most remote Galactic dwarf satellites. The original estimate of its absolute magnitude, $M_V \sim -7.9$, placed Canes Venatici I at the edge of the region of the size–luminosity diagram occupied by classical dSph galaxies. Martin et al. (2008a) acquired deep BV imaging reaching the level of the MSTO with the Large Binocular Telescope. They found a complex star formation history with at least two populations: a spatially extended, old (>10 Gyr), and metal-poor population that dominates (95%) the stellar mass and a younger (~ 1.4 – 2.0 Gyr), more metal-rich, and more spatially concentrated population.

More recently, Okamoto et al. (2012) published the deepest CMD to date, reaching $V \sim 26$, using imaging collected with the Suprime-Cam on the Subaru telescope. These authors measured a distance of 216 ± 8 kpc from isochrone fitting and noted that the system’s HB morphology and RGB look remarkably similar to those of Draco.

Our CFHT images are nearly as deep as those of Okamoto (see Figure 23) but cover a roughly fourfold larger area. We measure an effective radius of $r_{e,s} = 486 \pm 14$ pc and an absolute magnitude of $M_V = -8.5 \pm 0.1$. Our isodensity map reveals a morphology that is quite elongated in the E–W direction, with an overall ellipticity of $\epsilon = 0.46 \pm 0.2$. The contours look fairly regular with a possible twist in the outer regions but at a low statistical significance (Figure 12).

4.4.26. AM 4

AM 4 was discovered by Madore & Arp (1982) as a sparse stellar overdensity in the ESO/SRC Southern Sky Survey. The first CMD for the object was produced by Inman & Carney (1987) using data from the 1.5 m telescope at CTIO. Their CMD showed AM 4 to be an extremely low-luminosity system with a striking lack of evolved stars. Prior to the discovery of the ultra-faint satellites in the SDSS, AM 4 was by far the faintest globular cluster known in the Galaxy. Carraro (2009) obtained new imaging for AM 4 using the 1 m telescope at Las Campanas Observatory and estimated an age of ~ 9 Gyr. This is similar to the globular cluster Terzan 7, which is known to be associated with the Sagittarius dwarf galaxy. Due to its extremely low luminosity and relatively young age, Carraro

(2009) postulated that AM 4 may also be associated with Sagittarius, although its current location in the Galaxy appears inconsistent with that of other Sagittarius debris.

From our Clay imaging, we calculate an absolute magnitude of $M_V = -0.9 \pm 0.8$ and an effective radius of $r_{e,s} = 7.3 \pm 1.4$ pc. Its extreme luminosity and fairly compact size are comparable to those of Koposov 1 and 2, Muñoz 1, and Segue 3, all of which have effective radii smaller than 10 pc. As with these ultra-faint counterparts, AM 4 shows a decided lack of stars in the RGB region, which prevents us from estimating its metallicity photometrically (see Figure 23). However, the SGB region is well defined, and from isochrone fitting, we conclude that AM 4 is indeed an ancient (>12 Gyr) stellar system.

4.4.27. Boötes II

Discovered in SDSS DR5 imaging by Walsh et al. (2007), Boötes II lies just $1^\circ.7$ from the Boötes I satellite (discovered 1 yr earlier). Unlike the case of Leo IV and V, the two systems do not appear to form a physical pair. Boötes II is located closer to the Galactic center than Boötes I, with a distance difference comparable to that of the Leo IV and V pair ($R_{GC} \simeq 42$ and 60 kpc, respectively; Walsh et al. 2008). However, Boötes II is moving with a mean heliocentric radial velocity that differs by nearly 200 km s^{-1} from that of Boötes I, and in the opposite direction (Koch et al. 2009b). A physical association between the two satellites thus seems unlikely.

From our CFHT data, we measure an absolute magnitude of $M_V = -2.9 \pm 0.7$ and an effective radius of $r_{e,s} = 37 \pm 6$ pc. These values are slightly smaller than previous estimates (Walsh et al. 2008; Koch et al. 2009b) and make Boötes II one of the smallest and faintest of the ultra-faint satellites. Our imaging, which reaches ~ 3 mag below the MSTO, shows the CMD (Figure 24) to be sparsely populated, with only a handful of RGB star candidates. Despite its relatively low overall ellipticity, $\epsilon = 0.24 \pm 0.12$, Boötes II is one of the most distorted of the ultra-faint systems. Its two-dimensional morphology shows an irregular structure (Figure 13) with multiple tidal features that resemble those of Willman 1, a system that is similar in size and luminosity and located at a comparable galactocentric distance of $R_{GC} \sim 40$ kpc.

It has been suggested in the past that Boötes II may be associated with the Sagittarius dwarf galaxy (Koch et al. 2009b). Our CFHT photometry shows that a second main sequence is clearly present in this field well beyond the extent of the dwarf and likely associated with Sagittarius (Law & Majewski 2010). From isochrone fitting, we find the population responsible for this second sequence to be located at a heliocentric distance of ~ 55 kpc. Boötes II itself is located in the foreground, at a distance of ~ 42 kpc.

4.4.28. Boötes I

The Boötes I dwarf galaxy was one of the first ultra-faint satellites to be discovered in SDSS (Belokurov et al. 2006a). The discovery article placed it at a galactocentric distance of $R_{GC} \sim 60$ kpc and estimated the half-light radius to be $r_h \sim 220$ pc, similar in size to classical dSph galaxies. Muñoz et al. (2006a) used the WIYN telescope to carry out the first spectroscopic study of this system and found its velocity dispersion of $6.6 \pm 2.3 \text{ km s}^{-1}$ to translate into a mass-to-light ratio between 130 and 610 in solar units. They also reported a

mean metallicity of $[\text{Fe}/\text{H}] \sim -2.5$ dex, making Boötes I the darkest and least chemically evolved dwarf galaxy known at that time.

Our CFHT imaging (covering a $2^\circ \times 1^\circ$ region) reaches ~ 2.5 mag below the MSTO. The subgiant branch and lower RGB are clearly defined, and a blue HB is discernible, although it is sparsely populated. A clear blue straggler sequence is also visible (Figure 24). We measure an absolute magnitude of $M_V = -6.0 \pm 0.2$, an effective radius of $r_{e,s} = 216 \pm 5$ pc, and an overall ellipticity of $\epsilon = 0.25 \pm 0.02$, consistent with previous estimates. Quite recently, Roderick et al. (2016) presented a deep-imaging survey carried out with the DECam imager on the CTIO 4 m telescope. They found a large, extended stellar substructure surrounding the galaxy and argued that this system may have undergone significant tidal disruption. Our isodensity contour map (Figure 13) shows an outer structure that is consistent with the findings of Roderick et al. (2016).

4.4.29. NGC 5694

Located at a galactocentric radius of $R_{\text{GC}} \simeq 29$ kpc, NGC 5694 was discovered in 1784 by Herschel. It was first resolved into stars and confirmed to be a globular cluster by Lampland & Tombaugh (1976) using plates taken with the 13 inch Lawrence-Lowell telescope at Lowell Observatory. An unusual feature of NGC 5694 is its large spatial extent. Correnti et al. (2011) reported the discovery of a low surface brightness halo surrounding the cluster. They were able to trace this feature out to a distance of at least $\sim 9'$ ($20r_c$). This is well beyond the King limiting radius of $4'/28$ estimated by Trager et al. (1995). In the same vein, Bellazzini et al. (2015) measured the velocity dispersion profile of NGC 5694 and found it to decrease and then flatten out to a distance of $14r_h$. They argued that NGC 5694 is a cluster that has yet to fill its Roche lobe, remaining tidally undisturbed after evolving in isolation. They also noted that this seems to be the case for a number of outer halo clusters, including Eridanus, Palomar 2, NGC 5824, Palomar 4, NGC 6229, NGC 7006, and NGC 7492.

From our CFHT data, we measure an effective radius of $r_{e,s} = 4.3 \pm 0.1$ pc and an absolute magnitude of $M_V = -7.9 \pm 0.1$. In agreement with Correnti et al. (2011), we detect a main-sequence population out to at least $9'$ ($\simeq 90$ pc). The cluster is fairly round and regular in structure, with $\epsilon = 0.06 \pm 0.02$, and its CMD shows an extended blue HB (Figure 24). At a galactocentric distance of $R_{\text{GC}} = 29$ kpc, it is located close to NGC 5824, an outer halo cluster that is similar in size, luminosity, and HB morphology. Overall, NGC 5694 differs markedly from most of the halo clusters beyond $R_{\text{GC}} \sim 80$ kpc in being brighter, more concentrated, and with a blue HB.

4.4.30. Muñoz 1

Muñoz 1 is the lone object in our survey to be discovered from our own imaging (Muñoz et al. 2012a). Identified on the CFHT images acquired for the Ursa Minor dSph galaxy, which were arranged in a 4×4 grid, Muñoz 1 was detected as a stellar overdensity located $\sim 45'$ to the SW of the Ursa Minor photocenter (and inside the latter's tidal radius). Indeed, Muñoz 1 is visible in the isodensity contour map for Ursa Minor as the round, compact feature in Figure 14. Spectra taken with Keck/DEIMOS yielded a systemic radial velocity

of $v_r = -137 \pm 4$ km s^{-1} , which is lower than that of Ursa Minor by more than 100 km s^{-1} . This fact, along with a line-of-sight distance difference of ~ 30 kpc (in the sense that Muñoz 1 is the closer of the two systems), rules out any physical association.

Our CMD shows a clear MSTO, although the system is so faint that almost no stars are visible in either the subgiant or RGB regions (Figure 24). We measure an effective radius of $r_{e,s} = 22 \pm 5$ pc and an absolute magnitude of $M_V = -0.5 \pm 0.9$, making Muñoz 1 one of the faintest of the known Galactic satellites.

4.4.31. NGC 5824

At a galactocentric distance of $R_{\text{GC}} = 26$ kpc and with an absolute magnitude (from this work) of $M_V = -9.3 \pm 0.04$, NGC 5824 is the second brightest of the outer halo clusters (after NGC 2419). It was discovered in the 19th century but not studied in detail for roughly a century.

From our data, we measure an effective radius of $r_{e,s} = 4.9 \pm 0.1$ pc and a fairly round shape, $\epsilon = 0.03 \pm 0.01$, with no obvious signs of morphological perturbation. Our CMD reaches more than 3 mag below the MSTO (Figure 25) and clearly shows an extended blue HB. This is similar to NGC 5694 but unlike other extended clusters at $R_{\text{GC}} \sim 100$ kpc. Our photometry is consistent with an old age (>12 Gyr), as was previously noted by Sanna et al. (2014) from *HST*/WFPC2 data. As is the case with NGC 5694, the cluster is not well described by a King profile (Carballo-Bello et al. 2012) but instead shows a number density profile that is well fitted by a power law (Sanna et al. 2014) to a distance of more than $30r_{e,s}$ (Figure 14). This is a remarkable result, as it means that we are able to detect NGC 5824 member stars out to a distance of at least ~ 180 pc from its center.

4.4.32. Ursa Minor

The Ursa Minor galaxy was discovered by Wilson (1955) using photographic plates from the 48 inch Palomar Schmidt telescope taken for the National Geographic Society–Palomar Observatory Sky Survey. Hodge (1964a) used plates taken with the 120 inch Lick and 48 inch Palomar Schmidt telescopes to carry out a star-count analysis of Ursa Minor. He found an ellipticity of $\epsilon = 0.55 \pm 0.10$ and fitted a King (1962) model to measure a physical major-axis radius of 1.5 ± 0.5 kpc ($75' \pm 25'$).

In a pioneering study, Aaronson & Olszewski (1987) measured a velocity dispersion of $\sigma_v = 11 \pm 3$ km s^{-1} for Ursa Minor, prompting many subsequent investigations into the dark matter content of this and other Galactic dSph galaxies (e.g., Lake 1990; Pryor & Kormendy 1990). Hargreaves et al. (1994), Olszewski et al. (1995, 1996), Wilkinson et al. (2004), and Muñoz et al. (2005) led subsequent spectroscopic campaigns, collecting hundreds of radial velocity measurements over the following decade.

More recent photometric studies have focused on the galaxy's morphological structure, including a survey of main-sequence and blue HB stars by Martínez-Delgado et al. (2001) and K giants by Palma et al. (2003). Both studies reported the detection of probable member stars well beyond the King tidal radius. Based on this finding and the elongated shape of the galaxy, these authors have argued that Ursa Minor has experienced significant tidal heating.

In our program, we used CFHT to cover the galaxy in a 2×2 mosaic, an area of nearly 4 deg^2 . Our CMD reaches roughly 3 mag below the MSTO, revealing in great detail all of the galaxy’s evolutionary sequences, including a large population of blue straggler stars (Figure 25). We measure the effective radius to be $r_{e,s} = 383 \pm 2 \text{ pc}$. Although this is significantly larger than the value of $r_h = 180 \text{ pc}$ from Irwin & Hatzidimitriou (1995), it is consistent with the measurement of $r_h \sim 390 \text{ pc}$ from Bellazzini et al. (2002). We find an absolute magnitude of $M_V = -9.0 \pm 0.05$. In agreement with previous studies, the galaxy is found to be fairly elongated, with a global ellipticity of $\epsilon = 0.55 \pm 0.10$. On the other hand, its isodensity contour map (Figure 14) shows no obvious secondary peak in the density distribution, contrary to several previous reports (e.g., Kleya et al. 1998; Bellazzini et al. 2002; Palma et al. 2003; Pace et al. 2014).

4.4.33. Palomar 14

Palomar 14 was discovered by Arp & van den Bergh (1960) from an inspection of Palomar Sky Survey plates. It is a sparsely populated cluster located at a galactocentric distance of $R_{GC} \simeq 71 \text{ kpc}$. Palomar 14 exhibits the second-parameter effect, like most of its outer halo counterparts (da Costa et al. 1982; Harris & van den Bergh 1984). Sarajedini (1997) was the first to recognize that Palomar 14 was indeed younger than the inner halo clusters by $\sim 3\text{--}4 \text{ Gyr}$, a typical value for remote halo clusters. The age difference was later revised to $1.5\text{--}2 \text{ Gyr}$ by Dotter et al. (2008a) using high-quality *HST*/WFPC2 photometry.

We observed Palomar 14 in a single CFHT pointing, reaching ~ 1.5 mag below the level of the MSTO (Figure 25). From our data, we measure an absolute magnitude of $M_V = -5.4 \pm 0.2$ and an effective radius of $r_{e,s} = 32 \pm 1 \text{ pc}$, leading to a surface brightness that is among the faintest for clusters in our sample. We also find a relatively high ellipticity (compared to other clusters) of $\epsilon = 0.11 \pm 0.01$. It has been reported that the cluster shows some evidence for tidal interaction (Jordi & Grebel 2010; Sollima et al. 2011). In these previous studies, the morphology appears distorted, especially in its outer regions, suggesting the presence of tidal debris. Our isodensity map (Figure 14) shows a possible elongation in the E–W direction, similar to published results and consistent with the presence of nascent tidal tails.

4.4.34. Hercules

Belokurov et al. (2007) reported the discovery of this remote, low-luminosity satellite in SDSS DR5 data. Soon after its discovery, Coleman et al. (2007) presented deeper follow-up imaging taken with the Large Binocular Telescope. Their CMD reached ~ 1.5 mag below the MSTO, revealing a highly elongated structure. Indeed, these authors noted that Hercules is the most elongated of the ultra-faint satellites, with an axial ratio of $\sim 3:1$, and also one of the largest, with a half-light radius of $r_h \sim 170 \text{ pc}$.

Despite its large distance, Hercules is likely to be among the most tidally stripped of satellites, given its elongated shape and unusual morphology. Evidence for tidal disruption—both photometric and spectroscopic—has been reported in the past (e.g., Coleman et al. 2007; Adén et al. 2009; Sand et al. 2009; Martin & Jin 2010; Deason et al. 2012; Blańa et al. 2015; Garling et al. 2018). Martin & Jin (2010) found the spatial orientation of Hercules’s elongation to be consistent with an

orbit that would bring the satellite as close as 6_{-2}^{+9} kpc from the Galactic center, making the tidal disruption scenario a plausible hypothesis.

Our CFHT imaging for Hercules (covering a $2^\circ \times 1^\circ$ field) reaches almost a full magnitude below the MSTO (Figure 25). Although its CMD is scarcely populated, the evolved sequences are clearly visible. A potential blue straggler population is also apparent, as was seen in the deep *HST*/ACS photometry of Brown et al. (2012). We measure the overall ellipticity of Hercules to be $\epsilon = 0.69 \pm 0.04$, although the ellipticity in the inner parts can be even larger. The estimated absolute magnitude is $M_V = -5.2 \pm 0.4$, and its effective radius is $r_{e,s} = 230 \pm 23 \text{ pc}$, making Hercules somewhat fainter and larger than the original estimates from Belokurov et al. (2007) and Coleman et al. (2007). As expected, our data show an unusually elongated morphology (Figure 14), consistent with earlier studies.

4.4.35. NGC 6229

NGC 6229, discovered by Herschel in 1787, is located at a galactocentric distance of $R_{GC} \simeq 30 \text{ kpc}$. NGC 6229 is another halo cluster that exhibits the second-parameter effect. There is, however, no direct evidence to date that NGC 6229 is younger than its inner halo counterparts.

Our CFHT photometry reaches ~ 3.5 mag below the MSTO and reveals a well-populated HB that covers nearly a full magnitude in $(g - r)$ color and exhibits an apparent bifurcation at its red edge (see Figure 26). From isochrone fitting, we estimate that NGC 6229’s age is consistent with being old (i.e., $>13 \text{ Gyr}$). We measure an absolute magnitude of $M_V = -8.0 \pm 0.2$ and an effective radius of $r_{e,s} = 3.19 \pm 0.09 \text{ pc}$. We are able to detect probable member stars out to $25r_e$, similar to other bright halo clusters in the range $30 \text{ kpc} < R_{GC} < 40 \text{ kpc}$. Our isodensity map reveals the cluster to be fairly round in shape, $\epsilon = 0.02 \pm 0.01$, with a regular morphology and no signs of tidal distortion (Figure 15). As expected due to crowding, its number density profile produced only from star counts is poorly fit by the parameters derived from the surface brightness analysis described in Section 3.3.

4.4.36. Palomar 15

This diffuse and somewhat poorly studied cluster was discovered by Zwicky (1959). It is located in the Galactic anticenter direction at a relatively low Galactic latitude, ($l = 19^\circ, b = 24^\circ$), which results in a significantly reddened CMD. Dotter et al. (2011) used imaging from *HST*/ACS to derive an age of $13 \pm 1.5 \text{ Gyr}$.

Our CFHT images reach nearly 2 mag fainter than the MSTO, as shown in Figure 26. The cluster sequences, including its blue HB, appear somewhat broader than usual for sparse halo clusters, probably owing to differential reddening across the field. From our data, we derived an absolute magnitude of $M_V = -5.6 \pm 0.2$ and an effective radius of $r_{e,s} = 19.0 \pm 0.4 \text{ pc}$. Palomar 15’s overall ellipticity is $\epsilon = 0.05 \pm 0.02$, and its two-dimensional morphology shows no irregularities or signs of tidal interaction (Figure 15). We note that Myeong et al. (2017), using photometry taken with the DECam imager on the 4 m Blanco telescope at CTIO, reported the presence of tidal-like substructure on the outskirts of Palomar 15.

4.4.37. *Draco*

The Draco dSph galaxy was discovered by Wilson (1955) from an inspection of plates taken with the 48 inch Palomar Schmidt telescope for the National Geographic Society–Palomar Observatory Sky Survey. Hodge (1964b) used 200 inch Palomar plates, among others, to perform star counts in the galaxy. His analysis showed that the galaxy resembled other “Sculptor-type” systems; i.e., it had an elliptical appearance, with $\epsilon = 0.29 \pm 0.04$, and was well represented by a King (1962) model having a limiting radius of 510 ± 40 pc (for his adopted distance of 68 kpc).

During the last decade, attention has been devoted to the possibility that Draco may be tidally influenced by the Milky Way. Using the radial velocity data of Kleyna et al. (2002), Muñoz et al. (2005) reanalyzed Draco’s velocity dispersion profile. They found it to remain flat beyond the nominal tidal radius, suggesting tidal stripping as a possible explanation. On the other hand, several deep photometric studies (e.g., Odenkirchen et al. 2001; Klessen et al. 2003; Ségall et al. 2007) have been unable to detect the morphological features expected for tidally disrupting systems, such as isophotal twisting or tidal tails.

In our survey, we used CFHT to image Draco in a 2×2 grid pattern, covering an area of nearly 4 deg^2 and reaching more than 2 mag below the MSTO. The combination of depth and areal coverage makes our imaging survey the most extensive to date for this galaxy. Our CMD (Figure 26) reveals Draco’s extended HB, as well as its very sizable population of blue stragglers. We measure an effective radius of $r_{e,s} = 219 \pm 2$ pc, an absolute magnitude of $M_V = -8.7 \pm 0.1$, and a mean ellipticity of $\epsilon = 0.30 \pm 0.01$, consistent with previous determinations. With our photometry, we are able to study Draco’s two-dimensional morphology to a fainter surface brightness limit than any previous study. However, the galaxy’s isodensity contour map shows no sign of irregularities (Figure 15) that would suggest it has been strongly perturbed by the Galactic tidal field.

4.4.38. *NGC 7006*

NGC 7006 is a low-latitude globular cluster, ($l = 64^\circ$, $b = -19^\circ$), located at a galactocentric distance of $R_{GC} \simeq 38$ kpc. Several early studies placed it on the far side of the Galaxy, at distances greater than $R_{GC} \sim 50$ kpc (e.g., Shapley 1920, 1930; Shapley & Mayberry 1921; Baade 1935). As a result, it attracted considerable attention in studies of the spatial extent of the Galaxy; i.e., prior to 1950, it was considered the second most distant cluster in the Milky Way, after NGC 2419.

Our CFHT photometry reaches ~ 4 mag below the level of the MSTO (Figure 26). We measure an absolute magnitude of $M_V = -7.4 \pm 0.1$ and an effective radius of $r_{e,s} = 6.11 \pm 0.12$ pc. Although its surface brightness profile is not as extended as those of NGC 5694 or NGC 5824, we are able to detect likely member stars out to $\sim 16r_e$. Like most clusters in our sample, its morphology is round and regular (Figure 15), with an overall ellipticity of $\epsilon = 0.07 \pm 0.01$ and no signs of tidal distortion. We see no evidence for the extratidal halo reported by Jordi & Grebel (2010) from an analysis of SDSS images.

4.4.39. *Segue 3*

This extremely faint satellite was discovered by Belokurov et al. (2010) using SDSS DR7 data. From follow-up imaging acquired at the 4 m KPNO telescope, these authors estimated a half-light radius of $r_h \sim 3$ pc and an absolute magnitude of $M_V = -1.2$, making Segue 3 one of the faintest Galactic satellites currently known. Based on its compact size, they classified the system as a faint globular cluster.

Fadely et al. (2011) used deep imaging taken with the 6.5 m Baade telescope to conclude that Segue 3 is an old halo cluster located at a galactocentric distance of $R_{GC} \sim 17$ kpc. Soon afterward, Ortolani et al. (2013) used *BVI* imaging from the Telescopio Nazionale Galileo to argue that Segue 3 is, in fact, a much younger system, with an age of just ~ 3.2 Gyr, that is located at a distance of $R_{GC} \sim 29$ kpc. Recently, Boettcher et al. (2013) carried out a search for RR Lyrae stars in the Segue 3 field but were unable to identify any promising candidates.

From our Clay imaging, we measure an absolute magnitude of $M_V = -0.9 \pm 0.7$ and an effective radius of $r_{e,s} = 4.1 \pm 0.7$ pc, making Segue 3 somewhat fainter and larger than the estimates of Belokurov et al. (2010). Age, distance, and metallicity estimates from isochrone fitting are critically dependent on the presence of subgiant stars. In our CMD (Figure 27), a handful of stars are found in the subgiant branch region; if these are bona fide cluster members, then our isochrone fitting results are consistent with the findings of Ortolani et al. (2013), supporting the observation that Segue 3 is (by far) the youngest of the outer halo clusters. However, given the extremely sparse nature of the cluster’s upper sequences, definitive measurements of age, metallicity, and distance are probably not possible at this time. Spectroscopic identification of member stars will be needed to settle this discrepancy.

4.4.40. *Pisces II*

The discovery of Pisces II was reported simultaneously with that of Segue 3 by Belokurov et al. (2010), who detected it as an overdensity in SDSS DR7 data. Based on follow-up imaging acquired with the KPNO 4 m telescope, the authors calculated an absolute magnitude of $M_V = -5.0$, a half-light radius of $r_h = 58$ pc, and a distance of ~ 182 kpc. Sand et al. (2012) obtained deeper imaging with the Clay telescope, revising the absolute magnitude to $M_V = -4.1 \pm 0.4$ and confirming the size and distance measurements of Belokurov et al. (2010).

From our Clay imaging, we measure an effective radius of $r_{e,s} = 64 \pm 10$ pc, an absolute magnitude of $M_V = -4.2 \pm 0.4$, and an overall ellipticity of $\epsilon = 0.40 \pm 0.10$. These values are all consistent with the results of Sand et al. (2012). The CMD of Pisces II (Figure 27) shows a sparsely populated but well-defined blue HB. Its two-dimensional morphology shows no sign of tidal stripping.

4.4.41. *Palomar 13*

The sparsely populated globular cluster Palomar 13 was discovered by Wilson (1955) using plates from the National Geographic Society–Palomar Observatory Sky Survey. Based on *HST*/WFC3 imaging that reached $m_{F606W} \sim 27.2$, Hamren et al. (2013) reported an age of 13.4 ± 0.5 Gyr and a metallicity of $[\text{Fe}/\text{H}] \sim -1.6$ dex.

We observed Palomar 13 in a single pointing with CFHT. Our photometry reaches to $g \sim 25$, roughly 4 mag below the

MSTO (Figure 27). The CMD reveals a prominent blue straggler population, consistent with previous findings (Côté et al. 2002; Clark et al. 2004). From our data, we measure an effective radius of $r_e = 9.5 \pm 0.7$ pc and an absolute magnitude of $M_V = -2.8 \pm 0.6$. The overall ellipticity is measured to be $\epsilon = 0.10 \pm 0.06$, on the high side for globular clusters.

4.4.42. NGC 7492

NGC 7492 is a sparse and relatively nearby ($R_{GC} \simeq 25$ kpc) outer halo cluster. The first CCD study of the cluster was carried out by Buonanno et al. (1987), whose CMD reached below the level of the MSTO. From isochrone fitting, these authors estimated a metallicity of $[Fe/H] = -1.51 \pm 0.20$ dex. Côté et al. (1991) presented a deep CMD, confirming the metallicity estimate of Buonanno et al. (1987) and refining their distance estimates.

Figure 27 shows the CMD based on our CFHT imaging, which reaches about 4 mag below the level of the MSTO. We measure an effective radius of $r_{e,s} = 9.6 \pm 0.1$ pc and an absolute magnitude of $M_V = -6.10 \pm 0.05$. We see no indication of surrounding tidal debris, contrary to the claims of Lee et al. (2004). Its isodensity contour map (Figure 16) shows a regular and almost perfectly round morphology with $\epsilon = 0.02 \pm 0.02$. However, we do note that an additional population of main-sequence stars seems to be present in the NGC 7492 field, located at a similar line-of-sight distance. In a companion paper, we show that this new population probably corresponds to debris from the Sagittarius dwarf galaxy and is likely not physically associated with the cluster (Paper I).

4.5. Comments on Secondary Targets

Basic data for the 14 satellites that make up our secondary sample are presented in Table 1, and our best-fit exponential, Plummer, King, and Sérsic parameters for these systems are summarized in Tables 3–5. Like our primary objects, these secondary targets include a mixture of ultra-faint dwarf galaxies, diffuse star clusters, and low-luminosity objects of an as-yet-undetermined nature. The full sample consists of Balbinot 1 (Balbinot et al. 2013); Laevens 1 and 2 (Laevens et al. 2014, 2015b); Kim 1 (Kim & Jerjen 2015a); Hor II (Kim & Jerjen 2015b); Hyd II (Martin et al. 2015); Gru I (Koposov et al. 2015a); Ind I (Koposov et al. 2015a; Kim et al. 2015b); the DES Collaboration et al. (2015); and Eri III, Hor I, Ret II, Eri II, Pic I, and Pho II (Koposov et al. 2015a; the DES Collaboration et al. 2015).

Our analysis of these objects is based on the same data used in the discovery papers, i.e., either our own analysis of the original images retrieved from the archive or photometric catalogs kindly provided by the authors (see Section 2.2). Thus, we expect no dramatic differences between our measurements and those available in the literature. Still, our analysis of these systems allows us to (1) carry out an independent check on our methodology (which can be important for faint, diffuse objects observed against a background of contaminating sources) and (2) report photometric and structural parameters for these objects that were measured in an identical manner as those for our primary sample.

Figure 28 presents a comparison of our measured absolute magnitudes, ellipticities, and effective radii with those reported in the above papers; in all cases, residuals are in the sense of

our values minus those in the literature. The horizontal dotted and dashed lines show the mean differences and $\pm 1\sigma$ scatter in each case, i.e.,

$$\begin{aligned}\Delta M_V &= -0.02 \pm 0.56 \\ \Delta \epsilon / \epsilon &= +0.09 \pm 0.16 \\ \Delta R_e / R_e &= -0.14 \pm 0.43.\end{aligned}\quad (11)$$

For most systems, there is very good agreement between our measurements and those in the literature (e.g., Laevens 2, Eri III, Hor I, Hyd II, Ind I, Balbinot 1, Pic I, and Gru I). In a few other cases, there is marginal disagreement in one or more derived parameters.

- Hor II. We measure $M_V = -1.54 \pm 1.02$ and $R_e = 64 \pm 30$ pc, slightly fainter and larger than reported by Kim & Jerjen (2015b), who gave $M_V = -2.60 \pm 0.20$ and $R_e = 47 \pm 10$ pc. We also find this system to be more flattened ($\epsilon = 0.86^{+0.14}_{-0.19}$) than previously reported ($\epsilon = 0.52^{+0.13}_{-0.17}$). However, most parameters are consistent within their respective errors.
- Ret II. We find this system to be somewhat brighter ($M_V = -3.65 \pm 0.24$) and larger ($R_e = 49 \pm 2$ pc) than reported by Koposov et al. (2015a), who found $M_V = -2.70 \pm 0.10$ and $R_e = 32 \pm 2$ pc. However, our values are in good agreement with those ($M_V = -3.60 \pm 0.10$ and $R_e = 55 \pm 5$ pc) quoted in the DES Collaboration et al. (2015), and all three studies measure an ellipticity in the range 0.56–0.60.
- Eri II. We measure $M_V = -7.19 \pm 0.09$ and $R_e = 200 \pm 19$ pc, slightly brighter and larger than reported by Koposov et al. (2015a), who found $M_V = -6.60 \pm 0.10$ and $R_e = 169 \pm 16$ pc. By contrast, the DES Collaboration et al. (2015) reported $M_V = -7.40 \pm 0.10$ and $R_e = 172 \pm 57$ pc. Crnojevic et al. (2016) published deeper photometry and reported $M_V = -7.1 \pm 0.3$ and $R_e = 277 \pm 14$ pc.
- Laevens 1. We measure $M_V = -4.62 \pm 0.22$ and $R_e = 20.7 \pm 2.9$ pc, making this system somewhat fainter and smaller than reported by Laevens et al. (2014): $M_V = -5.50 \pm 0.50$ and $R_e = 28.8 \pm 2.4$ pc. The respective ellipticities (0.11 ± 0.10 and 0.08 ± 0.08) are in good agreement.
- Kim 1. Parameter estimation for this system is especially challenging given its very low luminosity (the lowest of any known Galactic satellite). We find $M_V = +0.74 \pm 1.05$, $R_e = 5.4 \pm 1.3$ pc, and $\epsilon = 0.67 \pm 0.22$. For comparison, Kim & Jerjen (2015a) reported $M_V = +0.30 \pm 0.50$, $R_e = 6.9 \pm 0.6$ pc, and $\epsilon = 0.42 \pm 0.10$. However, all measurements are consistent within the uncertainties.
- Pho II. Our measurements ($M_V = -3.28 \pm 0.63$ and $R_e = 38.9 \pm 6.5$ pc) point to a somewhat brighter and more extended system than found by Koposov et al. (2015a): $M_V = -2.80 \pm 0.20$ and $R_e = 26.0 \pm 6.2$ pc. In both cases, though, the measurements agree to within their respective errors. We note that the estimates of the DES Collaboration et al. (2015), $M_V = -3.70 \pm 0.40$ and $R_e = 33^{+20}_{-11}$ pc, are more in line with our measurements.

5. Discussion: The Magnitude–Size Relationship

As discussed in Section 1, our photometric catalogs and structural parameters have already formed the basis of several published studies (Bradford et al. 2011; Muñoz et al. 2012b; Santana et al. 2013; Carballo-Bello et al. 2015, 2017; Santana et al. 2016) and will be used in a future paper to explore the scaling relations of outer halo satellites. For the time being, we use our measurements to examine the distribution of these objects in the size–luminosity plane, a customary tool for studying the structural properties of stellar systems in the Milky Way, M31, and nearby galaxy groups and clusters (e.g., Kormendy 1990; Côté et al. 2002; Willman et al. 2005a; Belokurov et al. 2007; Dabringhausen et al. 2008; Huxor et al. 2011; Misgeld & Hilker 2011; Tollerud et al. 2011; Norris et al. 2014).

Figure 29 shows the distribution of 81 Galactic substructures in the $\log R_e$ – $\log L_V$ diagram.⁸ Objects have been labeled individually and color-coded according to the samples from which they are drawn, with primary, secondary, and tertiary objects shown in blue, red, and green, respectively. For comparison, we also show lines of constant surface brightness: $\mu_V = 18, 22, 26,$ and 30 mag arcsec^{−2}. These limits roughly bound the surface brightnesses of the outer halo substructures known at this time.

The same data are shown again in Figure 30 but now excluding the four objects belonging to the inner halo. For clarity, the labels have been removed, although the color-coding remains the same. At the time of writing, this figure shows the complete sample of 77 known outer halo substructures, irrespective of their classification as globular cluster, classical dwarf, or ultra-faint dwarf galaxy. The histograms in the bottom and right panels show the projected distribution of these satellites in terms of effective radius and absolute magnitude.

Two points are worth noting in this figure. First, the dramatic increase in the number of cataloged satellites during the past two decades has been accompanied by a commensurate increase in their structural diversity. For instance, the 77 objects shown in Figure 30 span factors of $\sim 10^3$ in effective radius, $\sim 10^6$ in V -band luminosity, and $\sim 10^{4.8}$ in surface brightness. Clearly, these substructures represent a remarkably diverse population. Second, with the benefit of an expanded sample size, a homogeneous analysis based on high-quality imaging, and a uniform parameterization of the density profiles, the separation of halo substructures into two distinct populations—i.e., globular clusters and dwarf galaxies—with fundamentally different formation paths has become difficult to support, at least on the basis of photometric and structural parameters alone. Incompleteness in this diagram is notoriously difficult to gauge, but the once-clear dichotomy in the sizes of globular clusters and dwarf galaxies has blurred considerably during the past decade (although a paucity of satellites having effective radii of ~ 30 – 100 pc and luminosities of $\sim 10^5 L_\odot$ may persist). In any event, Figure 30 demonstrates that spectroscopy for individual member stars will be indispensable for establishing the true nature of new substructures through dynamical mass estimates and measurements of star-to-star variations in chemical abundances.

⁸ For completeness, we include four known or suspected dwarf satellites of the Milky Way (Sag, Kim 1, Draco II, and Tucana III) that have $R_{GC} < 25$ kpc and are thus, strictly speaking, not members of the outer halo according to the definition adopted here.

Finally, we reflect upon the discovery histories of Galactic globular clusters and dwarf galaxies with the benefit of a baseline that now spans three and a half centuries. In Figure 31, we show how the census of halo substructures has evolved with time. The nine panels in this figure show the size–magnitude diagram of satellites at the time indicated in each panel. We plot globular clusters from Harris (1996) with $R_{GC} < 25$ kpc as blue dots and satellites in the outer halo as red crosses. It is striking to see the role that surface brightness has played in defining the census of known substructures, with the ensemble of known satellites at any time generally lying above a well-defined threshold in surface brightness (e.g., Disney 1976). As a result, discoveries have historically been driven by improvements in telescope technology, with the most dramatic gains in history (see Figure 1 of Paper I) coming on the heels of surveys made with wide-field instruments (e.g., the surveys of W. Herschel and J. Dunlop, the Palomar Sky Survey conducted with the 48 inch Oschin Schmidt telescope, and, most recently, the SDSS, Pan-STARRS, and DES surveys). The highly anticipated next step will come from LSST, which is expected to add hundreds of new objects to our census of halo substructures (e.g., Tollerud et al. 2008).

6. Summary

In this paper, we have presented homogeneous photometric and structural parameters for a large sample of substructures in the outer halo of the Milky Way. Our measurements are based on wide-field gr images for 44 satellites obtained with the MegaCam instruments on the CFHT and Clay telescopes, supplemented by a reanalysis of gr data for an additional 14 satellites. Because we imposed no selection on the basis of morphology, our targets include a mixture of remote globular clusters, classic dSph galaxies, and ultra-faint dwarfs.

Photometric and structural parameters were derived by using a two-dimensional maximum-likelihood technique to fit four different density laws: exponential, Plummer (1911), King (1962), and Sérsic (1968) profiles. For seven high surface brightness targets, these four models were fitted to composite one-dimensional profiles obtained from a combination of star counts and surface photometry. We tabulate our best-fit photometric and structural parameters, including ellipticities, position angles, effective radii, Sérsic indices, absolute magnitudes, and surface brightness measurements. We compare our results to measurements in the literature and find generally good agreement for most systems. A critical evaluation of the fitted density laws suggests that the Sérsic model is the preferred parameterization for these substructures, as it has the flexibility to fit the profiles for satellites spanning a range in luminosity, surface brightness, and morphology.

We examine the isodensity contour maps and CMDs for our targets and present a careful comparison with previous results for each object in our survey. As a rule, we find most of the globular clusters in our survey to have regular morphologies, with few signs of strong tidal interactions with the Milky Way. A notable exception is Palomar 14, which shows a faint, elongated distribution in its outer regions consistent with the presence of nascent tidal tails, as has also been reported by Sollima et al. (2011). The classical dSphs in our survey are often elongated but otherwise show regular density contours, with no clear signs of tidal disruption; some systems, like UMi and Carina, for which claims of tidal stripping exist in the literature will need a closer analysis to make conclusive







statements in this context. The situation for several of the ultra-faint galaxies is different, with a number of systems, such as Hercules, UMa I and II, and Willman 1, showing unusual morphologies and potential tidal features consistent with at least some degree of stripping.

Finally, we examine the distribution of outer halo satellites in the size–magnitude diagram using our catalog of photometric and structural parameters. A wide diversity in structural parameters is observed, with satellites spanning factors of $\sim 10^3$ in effective radius, $\sim 10^6$ in V-band luminosity, and $\sim 10^{4.8}$ in surface brightness. Indeed, based on the available sample and measured parameters, the separation of halo substructures into two distinct, nonoverlapping populations—i.e., globular clusters and dwarf galaxies—having fundamentally different origins seems increasingly difficult to support. In the coming LSST era, when vast numbers of satellites are expected to be discovered, spectroscopy for individual member stars will prove essential for establishing the true nature of these systems through dynamical mass measurements and elemental abundance ratios measured for individual stars.

This paper is based on observations obtained with the MegaPrime/MegaCam, a joint project of the Canada–France–Hawaii Telescope (CFHT) and CEA/DAPNIA, at CFHT, which is operated by the National Research Council (NRC) of Canada, the Institut National des Science de l’Univers of the Centre National de la Recherche Scientifique (CNRS) of France, and the University of Hawaii. This work was supported in part by the facilities and staff of the Yale University Faculty of Arts and Sciences High Performance Computing Center. The authors would like to thank an anonymous referee for helping us improve this article and Alan McConnachie for helpful discussions. R.R.M. and F.A.S. acknowledge partial support from project BASAL PFB-06. RRM also acknowledges support from FONDECYT project No. 1170364. M.G. acknowledges support from the National Science Foundation under award number AST-0908752 and the Alfred P. Sloan Foundation. S.G.D. was supported in part by NSF grants AST-1313422, AST-1413600, AST-1518308 and by the Ajax Foundation.

Facilities: CFHT, Magellan.

ORCID iDs

Patrick Côté  <https://orcid.org/0000-0003-1184-8114>
 Felipe A. Santana  <https://orcid.org/0000-0002-4023-7649>
 Marla Geha  <https://orcid.org/0000-0002-7007-9725>
 Grecco A. Oyarzún  <https://orcid.org/0000-0003-0028-4130>
 Peter B. Stetson  <https://orcid.org/0000-0001-6074-6830>
 S. G. Djorgovski  <https://orcid.org/0000-0002-0603-3087>

References

- Aaronson, M., & Olszewski, E. 1987, in IAU Symp. 117, Dark Matter in the Universe, ed. J. Kormendy & G. R. Knapp (Dordrecht: Reidel), 153
- Abell, G. O. 1955, *PASP*, **67**, 258
- Adén, D., Feltzing, S., Koch, A., et al. 2009, *A&A*, **506**, 1147
- Arp, H., & van den Bergh, S. 1960, *PASP*, **72**, 48
- Baade, W. 1935, *ApJ*, **82**, 396
- Baade, W., & Hubble, E. 1939, *PASP*, **51**, 40
- Balbinot, E., Santiago, B. X., da Costa, L., et al. 2013, *ApJ*, **767**, 101
- Battaglia, G., Tolstoy, E., Helmi, A., et al. 2006, *A&A*, **459**, 423
- Battaglia, G., Tolstoy, E., Helmi, A., et al. 2011, *MNRAS*, **411**, 1013
- Baumgardt, H., Côté, P., Hilker, M., et al. 2009, *MNRAS*, **396**, 2051
- Bellazzini, M., Ferraro, F. R., Origlia, L., et al. 2002, *AJ*, **124**, 3222
- Bellazzini, M., Mucciarelli, A., Sollima, A., et al. 2015, *MNRAS*, **446**, 3130
- Belokurov, V., Walker, M. G., Evans, N. W., et al. 2008, *ApJL*, **686**, L83
- Belokurov, V., Walker, M. G., Evans, N. W., et al. 2009, *MNRAS*, **397**, 1748
- Belokurov, V., Walker, M. G., Evans, N. W., et al. 2010, *ApJL*, **712**, L103
- Belokurov, V., Zucker, D. B., Evans, N. W., et al. 2006a, *ApJL*, **647**, L111
- Belokurov, V., Zucker, D. B., Evans, N. W., et al. 2006b, *ApJL*, **642**, L137
- Belokurov, V., Zucker, D. B., Evans, N. W., et al. 2007, *ApJ*, **654**, 897
- Blaña, M., Fellhauer, M., Smith, R., et al. 2015, *MNRAS*, **446**, 144
- Boettcher, E., Willman, B., Fadely, R., et al. 2013, *AJ*, **146**, 94
- Boulade, O., Charlot, X., Abbon, P., et al. 2003, *Proc. SPIE*, **4841**, 72
- Bradford, J. D., Geha, M., Muñoz, R. R., et al. 2011, *ApJ*, **743**, 167
- Brown, T. M., Tumlinson, J., Geha, M., et al. 2012, *ApJL*, **753**, L21
- Brown, T. M., Tumlinson, J., Geha, M., et al. 2014, *ApJ*, **796**, 91
- Buonanno, R., Corsi, C. E., Ferraro, I., & Fusi Pecci, F. 1987, *A&AS*, **67**, 327
- Cannon, R. D., Hawarden, T. G., & Tritton, S. B. 1977, *MNRAS*, **180**, 81P
- Caon, N., Capaccioli, M., & Rampazzo, R. 1990, *A&AS*, **86**, 429
- Carballo-Bello, J. A., Corral-Santana, J. M., Martínez-Delgado, D., et al. 2017, *MNRAS*, **467**, L91
- Carballo-Bello, J. A., Gieles, M., Sollima, A., et al. 2012, *MNRAS*, **419**, 14
- Carballo-Bello, J. A., Muñoz, R. R., Carlin, J. L., et al. 2015, *ApJ*, **805**, 51, (Paper IV)
- Carraro, G. 2005, *ApJ*, **621**, L61
- Carraro, G. 2009, *AJ*, **137**, 3809
- Carraro, G., Zinn, R., & Moni Bidin, C. 2007, *A&A*, **466**, 181
- Cesarsky, D. A., Lequeux, J., Laustsen, S., Schuster, H.-E., & West, R. M. 1977, *A&A*, **61**, L31
- Chambers, K. C., Magnier, E. A., Metcalfe, N., et al. 2016, arXiv:1612.05560
- Clark, L. L., Sandquist, E. L., & Bolte, M. 2004, *AJ*, **128**, 3019
- Cohen, J. G., & Kirby, E. N. 2012, *ApJ*, **760**, 86
- Cohen, J. G., Kirby, E. N., Simon, J. D., & Geha, M. 2010, *ApJ*, **725**, 288
- Coleman, M. G., Da Costa, G. S., & Bland-Hawthorn, J. 2005, *AJ*, **130**, 1065
- Coleman, M. G., de Jong, J. T. A., Martin, N. F., et al. 2007, *ApJL*, **668**, L43
- Correnti, M., Bellazzini, M., Dalessandro, E., et al. 2011, *MNRAS*, **417**, 2411
- Côté, P., Djorgovski, S. G., Meylan, G., Castro, S., & McCarthy, J. K. 2002, *ApJ*, **574**, 783
- Côté, P., Ferrarese, L., Jordán, A., et al. 2007, *ApJ*, **671**, 1456
- Côté, P., Richer, H. B., & Fahlman, G. G. 1991, *AJ*, **102**, 1358
- Crojevic, D., Sand, D. J., Zaritsky, D., et al. 2016, *ApJ*, **824**, L14
- Dabringhausen, J., Hilker, M., & Kroupa, P. 2008, *MNRAS*, **386**, 864
- da Costa, G. S. 1995, *PASP*, **107**, 937
- da Costa, G. S., Ortolani, S., & Mould, J. 1982, *ApJ*, **257**, 633
- Deason, A. J., Belokurov, V., Evans, N. W., Watkins, L. L., & Fellhauer, M. 2012, *MNRAS*, **425**, L101
- de Boer, T. J. L., Tolstoy, E., Hill, V., et al. 2012, *A&A*, **539**, A103
- de Jong, J. T. A., Harris, J., Coleman, M. G., et al. 2008, *ApJ*, **680**, 1112
- de Jong, J. T. A., Martin, N. F., Rix, H.-W., et al. 2010, *ApJ*, **710**, 1664
- Dias, W. S., Alessi, B. S., Moitinho, A., & Lépine, J. R. D. 2002, *A&A*, **389**, 871
- Diehl, H. T., Abbott, T. M. C., Annis, J., et al. 2014, *Proc. SPIE*, **9149**, 91490V
- Disney, M. J. 1976, *Natur*, **263**, 573
- Djorgovski, S. 1993, in ASP Conf. Ser. 50, Structure and Dynamics of Globular Clusters, ed. S. G. Djorgovski & G. Meylan (San Francisco, CA: ASP), 373
- Dominguez, R., Fellhauer, M., Blaña, M., et al. 2016, *MNRAS*, **461**, 3630
- Dotter, A., Chaboyer, B., Jevremović, D., et al. 2008a, *ApJS*, **178**, 89
- Dotter, A., Sarajedini, A., & Anderson, J. 2011, *ApJ*, **738**, 74
- Dotter, A., Sarajedini, A., & Yang, S. 2008b, *AJ*, **136**, 1407
- Drlica-Wagner, A., Bechtol, K., Rykoff, E. S., et al. 2015, *ApJ*, **813**, 109
- Fadely, R., Willman, B., Geha, M., et al. 2011, *AJ*, **142**, 88
- Fellhauer, M., Evans, N. W., Belokurov, V., et al. 2007, *MNRAS*, **375**, 1171
- Ferrarese, L., Côté, P., Jordán, A., et al. 2006, *ApJS*, **164**, 334
- Ferrarese, L., Côté, P., Sánchez-Janssen, R., et al. 2016, *ApJ*, **824**, 10
- Fischer, P., Welch, D. L., Cote, P., Mateo, M., & Madore, B. F. 1992, *AJ*, **103**, 857
- Gallart, C., Freedman, W. L., Aparicio, A., Bertelli, G., & Chiosi, C. 1999a, *AJ*, **118**, 2245
- Gallart, C., Freedman, W. L., Mateo, M., et al. 1999b, *ApJ*, **514**, 665
- Garling, C., Willman, B., Sand, D., et al. 2018, *ApJ*, **852**, 44
- Geha, M., Willman, B., Simon, J. D., et al. 2009, *ApJ*, **692**, 1464
- Gilmore, G., Wilkinson, M. I., Wyse, R. F. G., et al. 2007, *ApJ*, **663**, 948
- Graham, A. W., Erwin, P., Trujillo, I., & Asensio Ramos, A. 2003, *AJ*, **125**, 2951
- Graham, A. W., & Guzmán, R. 2003, *AJ*, **125**, 2936
- Hamren, K. M., Smith, G. H., Guhathakurta, P., et al. 2013, *AJ*, **146**, 116
- Hargreaves, J. C., Gilmore, G., Irwin, M. J., & Carter, D. 1994, *MNRAS*, **271**, 693

- Harrington, R. G., & Wilson, A. G. 1950, *PASP*, **62**, 118
- Harris, W. E. 1976, *AJ*, **81**, 1095
- Harris, W. E. 1980, *PASP*, **92**, 43
- Harris, W. E. 1996, *AJ*, **112**, 1487
- Harris, W. E., Durrell, P. R., Petitpas, G. R., Webb, T. M., & Woodworth, S. C. 1997, *AJ*, **114**, 1043
- Harris, W. E., & van den Bergh, S. 1984, *AJ*, **89**, 1816
- Hodge, P. W. 1961, *AJ*, **66**, 384
- Hodge, P. W. 1962, *AJ*, **67**, 125
- Hodge, P. W. 1963, *AJ*, **68**, 470
- Hodge, P. W. 1964a, *AJ*, **69**, 438
- Hodge, P. W. 1964b, *AJ*, **69**, 853
- Hodge, P. W. 1971, *ARA&A*, **9**, 35
- Homma, D., Chiba, M., Okamoto, S., et al. 2016, *ApJ*, **832**, 21
- Homma, D., Chiba, M., Okamoto, S., et al. 2018, *PASJ*, **70**, 18
- Hurley-Keller, D., Mateo, M., & Nemeč, J. 1998, *AJ*, **115**, 1840
- Huxor, A. P., Ferguson, A. M. N., Tanvir, N. R., et al. 2011, *MNRAS*, **414**, 770
- Inman, R. T., & Carney, B. W. 1987, *AJ*, **93**, 1166
- Irwin, M., & Hatzidimitriou, D. 1995, *MNRAS*, **277**, 1354
- Irwin, M. J., Belokurov, V., Evans, N. W., et al. 2007, *ApJL*, **656**, L13
- Irwin, M. J., Bunclark, P. S., Bridgeland, M. T., & McMahon, R. G. 1990, *MNRAS*, **244**, 16P
- Irwin, M. J., Demers, S., & Kunkel, W. E. 1995, *ApJL*, **453**, L21
- Jerjen, H., & Binggeli, B. 1997, in ASP Conf. Ser. 116, *The Nature of Elliptical Galaxies*, ed. M. Arnaboldi, G. S. Da Costa, & P. Saha (San Francisco, CA: ASP), 239
- Jordi, K., & Grebel, E. K. 2010, *A&A*, **522**, A71
- Jordi, K., Grebel, E. K., & Ammon, K. 2006, *A&A*, **460**, 339
- Kim, D., & Jerjen, H. 2015a, *ApJ*, **799**, 73
- Kim, D., & Jerjen, H. 2015b, *ApJ*, **808**, L39
- Kim, D., Jerjen, H., & Geha, M. 2016, *ApJ*, **833**, 16
- Kim, D., Jerjen, H., Mackey, D., et al. 2015a, *ApJL*, **804**, L44
- Kim, D., Jerjen, H., Milone, A. P., et al. 2015b, *ApJ*, **803**, 63
- King, I. 1962, *AJ*, **67**, 471
- Kirby, E. N., Boylan-Kolchin, M., Cohen, J. G., et al. 2013a, *ApJ*, **770**, 16
- Kirby, E. N., Cohen, J. G., Simon, J. D., et al. 2017, *ApJ*, **838**, 83
- Kirby, E. N., Simon, J. D., & Cohen, J. G. 2015, *ApJ*, **810**, 56
- Kirby, E. N. M., Cohen, J. G., Guhathakurta, P., et al. 2013b, *ApJ*, **779**, 102
- Klessen, R. S., Grebel, E. K., & Harbeck, D. 2003, *ApJ*, **589**, 798
- Kleyna, J. T., Geller, M. J., Kenyon, S. J., Kurtz, M. J., & Thorstensen, J. R. 1998, *AJ*, **115**, 2359
- Kleyna, J. T., Wilkinson, M. I., Evans, N. W., Gilmore, G., & Frayn, C. 2002, *MNRAS*, **330**, 792
- Koch, A., & Côté, P. 2010, *A&A*, **517**, A59
- Koch, A., Côté, P., & McWilliam, A. 2009a, *A&A*, **506**, 729
- Koch, A., Grebel, E. K., Wyse, R. F. G., et al. 2006, *AJ*, **131**, 895
- Koch, A., Kleyna, J. T., Wilkinson, M. I., et al. 2007, *AJ*, **134**, 566
- Koch, A., & Rich, R. M. 2014, *ApJ*, **794**, 89
- Koch, A., Wilkinson, M. I., Kleyna, J. T., et al. 2009b, *ApJ*, **690**, 453
- Koposov, S., Belokurov, V., Evans, N. W., et al. 2008, *ApJ*, **686**, 279
- Koposov, S. E., Belokurov, V., & Torrealba, G. 2017, *MNRAS*, **470**, 2702
- Koposov, S. E., Belokurov, V., Torrealba, G., & Evans, N. W. 2015a, *ApJ*, **805**, 130
- Koposov, S. E., Casey, A. R., Belokurov, V., et al. 2015b, *ApJ*, **811**, 62
- Koposov, S. E., Gilmore, G., Walker, M. G., et al. 2011, *ApJ*, **736**, 146
- Kormendy, J. 1990, in *The Edwin Hubble Centennial Symp., The Evolution of the Universe of Galaxies*, ed. R. G. Kron (San Francisco, CA: ASP), 33
- Laevens, B. P. M., Martin, N. F., Bernard, E. J., et al. 2015a, *ApJ*, **813**, 44
- Laevens, B. P. M., Martin, N. F., Ibata, R. A., et al. 2015b, *ApJ*, **802**, L18
- Laevens, B. P. M., Martin, N. F., Sesar, B., et al. 2014, *ApJ*, **786**, L3
- Lai, D. K., Lee, Y. S., Bolte, M., et al. 2011, *ApJ*, **738**, 51
- Lake, G. 1990, *MNRAS*, **244**, 701
- Lampland, C. O., & Tombaugh, C. W. 1976, *AN*, **246**, 171
- Lauberts, A. 1976, *A&A*, **52**, 309
- Law, D. R., & Majewski, S. R. 2010, *ApJ*, **718**, 1128
- Lee, K. H., Lee, H. M., Fahlman, G. G., & Sung, H. 2004, *AJ*, **128**, 2838
- Lee, M. G., Freedman, W., Mateo, M., & Thompson, I. 1993, *AJ*, **106**, 1420
- Lee, M. G., Park, H. S., Park, J., et al. 2003, *AJ*, **126**, 2840
- Li, T. S., Simon, J. D., Drlica-Wagner, A., et al. 2017, *ApJ*, **838**, 8
- Luque, E., Pieres, A., Santiago, B., et al. 2017, *MNRAS*, **468**, 97
- Luque, E., Queiroz, A., Santiago, B., et al. 2016, *MNRAS*, **458**, 603
- Madore, B. F., & Arp, H. C. 1982, *PASP*, **94**, 40
- Majewski, S. R., Frinchaboy, P. M., Kunkel, W. E., et al. 2005, *AJ*, **130**, 2677
- Majewski, S. R., Ostheimer, J. C., Patterson, R. J., et al. 2000, *AJ*, **119**, 760
- Martin, N. F., Coleman, M. G., De Jong, J. T. A., et al. 2008a, *ApJL*, **672**, L13
- Martin, N. F., de Jong, J. T. A., & Rix, H.-W. 2008b, *ApJ*, **684**, 1075
- Martin, N. F., Geha, M., Ibata, R. A., et al. 2016, *MNRAS*, **458**, L59
- Martin, N. F., & Jin, S. 2010, *ApJ*, **721**, 1333
- Martin, N. F., Nidever, D. L., Besla, G., et al. 2015, *ApJL*, **804**, L5
- Martínez-Delgado, D., Alonso-García, J., Aparicio, A., & Gómez-Flechoso, M. A. 2001, *ApJ*, **549**, L63
- Mateo, M. L. 1998, *ARA&A*, **36**, 435
- McConnachie, A. W. 2012, *AJ*, **144**, 4
- McLaughlin, D. E., & van der Marel, R. P. 2005, *ApJS*, **161**, 304
- McLeod, B., Geary, J., Conroy, M., et al. 2015, *PASP*, **127**, 366
- Mighell, K. J. 1997, *AJ*, **114**, 1458
- Mighell, K. J., & Rich, M. 1996, *AJ*, **111**, 777
- Misgeld, I., & Hilker, M. 2011, *MNRAS*, **414**, 3699
- Mucciarelli, A., Monaco, L., Bonifacio, P., et al. 2017, *A&A*, **603**, L7
- Muñoz, R. R., Carlin, J. L., Frinchaboy, P. M., et al. 2006a, *ApJL*, **650**, L51
- Muñoz, R. R., Côté, P., Santana, F. A., et al. 2018, *ApJ*, **860**, 65 (Paper I)
- Muñoz, R. R., Frinchaboy, P. M., Majewski, S. R., et al. 2005, *ApJL*, **631**, L137
- Muñoz, R. R., Geha, M., Côté, P., et al. 2012a, *ApJL*, **753**, L15
- Muñoz, R. R., Geha, M., & Willman, B. 2010, *AJ*, **140**, 138
- Muñoz, R. R., Majewski, S. R., Zaggia, S., et al. 2006b, *ApJ*, **649**, 201
- Muñoz, R. R., Padmanabhan, N., & Geha, M. 2012b, *ApJ*, **745**, 127
- Myeong, G. C., Jerjen, H., Mackey, D., et al. 2017, *ApJL*, **840**, L25
- Norris, M. A., Kannappan, S. J., Forbes, D. A., et al. 2014, *MNRAS*, **443**, 1151
- Odenkirchen, M., Grebel, E. K., Harbeck, D., et al. 2001, *AJ*, **122**, 2538
- Okamoto, S., Arimoto, N., Yamada, Y., et al. 2008a, in *Astronomical Society of the Pacific Conference Series, Vol. 399, Panoramic Views of Galaxy Formation and Evolution*, ed. T. Kodama, T. Yamada, & K. Aoki (San Francisco, CA: ASP), 469
- Okamoto, S., Arimoto, N., Yamada, Y., & Onodera, M. 2008b, *A&A*, **487**, 103
- Okamoto, S., Arimoto, N., Yamada, Y., & Onodera, M. 2012, *ApJ*, **744**, 96
- Olszewski, E. W., Aaronson, M., & Hill, J. M. 1995, *AJ*, **110**, 2120
- Olszewski, E. W., Pryor, C., & Armandroff, T. E. 1996, *AJ*, **111**, 750
- Ortolani, S., Bica, E., & Barbuy, B. 2013, *MNRAS*, **433**, 1966
- Pace, A. B., Martínez, G. D., Kaplinghat, M., & Muñoz, R. R. 2014, *MNRAS*, **442**, 1718
- Palma, C., Kunkel, W. E., & Majewski, S. R. 2000, *PASP*, **112**, 1305
- Palma, C., Majewski, S. R., Siegel, M. H., et al. 2003, *AJ*, **125**, 1352
- Paust, N., Wilson, D., & van Belle, G. 2014, *AJ*, **148**, 19
- Peterson, C. J. 1976, *AJ*, **81**, 617
- Plummer, H. C. 1911, *MNRAS*, **71**, 460
- Press, W. H., Flannery, B. P., Teukolsky, S. A., & Vetterling, W. T. 1988, *Numerical Recipes in C: The Art of Scientific Computing* (New York: Cambridge Univ. Press)
- Pryor, C., & Kormendy, J. 1990, *AJ*, **100**, 127
- Pryor, C., & Meylan, G. 1993, in ASP Conf. Ser. 50, *Structure and Dynamics of Globular Clusters*, ed. S. G. Djorgovski & G. Meylan (San Francisco, CA: ASP), 357
- Racine, R., & Harris, W. E. 1975, *ApJ*, **196**, 413
- Roderick, T. A., Mackey, A. D., Jerjen, H., & Da Costa, G. S. 2016, *MNRAS*, **461**, 3702
- Salpeter, E. E. 1955, *ApJ*, **121**, 161
- Sand, D. J., Olszewski, E. W., Willman, B., et al. 2009, *ApJ*, **704**, 898
- Sand, D. J., Seth, A., Olszewski, E. W., et al. 2010, *ApJ*, **718**, 530
- Sand, D. J., Strader, J., Willman, B., et al. 2012, *ApJ*, **756**, 79
- Sanna, N., Dalessandro, E., Ferraro, F. R., et al. 2014, *ApJ*, **780**, 90
- Santana, F. A., Muñoz, R. R., de Boer, T. J. L., et al. 2016, *ApJ*, **829**, 86, (Paper VI)
- Santana, F. A., Muñoz, R. R., Geha, M., et al. 2013, *ApJ*, **774**, 106, (Paper II)
- Sarajedini, A. 1997, *AJ*, **113**, 682
- Searle, L., & Zinn, R. 1978, *ApJ*, **225**, 357
- Ségall, M., Ibata, R. A., Irwin, M. J., Martin, N. F., & Chapman, S. 2007, *MNRAS*, **375**, 831
- Sérsic, J. L. 1968, *Atlas de Galaxias Australes* (Cordoba: Observatorio Astronomico)
- Shapley, H. 1920, *ApJ*, **52**, 73
- Shapley, H. 1930, *Star Clusters* (New York: McGraw-Hill)
- Shapley, H. 1938a, *BHarO*, **908**, 1
- Shapley, H. 1938b, *Natur*, **142**, 715
- Shapley, H., & Mayberry, B. W. 1921, *PNAS*, **7**, 152
- Siegel, M. H., Majewski, S. R., Cudworth, K. M., & Takamiya, M. 2001, *AJ*, **121**, 935
- Simon, J. D., & Geha, M. 2007, *ApJ*, **670**, 313
- Simon, J. D., Geha, M., Minor, Q. E., et al. 2011, *ApJ*, **733**, 46
- Simon, J. D., Li, T. S., Drlica-Wagner, A., et al. 2017, *ApJ*, **838**, 11

- Smecker-Hane, T. A., Stetson, P. B., Hesser, J. E., & Lehnert, M. 1994, *AJ*, 108, 507
- Sohn, Y.-J., Park, J.-H., Rey, S.-C., et al. 2003, *AJ*, 126, 803
- Sollima, A., Martínez-Delgado, D., Valls-Gabaud, D., & Peñarrubia, J. 2011, *ApJ*, 726, 47
- Stetson, P. B. 1994, *PASP*, 106, 250
- Stetson, P. B., Bolte, M., Harris, W. E., et al. 1999, *AJ*, 117, 247
- The DES Collaboration, Bechtol, K., Drlica-Wagner, A., et al. 2015, *ApJ*, 807, 50
- Tollerud, E. J., Bullock, J. S., Graves, G. J., & Wolf, J. 2011, *ApJ*, 726, 108
- Tollerud, E. J., Bullock, J. S., Strigari, L. E., & Willman, B. 2008, *ApJ*, 688, 277
- Torrealba, G., Belokurov, V., Kuposov, S. E., et al. 2018, *MNRAS*, 475, 5085
- Torrealba, G., Kuposov, S. E., Belokurov, V., & Irwin, M. 2016a, *MNRAS*, 459, 2370
- Torrealba, G., Kuposov, S. E., Belokurov, V., et al. 2016b, *MNRAS*, 463, 712
- Trager, S. C., King, I. R., & Djorgovski, S. 1995, *AJ*, 109, 218
- Valcheva, A. T., Ovcharov, E. P., Lalova, A. D., et al. 2015, *MNRAS*, 446, 730
- Walker, M. G., Belokurov, V., Evans, N. W., et al. 2009a, *ApJL*, 694, L144
- Walker, M. G., Mateo, M., Olszewski, E. W., et al. 2007, *ApJL*, 667, L53
- Walker, M. G., Mateo, M., Olszewski, E. W., et al. 2009b, *AJ*, 137, 3109
- Walker, M. G., Mateo, M., Olszewski, E. W., et al. 2016, *ApJ*, 819, 53
- Walsh, S. M., Jergen, H., & Willman, B. 2007, *ApJ*, 662, L83
- Walsh, S. M., Willman, B., Sand, D., et al. 2008, *ApJ*, 688, 245
- Webbink, R. F. 1985, in IAU Symp. 113, Dynamics of Stars Clusters, ed. J. Goodman & P. Hut (Dordrecht: Reidel), 541
- Weinberger, R. 1995, *PASP*, 107, 58
- Westfall, K. B., Majewski, S. R., Ostheimer, J. C., et al. 2006, *AJ*, 131, 375
- Whiting, A. B., Hau, G. K. T., & Irwin, M. 2002, *ApJS*, 141, 123
- Wilkinson, M. I., Kleyna, J. T., Evans, N. W., et al. 2004, *ApJL*, 611, L21
- Willman, B., Blanton, M. R., West, A. A., et al. 2005a, *AJ*, 129, 2692
- Willman, B., Dalcanton, J. J., Martínez-Delgado, D., et al. 2005b, *ApJL*, 626, L85
- Willman, B., Geha, M., Strader, J., et al. 2011, *AJ*, 142, 128
- Willman, B., Masjedi, M., Hogg, D. W., et al. 2006, arXiv:astro-ph/0603486
- Willman, B., & Strader, J. . 2012, *AJ*, 144, 76
- Wilson, A. G. 1955, *PASP*, 67, 27
- York, D. G., Adelman, J., Anderson, J. E., Jr., et al. 2000, *AJ*, 120, 1579
- Zinn, R. 1980a, *ApJ*, 241, 602
- Zinn, R. 1980b, *ApJS*, 42, 19
- Zucker, D. B., Belokurov, V., Evans, N. W., et al. 2006a, *ApJL*, 643, L103
- Zucker, D. B., Belokurov, V., Evans, N. W., et al. 2006b, *ApJL*, 650, L41
- Zwicky, F. 1959, Carnegie Inst. Washington Yearbook, 58, 60